FZD-483

Experiments on two-phase flow in a vertical tube with a moveable obstacle

H.-M. Prasser, M. Beyer, H. Carl, S. Al Issa,
P. Schütz, H. Pietruske

September 2007

Wissenschaftlich-Technische Berichte
FZD-483 2007 · ISSN 1437-322X

WISSENSCHAFTLICH-TECHNISCHE BERICHTE

Forschungszentrum
Dresden Rossendorf

Wissenschaftlich-Technische Berichte
FZD-483
September 2007

H.-M. Prasser, M. Beyer, H. Carl, S. Al Issa,
P. Schütz, H. Pietruske

Experiments on two-phase flow in a vertical tube with a moveable obstacle

Technical Report

Forschungszentrum
Dresden Rossendorf

Technischer Fachbericht

Experimente zur Zweiphasenströmung in einem vertikalen Rohr mit verschiebbarem Hindernis

Technical Report

Experiments on two-phase flow in a vertical tube with a moveable obstacle

Reaktorsicherheitsforschung-Vorhaben-Nr./ Reactor Safety Research-project No.: 150 1265

Vorhabenstitel: **Aufbau und Durchführung von Experimenten an der Mehrzweck-Thermohydraulikversuchsanlage TOPFLOW für generische Untersuchungen von Zweiphasenströmungen und die Weiterentwicklung und Validierung von CFD-Codes.**

Project Title: **Construction and execution of experiments at the multi-purpose thermal hydraulic test facility TOPFLOW for generic investigations of two-phase flows and the development and validation of CFD codes.**

Autoren / Author(s): **H.-M. Prasser, M. Beyer, H. Carl, S. Al Issa, P. Schütz, H. Pietruske**

Dienststelle der Autoren / Performing Organisation: **Forschungszentrum Dresden-Rossendorf e.V. Institut für Sicherheitsforschung**

Berichtsdatum / Publication Date: **September 2007**

Berichts-Nr. / Report-No.: **FZD-483**

Das diesem Bericht zugrunde liegende Vorhaben wurde mit Mitteln des Bundesministeriums für Wirtschaft und Technologie unter dem Förderkennzeichen 150 1265 gefördert. Die Verantwortung für den Inhalt dieser Veröffentlichung liegt bei den Autoren.

Berichtsblatt

1. ISBN oder ISSN	2. Berichtsart Technischer Fachbericht
3a. Titel des Berichts Experimente zur Zweiphasenströmung in einem vertikalen Rohr mit verschiebbarem Hindernis	
3b. Titel der Publikation	
4a. Autoren des Berichts (Name, Vorname(n)) H.-M. Prasser, M. Beyer, H. Carl, S. Al Issa, P. Schütz, H. Pietruske	5. Abschlussdatum des Vorhabens 30.09.2006
	6. Veröffentlichungsdatum September 2007
4b. Autoren der Publikation (Name, Vorname(n))	7. Form der Publikation Broschüre
8. Durchführende Institution(en) (Name, Adresse) Forschungszentrum Dresden-Rossendorf e.V. Institut für Sicherheitsforschung Postfach 510119 01314 Dresden	9. Ber.Nr. Durchführende Institution
	10. Förderkennzeichen *) 150 1265
	11a. Seitenzahl Bericht 104
	11b. Seitenzahl Publikation
13. Fördernde Institution (Name, Adresse) Bundesministeriums für Wirtschaft und Technologie (BMWi) 11019 Berlin	12. Literaturangaben 32
	14. Tabellen 2
	15. Abbildungen 88
16. Zusätzliche Angaben	
17. Vorgelegt bei (Titel, Ort, Datum)	

18. Kurzreferat

Der vorliegende Bericht beschreibt eine neue Methode zur Untersuchung von Zweiphasen-Strömungsfeldern in der Umgebung eines asymmetrischen Hindernisses innerhalb eines vertikalen Rohres, die Daten zur Validierung von CFD Codes für komplexe Geometrien liefert. Hauptmerkmal dieser Versuchsanordnung ist die Möglichkeit, das Hindernis gegenüber dem stationären Gittersensor zu verschieben und somit dreidimensionale Gasgehaltsfelder zu erfassen. Neben der Messung von zeitgemittelten Gasgehaltsverteilungen wird eine neue Methode zur Datenauswertung vorgestellt, die mittels Gittersensordaten Geschwindigkeitsprofile der flüssigen Phase abschätzt. Die Strömung im Umfeld eines Hindernisses mit der vorliegenden Geometrie hat viele topologische Ähnlichkeiten mit komplexen Strömungen in Rohrbögen, T-Stücken, Ventilen und Sicherheitsventilen sowie anderen in Kraftwerksanlagen verwendeten Komponenten. Gekrümmte und gegenüber dem Gravitationsvektor signifikant geneigte Stromlinien, Strömungsseparation an scharfen Kanten und Rezirkulationsgebiete im Nachlauf des Hindernisses sind Phänomene, die mittels dieser Versuchsanordnung analysiert werden können. Um die Qualität von CFD Codes einschließlich der implementierten Mehrphasen- und Turbulenzmodelle einschätzen zu können, wurden mit ANSYS CFX 10.0 Vorausrechnungen durchgeführt. Ein Vergleich zwischen den Rechenergebnissen und den experimentellen Daten zeigt eine gute Übereinstimmung bei allen signifikanten qualitativen Details sowohl für die Gasgehalts- als auch die Geschwindigkeitsverteilungen der flüssigen Phase. Weiterhin enthält der Bericht eine Methode zur Abschätzung der lateralen Komponenten für Blasengeschwindigkeiten in Form einer kurzen theoretischen Beschreibung und Visualisierungsbeispielen. Die Bilder zeigen die Strömungsablenkung im Umfeld des Hindernisses mittels Vektoren, die die Durchschnittsgeschwindigkeiten aller Blasen an den jeweiligen Kreuzungspunkten während der Durchdringung der Messebene des Sensors repräsentieren. Eine detaillierte Unsicherheitsanalyse zur Geschwindigkeitsabschätzung schließt den vorliegenden Bericht ab. Sie beinhaltet Informationen über den Vergleich mit der Kreuzkorrelation, einer zweiten Methode zur Ermittlung von Gasgeschwindigkeitsprofilen. Zusätzlich gibt dieses Kapitel einen Überblick über den Einfluss von Beschleunigungs- und Verzögerungseffekten auf die Geschwindigkeitsberechnungen.

19. Schlagwörter Zweiphasenströmung, Gasblasen, Gasgehaltsverteilungen, Geschwindigkeitsfelder	
20. Verlag	21. Preis

Document Control Sheet

1. ISBN or ISSN	2. Type of Report Technical Report
3a. Report Title Experiments on two-phase flow in a vertical tube with a moveable obstacle	
3b. Title of Publication	
4a. Author(s) of the Report (Family Name, First Name(s)) H.-M. Prasser, M. Beyer, H. Carl, S. Al Issa, P. Schütz, H. Pietruske	5. End of Project 30.09.2006
	6. Publication Date September 2007
4b. Author(s) of the Publication (Family Name, First Name(s))	7. Form of Publication Booklet
8. Performing Organisation(s) (Name, Address) Forschungszentrum Dresden-Rossendorf e.V. Institut für Sicherheitsforschung Postfach 510119 01314 Dresden	9. Originator's Report No.
	10. Reference No.*) 150 1265
	11a. No. of Pages Report 104
	11b. No. of Pages Publication
13. Sponsoring Agency (Name, Address) Bundesministeriums für Wirtschaft und Technologie (BMWi) 11019 Berlin	12. No. of References 32
	14. No. of Tables 2
	15. No. of Figures 88
16. Supplementary Notes	
17. Presented at (Title, Place, Date)	

18. Abstract

A novel technique to study the two-phase flow field around an asymmetric diaphragm in a vertical pipe is presented, that enables producing data for CFD code validation in complex geometries. Main feature is a translocation of the diaphragm to scan the 3D void field with a stationary wire-mesh sensor. Besides the measurement of time-averaged void fraction fields, a novel data evaluation method was developed to extract estimated liquid velocity profiles from the wire-mesh sensor data. The flow around an obstacle of the chosen geometry has many topological similarities with complex flow situations in bends, T-junctions, valves, safety valves and other components of power plant equipment and flow phenomena like curved stream lines, which form significant angles with the gravity vector, flow separation at sharp edges and recirculation zones in their wake are present. In order to assess the quality of the CFD code and their underlying multiphase flow and turbulence models pre-test calculations by ANSYS CFX 10.0 were carried out. A comparison between the calculation results and the experimental data shows a good agreement in term of all significant qualitative details of the void fraction and liquid velocity distributions. Furthermore, the report contains a method to assess the lateral components of bubble velocities in the form of a basic theoretical description and visualisation examples. The plots show the deviation of the flow around the obstacle in term of vectors represented the average velocities of the instantaneous cross-sections of all bubbles in the time interval when they pass the measuring plane. A detailed uncertainty analyse of the velocity assessments concludes the presented report. It includes remarks about the comparison with a second method for calculating bubble velocity profiles – the cross-correlation. In addition, this chapter gives an overview about the influence of acceleration and deceleration effects on the velocity estimation.

19. Keywords
Two-Phase Flow, Gas bubbles, Gas volume fraction distribution, velocity fields

20. Publisher	21. Price

This report is part of a series, which comprise following reports:

- Construction and execution of experiments at the multi-purpose thermal hydraulic test facility TOPFLOW for generic investigations of two-phase flows and the development and validation of CFD codes (Final project report), FZD-481,
- Experiments on upwards gas-liquid flow in vertical pipes, FZD-482,
- Experiments on two-phase flow in a vertical tube with a moveable obstacle, FZD-483,
- Experimental investigation of stratified air/water flows in a horizontal channel, FZD-484,
- Experimental investigation and CFD simulation of slug flow in horizontal channels, FZD-485,
- CFD models for polydispersed bubbly flows, FZD-486,
- Turbulent Dispersion of Bubbles in Poly-dispersed Gas-Liquid Flows in a Vertical Pipe, FZD-487,
- Validation of the Multiple Velocity Multiple Size Group (CFX10.0 N x M MUSIG) Model for Poly-dispersed Multiphase Flows, FZD-487.

All these reports are published as reports of the Forschungszentrum Dresden-Rossendorf.

Dieser Bericht ist Teil einer Serie, die folgende Einzelberichte umfasst:

- Aufbau und Durchführung von Experimenten an der Mehrzweck-Thermohydraulikversuchsanlage TOPFLOW für generische Untersuchungen von Zweiphasenströmungen und die Weiterentwicklung und Validierung von CFD-Codes (Abschlussbericht), FZD-480,
- Experimente zu aufwärtsgerichteten Gas-Flüssig Strömungen in vertikalen Rohren, FZD-482,
- Experimente zur Zweiphasenströmung in einem vertikalen Rohr mit verschiebbarem Hindernis, FZD-483,
- Experimentelle Untersuchung von geschichteten Luft/Wasser Strömungen in einem horizontalen Kanal, FZD-484,
- Experimentelle Untersuchung und CFD-Simulation von Schwallströmung in horizontalen Kanälen, FZD-485,
- CFD Modelle für polydisperse Blasenströmungen, FZD-486,
- Turbulente Blasendispersion in einer polydispersen Rohrströmung, FZD-487,
- Validierung des N x M MUSIG Modells für polydisperse Mehrphasen-strömungen, FZD-487.

Alle Berichte sind als Berichte des Forschungszentrums Dresden-Rossendorf veröffentlicht.

Contents

1. Introduction

In the frame of the TOPFLOW project, vertical pipe flow is experimentally studied in order to develop and validate models for bubble forces as well as for bubble coalescence and fragmentation in a gas-liquid two-phase flow. The advantage of the TOPFLOW facility (Beyer et al., 2004) consists in the combination of:

1. large scale test sections with
2. a wide operational parameter range in terms of both the superficial velocities and the system pressure and
3. a dedicated high-resolution instrumentation, namely the wire-mesh sensors.

In the last years, a large number of experiments in straight vertical pipes (Prasser et al., 2004a; Prasser, 2004b; Prasser et al., 2005a; Prasser et al., 2005b) were performed for the development of closure relations describing the forces acting on bubbles as well as a multi-bubble size model for the code ANSYS CFX 10.0. In the current experiments, the large test section with a nominal diameter of DN200 was used to study the flow field around an asymmetric obstacle. This is an interesting test case for CFD code validation, since the obstacle creates a pronounced three-dimensional two-phase flow field. Curved stream lines, which form significant angles with the gravity vector, a recirculation zone in the wake and a flow separation at the edge of an obstacle are common in industrial components and installations.

Runs were performed with an air-water flow at ambient conditions as well as with a steam-water mixture at a saturation pressure of 6.5 MPa. The measurements were carried out in the vertical test section of TOPFLOW using a DN200 wire-mesh sensor. The wire-mesh sensors are available for ambient conditions as well as for saturated conditions at a pressure up to 7 MPa and supply detailed data on the instantaneous flow structure with a high resolution in space and time. In particular, this allows to visualise the structure of the gas liquid interface.

2. Literature review

Single and two-phase flows of three-dimensional nature were subject of numerous studies found in literature. Most of them dealt with flows around obstacles or, respectively, through a sudden expansion or constrictions in general. Similar flow fields are found in many engineering applications, like nuclear reactors, chemical reactors and power plants in general. A prominent example is the steam-water flow in safety valves described by Nishimura et al. (2000) and Boccardi et al. (2004). One of the general characteristic of these flows is the formation of vortexes and recirculation zones downstream of the obstacle. The majority of the works aims at the prediction of the flow field and its main features like length, reattachment point, void fraction and velocity field distributions on basis of different modelling approaches. Experiments are carried out in order to validate the proposed models. Concerning the choice of the fluid, single-phase liquid flow experiments are presented by Anagnostopoulos et al. (2004) and Sotiriadis et al. (2005), gas-liquid two-phase studies are found in Rinne et al. (1996), Nishimura et al. (2000), Morel et al. (2004), Boccardi et al. (2004), Kondo et al. (2002, 2004, 2005) and Ahmed et al. (2005), a pure gas wind channel experiment is given in Ota et al. (2001) and particulate liquid-solid flows are subject of Founti et al. (2001). Some papers deal with practical problems, like the determination of the capacity of safety valves (Nishimura et al., 2000 and Boccardi et

al., 2004) and wear in particle laden oil flows (Founti et al., 2001). Details of the flow field downstream the geometry change are obtained by LDA (Founti et al., 1998; Sotiriadis et al., 2005) and PIV (Anagnostopoulos et al., 2004) or, alternatively, by hot-film and hot wire anemometers (Founti et al., 2001, Morel et al., 2004 and Ahmed et al., 2005). The gas fraction and the structure of the two-phase flow are measured by local probes (Kondo et al., 2002 and Morel et al., 2004) and high-speed camera observation by Rinne et al. (1996), Kondo et al. (2002) and Ahmed et al. (2005). In all cases, except the wind channel (Ota et al., 2001), the flow domain has a characteristic scale of 25 - 100 mm. There are no experiments published dealing with high resolution measurements of the flow field in gas-liquid two-phase flows at higher pressures and temperatures. It is a unique feature of TOPFLOW to combine a comparatively large scale with the ability to perform experiments with steam-water mixture at up-to 7 MPa.

From the shape of the cross-section change, a stepwise expansion dominates, because the recirculation areas forming downstream present a challenge to the modelling. In one case, a movable piston was applied to create a periodically changing cross-section obstruction. The idea of the movable obstacle in our tests is different from this methodology, since here the change of the position of the diaphragm is used to vary the distance between obstacle and sensor in order to obtain 3D parameter fields, and not the degree of obstruction.

Concerning modelling and simulation, different mathematical approaches were used for the numerical simulation, like own implementations of the SIMPLE algorithm in Anagnostopoulos et al. (2004), Eulerian particle tracing (Founti et al., 1998, 2001 and Kondo et al., 2002, 2004, 2005) including collision modelling (Founti et al., 1998), two-fluid models (Morel et al., 2004), Large eddy Simulation, commercial CFD codes like CFX (Prasser et al., 2004c) and NEPTUNE by Morel et al. (2004). 3D modelling of two-phase flows showed the importance of the correct reflection of the forces acting on bubbles according to their diameter. The need to represent measured data in 3D appeared in most cases. Sometimes symmetry properties, like radial symmetry, were used to concentrate on radial profiles. With our own experiments we faced the challenge to create a complex three-dimensional flow field and to characterise it by a 2D measuring sensor, which was indirectly traversed along the flow direction by moving the obstacle.

Particular results concerning the behaviour of the flow field downstream of an expansion are worth mentioning: In a horizontal flow and a liquid-particle flow it was found that a second recirculation may happen far from the sudden expansion (Founti et al., 2001 and Anagnostopoulos et al., 2004), the reattachment point was dependent on particle loading (Founti et al., 1998). A similarity to the influence of the void fraction in our case can be expected. The reattachment distance also was related to the obstacle dimensions (Ota et al., 2001 and Sotiriadis et al., 2005). The movement and behaviour of bubbles incorporated many phenomena. The bubbles were deformed and broken by a strong liquid shear field. Also they were not driven to the wall after the expansion as an expected effect of the shear layer, which is a result of the change of the sign of the lift force coefficient (Kondo et al., 2005). Bubble entrainment into recirculation zones was dependent on the Stokes number (Founti et al., 1998), sometimes they were trapped in the recirculation zone (Founti et al., 2001), but they were escaping in case of the occurrence of a large vortex and large fluxes (Kondo et al., 2005). If the flow contains slugs, those are broken up on their way through the expansion. This changes the flow pattern from slug to bubbly flow

(Kondo et al., 2005 and Ahmed et al., 2005). This phenomenon becomes dominating at large superficial velocities (Kondo et al., 2002). The effect of the bubble diameters on the interfacial area forces was demonstrated by Morel et al. (2004) and Kondo et al. (2004). The motion of small bubbles at high superficial liquid velocities needs further investigation (Kondo et al., 2005). An increase in the liquid velocity, turbulence and drift velocities were marked in Ahmed et al. (2005), the deformation of the flow is conserved up-to large distances from the cross-section change and was still found even far from the reattachment point (Ota et al., 2001, Kondo et al., 2002 and Ahmed et al., 2005). This implies that the ordinary flow regime map, which was elaborated to characterise the two-phase flow in a straight channel, may be inapplicable to complex 3D two-phase flow, and some modification should be considered in Kondo et al. (2002). The intensity of reverse and lateral flows was marked in Ota et al. (2001).

3. Test facility

The described experiments were performed at the Two Phase FLOW Test Facility (TOPFLOW) located at the Institute of Safety Research of Forschungszentrum Dresden-Rossendorf e.V. A general scheme of the TOPFLOW facility is given in Fig. 3.1.

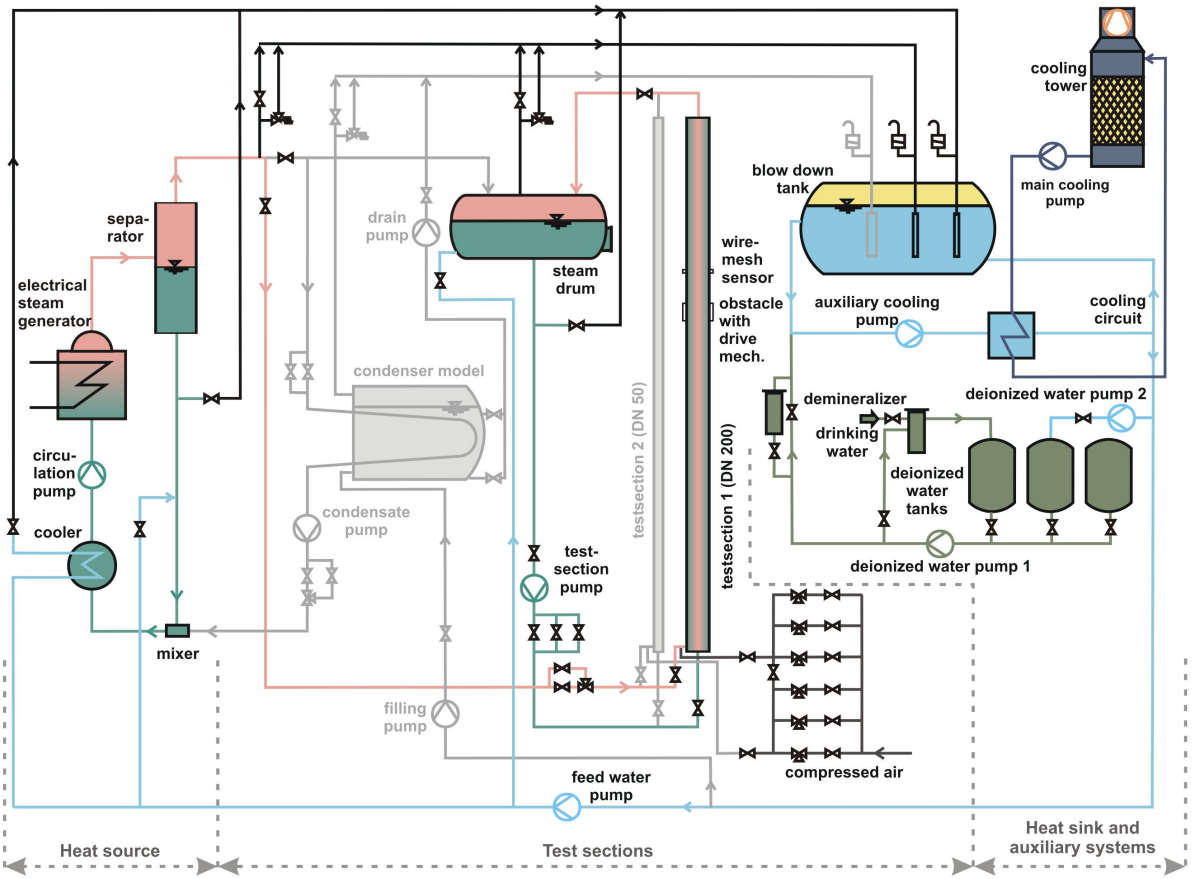

Fig. 3.1 General scheme of the thermal-hydraulic test facility TOPFLOW

An electrical steam generator with a power of 4 MW representing the heat source of the facility and a heat sink consisting of a blow-down tank to quench the exhaust steam, a cooling circuit and a dry cooling tower system are two main infrastructural components of TOPFLOW. Between these to ends, the flow passes through various

test rigs, which makes up a multi-purpose test facility. The steam is generated in 24 directly electrically heated stainless steel pipes, supplied from a power transformer. The heater circuit can be operated up to a pressure of 7 MPa and generate about 1,5 kg/s saturated steam at this pressure. The main experimental test rigs are:

- Two vertical test sections DN50 and DN200, both 9 m tall, for basic two-phase flow studies. The corresponding maximums of the L/D-ratios are 45 for DN200 and 180 for DN50.
- The passive heat removal system, which can be used to study the behaviour of passive safety systems for boiling water reactors (as emergency condenser). The test vessel has a volume of 18 m³, the tube bundle can transfer the full heater power.
- The pressure chamber (not represented in Fig. 3.1), which is used to accommodate test facilities for experiments at 5 MPa, but under pressure equilibrium. This allows performing hot pressurized experiments in light test facilities with thin or transparent parts for optical or infrared observation. The pressure tank has a volume of 40 m³.

The vertical test sections are equipped with a test section pump to generate the water flow up to 50 kg/s, with a steam supply system including mass flow meters and with a steam drum for the separation of the two-phase mixture at the outlet of the test sections. Big attention was paid to the accuracy of the steam and water mass flow measurements, which are performed by standard nozzle flow meters mounted in parallel and allow an accuracy of ±1 % over a mass flow range of 3 orders of magnitude.

Additionally to the high pressure steam operation, air-water flow experiments are possible. For this purpose, TOPFLOW is equipped with an air supply and metering station for up to 900 m³/h. Air is taken from the central pressurised air network of the research centre.

4. Geometrical boundary conditions

A three dimensional flow situation is obtained by disturbing vertical pipe flow with an obstacle. Because it is not possible to design a movable wire-mesh sensor, the other way around was applied: the sensor remains stationary and the obstacle - a half-moon diaphragm - is moved up and down in the DN200 test section (Fig. 4.1 and Fig. 4.2). This set-up will allow the measurement of the three-dimensional gas fraction field around the obstacle for air-water and steam-water experiments up to the maximum pressure of TOPFLOW. The field can be measured both upstream and downstream of the diaphragm, since the installation shown in Fig. 4.2 can either be flanged from below or from above after inverting it. Fig. 4.1 illustrates the assembling below the sensor that leads to a distance of 6170 mm between the injection device and the measuring plane of the sensor. If the obstacle is mounted above the sensor, this distance is 5110 mm. Unfortunately, the design of the test section does not allow equal distances. For this configuration the total height of the test section adds up to 9 m.

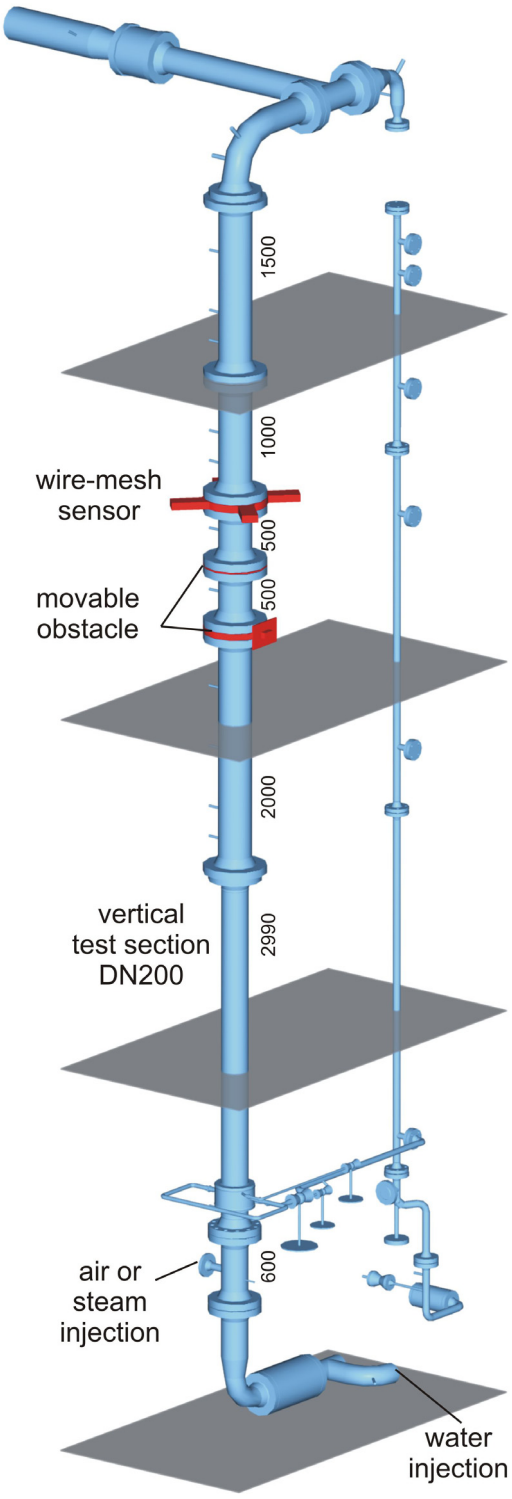

Fig. 4.1 Test section with obstacle and wire-mesh sensor

The diaphragm (Fig. 4.3) is a half-moon shaped disk. Its straight edge is arranged along the diameter of the pipe, while the circular edge is in a distance of 10 mm from the inner wall of the pipe (Fig. 4.4). It is made of a 4 mm thick sheet of stainless steel. The disk is mounted on top of a toothed rod, which is connected to a translation mechanism in order to change the axial position of the diaphragm. To maintain the obstacle in its position and to avoid oscillations, the toothed rod is handled by a guiding flange shown in the centre of Fig. 4.2. A pinion mounted to the shaft near the bottom flange is driving the toothed rod. This shaft establishes the force-fit connection to the worm gear transmission outside the tube.

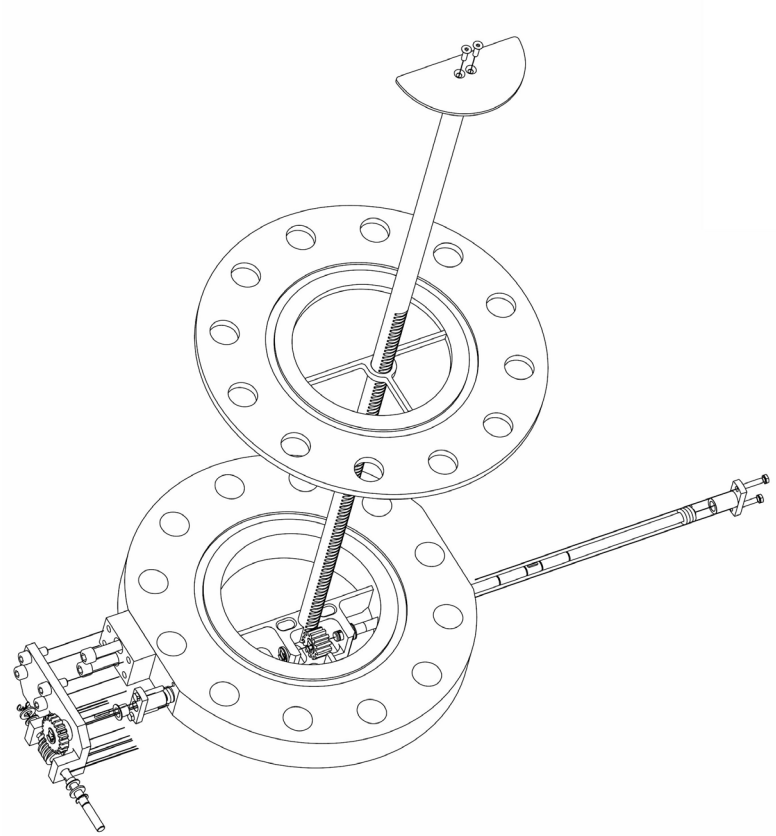

Fig. 4.2 Sketch of the movable obstacle with driving mechanism - a half-mood shaped horizontal plate mounted on top of a toothed rod

The obstacle is driven by a step motor, which is controlled by a personal computer. The positioning accuracy of the step motor is in a µm-range, so it does not take any effect on the positioning error of the obstacle. Basically, this error is caused by the manufacturing tolerance of the toothed rod mechanism and the worm gear transmission. During pre-tests it was estimated to ±1 mm.

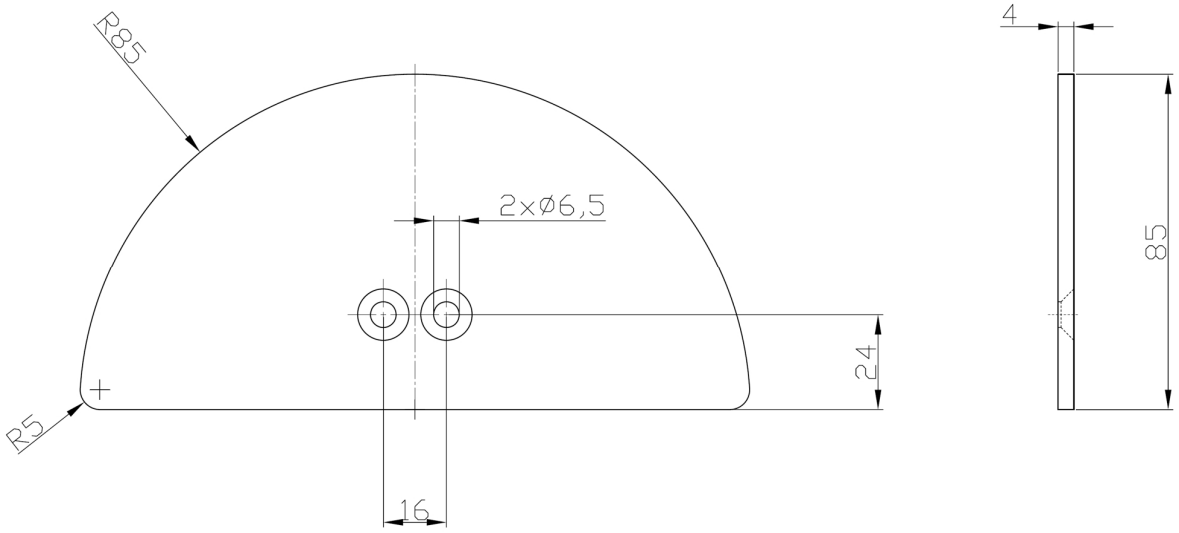

Fig. 4.3 Top and side view of the diaphragm

To compensate the thermal expansion of the toothed rod mechanism the experiments were executed at steady state thermal conditions. In this case we can

assume, that the toothed rod and the ambient segment of the test section expand evenly, because both are made of identical stainless steel.

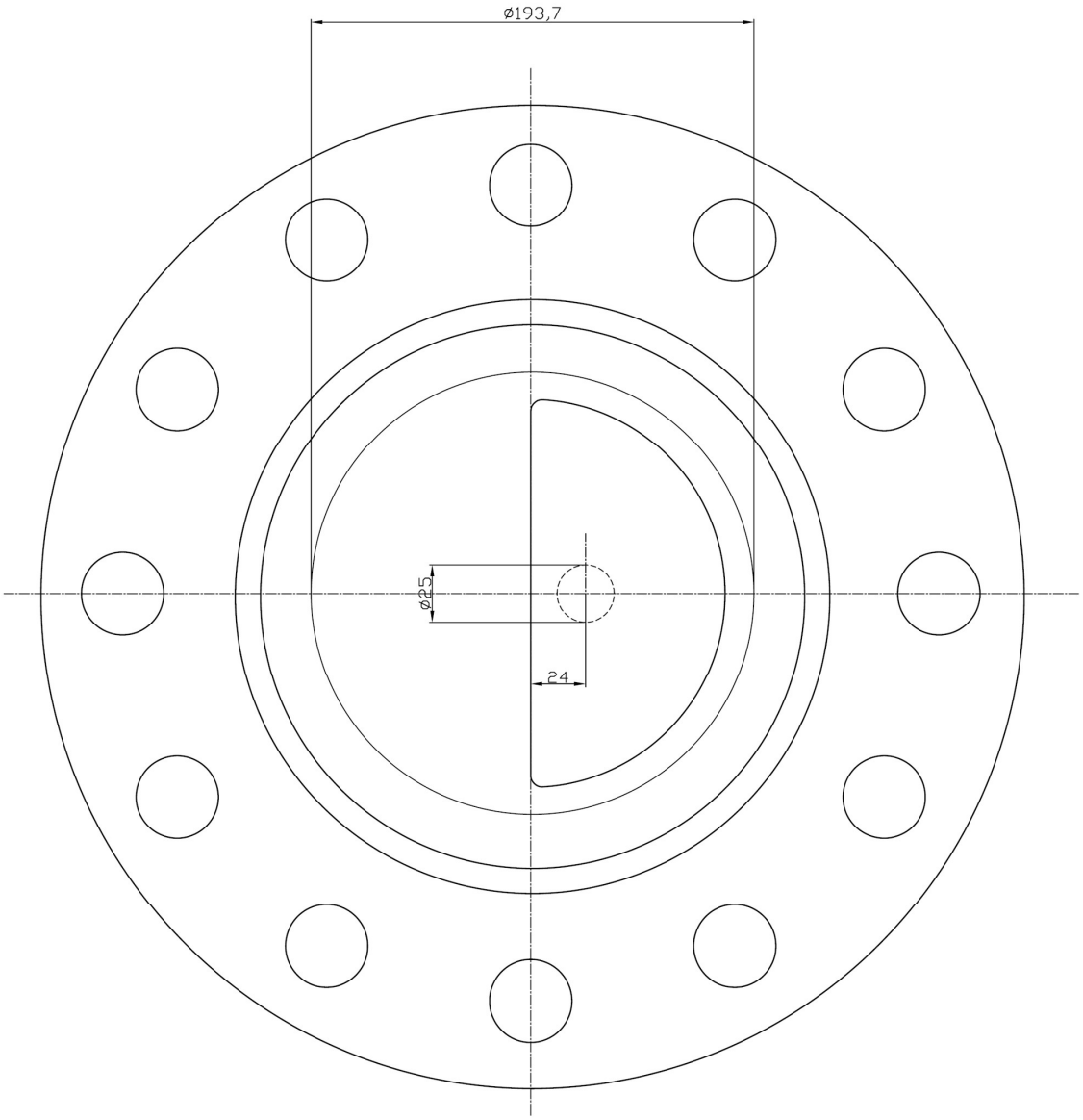

Fig. 4.4 Mounting position of the diaphragm inside the test section

The height position of the diaphragm is calculated using the value of the step motor, considering the transmission ratio of the driving mechanism. It was calibrated while toothed rod is slowly moving until a mechanical limitation which defines the maximum distance between the moving mechanism and the diaphragm. After this action, the height position is automatically set to 10 mm what corresponds to the minimum distance between the measuring plane of the wire-mesh sensor and the diaphragm. The maximum distance between these two planes is limited to 520 mm caused by the guiding flange (Fig. 4.2).

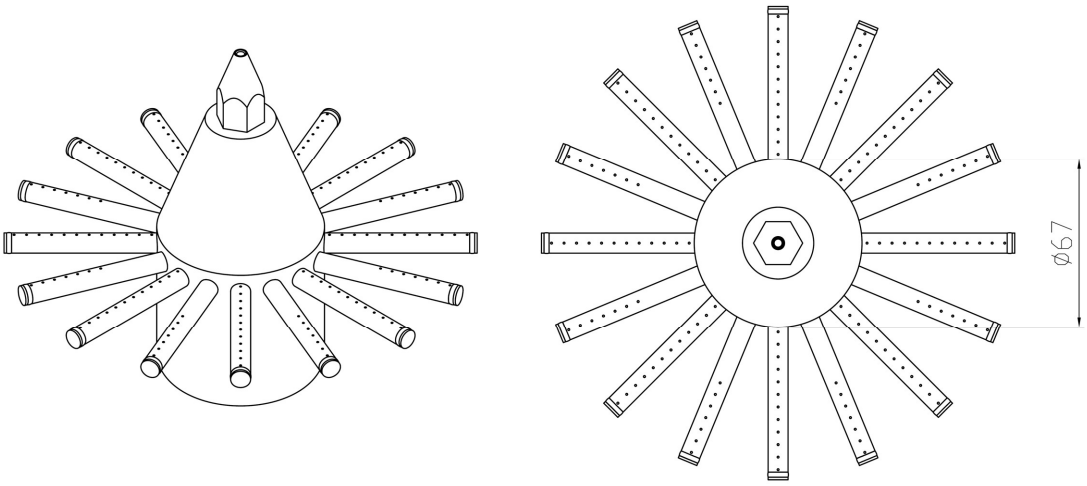

Fig. 4.5 Injector for the gaseous phase with 16 injection tubes and 152 orifices of 0.8 mm diameter

As aforementioned in chapter 3, the gaseous phase is fed on the bottom of the test section through a special injector shown in Fig. 4.5. This module consists of a central hollow cylinder with a conical head on which 16 thin radial tubes are welded. One half of these tubes has 7 drillings and the remaining – 12 orifices. This configuration aims to a uniform radial distribution of the gas. All orifices have a diameter of 0.8 mm and face downstream. To avoid a gas-leakage at the end of the tubes, they are plugged. The mounting position of the injector insight the mixing module of the test section is presented at Fig. 4.6.

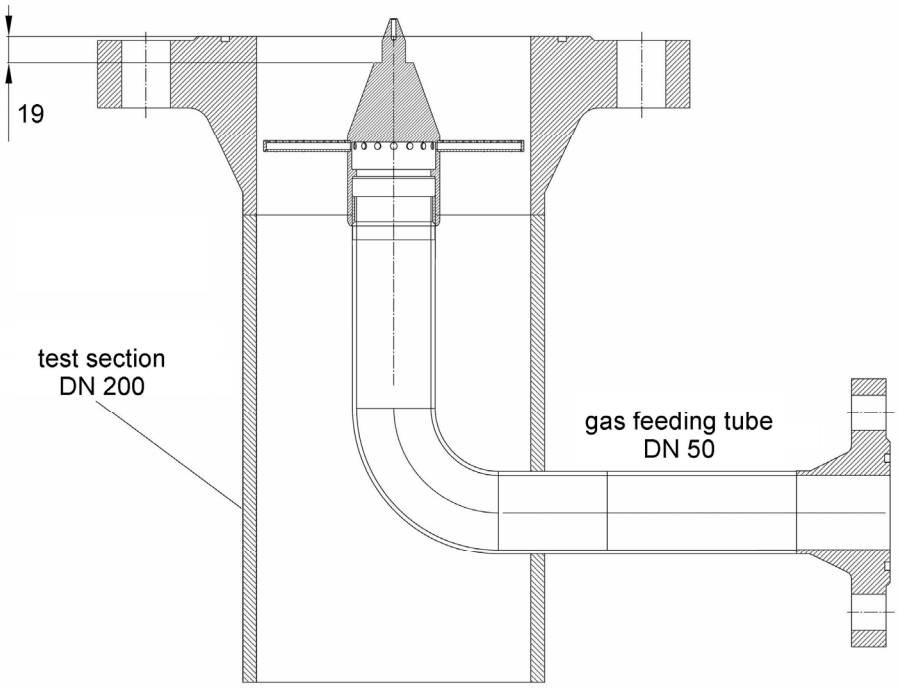

Fig. 4.6 Mixing module on bottom of the test section

5. Experiments and measuring technique

Measurements were carried out in an air-water flow at ambient pressure and a temperature about 30 °C as well as in a steam-water mixture under saturation conditions at 6.5 MPa and 281 °C. The high pressure allows reducing the volume condensation effects. Few experiments were also performed at 1, 2 and 4 MPa.

The test matrix given in Tab. 5.1 is a selection of combinations of superficial velocities for liquid and gas. This test matrix is a part of the common matrix used in the FZD for all experiments in the vertical test sections. Thereby it is possible to compare the results of the measurements with other runs without obstacle. The points measured with the obstacle are highlighted in Tab. 5.1. The tests at 1, 2 and 4 MPa were performed at J_L = 1.017 m/s and the following superficial steam velocities:

Tab. 5.1 Test matrix of the experiments with the movable obstacle, numbers: test run identifiers

water – superficial velocity	gas – superficial velocity							
m/s	0,0368	0,0574	0,0898	0,14	0,219	0,342	0,534	0,835
1,611	75	86	97	108	119	130	141	152
1,017	74	85	96	107	118	129	140	151
0,405	72	83	94	105	116	127	138	149
0,102	69	80	91	102	113	124	135	146

- p = 1 MPa J_G = 0.534 m/s (140),
- p = 2 MPa J_G = 0.219, 0.534 m/s (118, 140),
- p = 4 MPa J_G = 0.0898, 0.219, 0.534 m/s (096, 118, 140).

In order to study the two-phase flow around the obstacle the distance between diaphragm and mesh sensor was varied as follows: ± 520 mm, ± 250 mm, ± 160 mm, ± 80 mm, ± 40 mm, ± 20 mm, ± 15 mm, ± 10 mm. Experiment-related, negative positions mean that the sensor records the evolution of the flow downstream of the diaphragm and positive heights - upstream of it. This is also true for all measuring files, see attachment A. To be compatible with the numerical and theoretical descriptions in the other reports of the current project, this nomenclature was inverted, i.e. in the following sections of this report negative heights stand for flow pattern upstream and positive – downstream respectively.

It might be interesting to compare several runs. Therefore, the same sensor was used for air-water- as well as for steam-water tests with the obstacle. The high-temperature wire-mesh sensor employed (Fig. 5.1) presents the following main features:

- pressure range: up to 7 MPa and temperature range: 286 °C respectively,
- inner diameter: 193.7 mm,
- 64 x 64 orthogonal wires -> 3260 measuring points over the cross-section,
- diameter of the wires: 250 µm,
- distance between the wires: 3 mm as well as between the two wire-planes: also 3 mm.

Every wire is electrical insulated against the remaining wires and against the body of the sensor. At each measuring point, the electrical conductivity between the

transmitter and the receiver electrodes (wires) of the circumfluent medium is determined. These analog values are sampled and converted by a special electronic device connected to the sensor. After the measurement, the digital data is copied on a PC where it is stored for further processing.

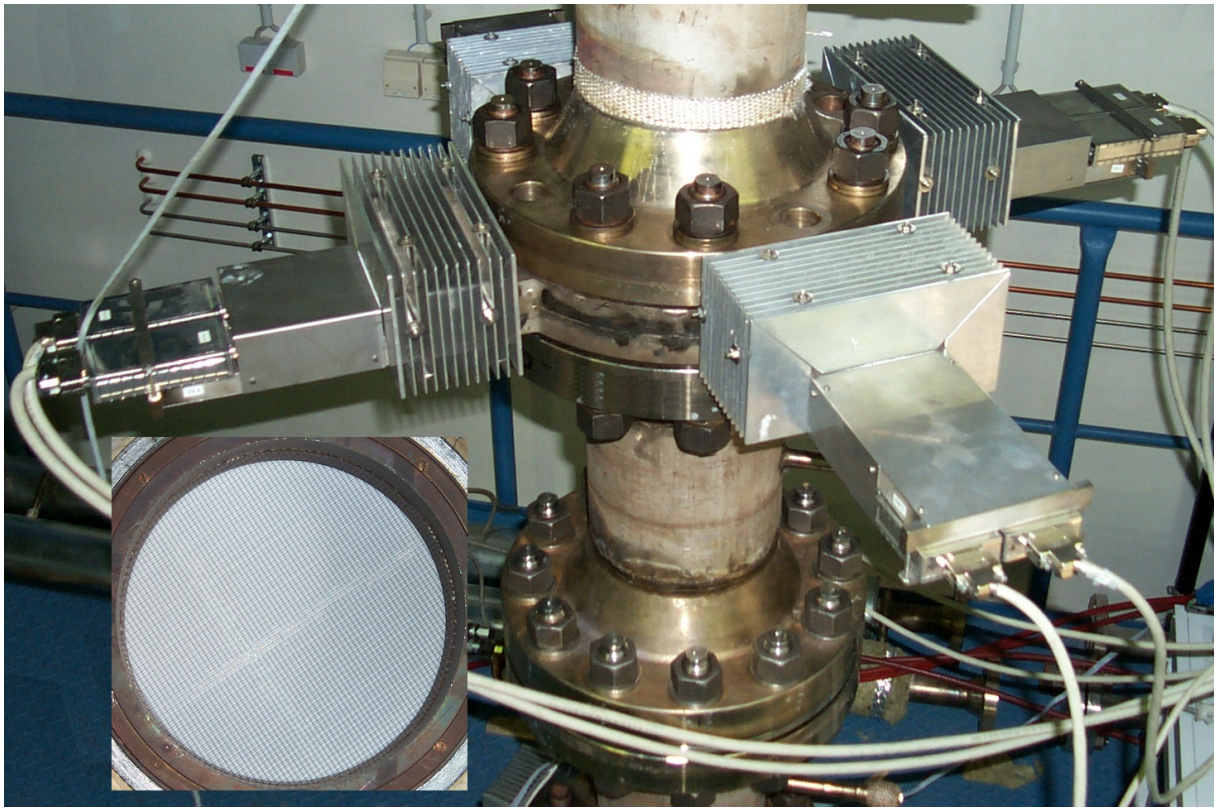

Fig. 5.1 Mounted high-pressure wire-mesh sensor DN200, dimensions of the measuring matrix 64x64

To reduce noise, the electronic device was galvanically isolated from the mains supply and the mesh sensor solidly grounded. A detailed description of the construction and function of wire-mesh sensors is given by Scholz (2000), Prasser et al. (2001), Pietruske et al. (2005). These are a proprietary development of the FZD and are partly own manufactured. The electronic device and the corresponding measuring software are developed and produced in co-operation with the TELE-TRONIC company (www.tz-rotech.de/teletronic/).

The quality of the void fraction measurement with wire-mesh sensors may be estimated by comparison with other measuring techniques. The gamma radiation through an air/water flow with variable superficial velocities of both media and volume void fraction between 0 and 100% were done. These experiments showed a maximum deviation between the wire-mesh sensor and the gamma radiation of ±5% (Prasser, 2000). The radiation of a steam/water flow under ambient conditions confirms this statement (Manera et al., 2001). This error band is quiet large, because the gamma ray measurement was not very precise.

Therefore, tests in an air/water flow were performed with the mesh sensor technology and an X-ray tomograph. The X-ray tomography is known as a more sensitive technique than gamma radiation. A comparative analysis of the results showed that the accuracy of the void fraction averaged over the cross-section depends on the

flow regime. Following differences on the absolute void fraction were found by Prasser et al. (2005c):

- in a bubbly flow: ±1% and
- in a plug flow a systematically underestimation of ca. -4%.

Furthermore, high-speed video observations were performed by Scholz (2000) to evaluate the measurement of the equivalent volume-equal bubble diameter with the wire-mesh sensor. It demonstrates the reliable detection of bubble diameters, larger or equal then the distance between the wire planes.

In order to get sufficient information for the assessment of the flow structure, the measurements are carried out for 10 seconds under steady state conditions with the maximum frequency of 2500 frames per second. The operating conditions (i.e. mass flow, pressure, temperature), necessary for the evaluation of measuring data, are copied from the process control system of the facility and recorded with the software DIAdem (see Beyer et al., 2004). For the synchronisation of the measurements with the related operating conditions is used the start-trigger sent by the process control system to the wire-mesh sensor electronic device. This trigger and, additionally, the measuring period are stored in the matrix of DIAdem.

6. CFX Pre-Test Calculations

Before the experiments were commissioned, a pre-test calculation was set-up for the boundary conditions of the air-water test 074, which was performed at the superficial velocities J_L = 1.0 m/s and J_G = 0.037 m/s. Flow conditions correspond to the bubbly flow regime. For the CFD simulation with ANSYS CFX 10.0 the Eulerian two-phase flow model was used (see ANSYS, 2005 and Frank et al., 2004), assuming that the gaseous phase consists of monodisperse bubbles with a pipe elevation dependent equivalent diameter of 4.8-5.2 mm in order to account for the hydrostatic bubble expansion. Both phases were treated as non-compressible, i.e. while the bubble diameter changes with the pipe elevation, the increase of the gas volume fraction caused by pressure decrease is neglected. Bubble drag in accordance to Grace drag law, Tomiyama lift force, Frank's generalized wall lubrication force and the FAD turbulent dispersion force have been taken into account (Frank, 2006). Bubble coalescence and fragmentation were neglected for this first pre-test simulation, also it can be assumed that bubble fragmentation will take place at the edges of the obstacle and coalescence might become of importance in regions of bubble accumulation i.e. in the wake behind the obstacle.

Steady state simulations with ANSYS CFX 10.0 were performed on two numerical meshes created with ICEM CFD Hexa and consisting of about 119.000 and 473.000 hexahedral mesh elements. Meshes were generated for half of the TOPFLOW geometry assuming axial symmetry. The flow domain for the CFD simulation consisted in two 1.5 m long pipe sections situated upstream and downstream of the obstacle. Inlet boundary conditions were set to fully developed two-phase pipe flow profiles for air and water velocities, radial gas volume fraction distribution, turbulent kinetic energy and turbulent eddy frequency. At the outlet cross-section of the 3.0 m long pipe section an averaged static pressure outlet boundary condition was used.

7. Evaluation of wire-mesh sensor data

7.1 Time averaged void fraction distributions

The wire-mesh sensor supplies a time sequence of instantaneous local gas fraction distributions within the measuring cross-section (Fig. 5.1). At each crossing point of wires belonging to different electrode planes of the sensor a control volume with the indexes i,j is formed, from which a gas fraction value $\varepsilon_{i,j,k}$ is delivered for each time sample k. The relation between the indexes i, j, k and the coordinates as well as the time are:

$$x = i \cdot \Delta x;\ y = j \cdot \Delta y;\ t = k \cdot \Delta t \ \ = k \big/ f_{sample} \tag{1}$$

When the local values are averaged over the total measuring time (in this case 10 s, or, respectively, from k = 1 to k = k_{max}), a two-dimensional void fraction distribution is obtained:

$$\bar{\varepsilon}_{i,j} = \frac{1}{k_{\max}} \sum_{k=1}^{k_{\max}} \varepsilon_{i,j,k} \tag{2}$$

If it is assumed that the translation of the diaphragm with respect to the sensor position can be approximately envisaged as a scan of the three-dimensional void distribution around the diaphragm, then the distributions measured for each of the distances given in chapter 5 can be combined to result in a full three-dimensional void fraction field around the obstacle.

7.2 Bubble size distributions

Due to the spatial resolution, it is possible to identify individual bubbles in the sensor signal. A bubble is a region of interconnected gas containing elements of the data array $\varepsilon_{i,j,k}$ that is surrounded by elements filled with the liquid phase. The operation of the bubble identification described by Prasser (2004b) results in a second three-dimensional array $b_{i,j,k}$, which assigns unique identification numbers specific for each bubble to each element of the distribution $\varepsilon_{i,j,k}$.

Both arrays $\varepsilon_{i,j,k}$ and $b_{i,j,k}$ are used to calculate equivalent diameters of the bubbles. The volume of a bubble with the identification number n is calculated as follows:

$$V_{bub,n} = \Delta x \Delta y \Delta t \cdot w_{bub} \sum_{i,j,k} \varepsilon_{i,j,k} \quad \forall [i,j,k] : b_{i,j,k} = n \tag{3}$$

This volume can be transformed into an equivalent diameter of the bubble:

$$\mathrm{D}_{\mathrm{equ,n}} = \sqrt[3]{\frac{6\mathrm{V}_{\mathrm{bub,n}}}{\pi}} \tag{4}$$

As it can be seen from eq. (3), the extraction of a volume-equivalent diameter D_{equ} requires information about the bubble velocity. This is necessary to specify the extension of the control volume formed by a crossing point of electrode wires of the sensor, which is equal to the area $\Delta x \cdot \Delta y$ within the measuring plane, multiplied by the distance the bubble travels during the sampling period Δt, which is equal to $\Delta t \cdot w_{bub}$.

If the bubble velocity is not available, the size of the bubbles can be characterized by the diameter of a circle D_{xy} equivalent to the maximum area occupied by the bubble in the measuring plane during its passage through the sensor. The equivalent

diameter D_{xy} characterizes the lateral extension of a bubble (Prasser et al., 2005a and Pietruske et al., 2005). The area occupied by a bubble at an instant given by the index k is

$$A_{xy,n,k} = \Delta x \Delta y \sum_{i,j} \varepsilon_{i,j,k} \quad \forall [i,j,k] : b_{i,j,k} = n \tag{5}$$

The equivalent diameter in the x,y-direction is calculated from the maximum area:

$$D_{xy,n} = \sqrt{\frac{4 A_{xy,n,\max}}{\pi}} \quad where \quad A_{xy,n,\max} = \max\left(A_{xy,n,k}\right) \tag{6}$$

The equivalent diameter D_{xy} is an alternative to the diameter of the equivalent sphere for characterizing the structure of the two-phase flow, when only a single wire-mesh sensor is available, as it was the case in the presented experiments.

Bubble size distributions are constructed by integrating the gas fraction carried by each individual bubble over classes of bubble diameters. These histograms represent distributions of the partial void fraction over the bubble diameter. Their unit is 1/mm or %/mm:

$$H_{bub} = \frac{\Delta \varepsilon}{\Delta D_{xy}} = f\left(D_{xy}\right), \quad [\%/mm] \tag{7}$$

7.3 Liquid velocity profile

There is a way to assess time-averaged liquid velocity distributions by evaluating the transit time of bubbles through the measuring plane of the sensor. For a hypothetical spherical bubble shape, the diameter in all three co-ordinate directions would be identical. The deviation from the spherical shape can be taken into account by a calibration factor C. On basis of the bubble identification algorithm and the bubble diameter measurement described in the previous section, the bubble velocity can be expressed as follows:

$$w_{bub,n} = C \cdot \left(\frac{D_{xy,n}}{\widetilde{D}_{equ,n}} \right)^3 = C \cdot \widetilde{w}_{bub,n} \tag{8}$$

where $\widetilde{D}_{equ,n} = \sqrt[3]{\frac{6\widetilde{V}_{bub,n}}{\pi}}$ is a auxiliary equivalent diameter, calculated without involving the bubble velocity, i.e. $\widetilde{V}_{bub,n} = \Delta x \Delta y \Delta t \sum_{i,j,k} \varepsilon_{i,j,k} \quad \forall [i,j,k] : b_{i,j,k} = n$. The dimension of $\widetilde{D}_{equ,n}$ is $(mm^2 \cdot s)^{1/3}$. In eq. (8) $\widetilde{w}_{bub,n}$ is the bubble velocity without the correction accounting for the deviation from the spherical shape.

The degree of deformation of a bubble depends on the bubble size, when the physical properties of the fluids are constant. For bubbles from a narrow region of equivalent diameters of $D_{MB,1} \le D_{xy} \le D_{MB,2}$, which we call “marker bubbles”, it can be assumed that the calibration factor C is constant and independent of the location within the measuring cross-section. The same holds for the rise velocity of the bubbles Δw_{bub} relative to the liquid velocity. A time-averaged two-dimensional velocity distribution of the marker bubbles is found using the local instantaneous gas fraction as a weight function. Those elements that belong to bubbles outside the size interval defined for marker bubbles are ignored:

$$\overline{w}_{MB,i,j} = \frac{1}{\overline{\varepsilon}_{i,j} \cdot k_{\max}} \sum_{k=1}^{k_{\max}} \begin{cases} \widetilde{w}_{bub,b_{i,j,k}} \cdot \varepsilon_{i,j,k} & if \quad D_{MB,1} \le D_{xy,b_{i,j,k}} \le D_{MB,2} \\ 0 & elsewhere \end{cases} \tag{9}$$

Due to the constancy of the calibration factor and the bubble rise velocity, the local time averaged liquid velocity can be written as follows:

$$\overline{v}_{L,i,j} = C \cdot \overline{w}_{MB,i,j} - \Delta w_{bub} \tag{10}$$

In eq. (10) all deviations of the bubble rise velocity relative to the liquid phase due to local acceleration of the fluid as well as bubble swarm effects are neglected. In a strict sense, eq. (10) is valid only for bubbles rising in resting liquid at low void fractions. It was decided not to account for these effects and to restrict the evaluation to an approximate assessment of the liquid velocity and the velocity distributions, because the assumption of the constancy of the calibration factor for itself is a quite rough approach leading to considerable uncertainties. The reliability of the obtained velocity profiles is discussed in a separate section of uncertainty analysis (see section 10).

The calibration factor can be obtained by reconstructing the interfacial liquid velocity from the two-dimensional profiles of velocity and gas fraction and comparing the result to the known superficial liquid velocity in the test pipe:

$$J_L = \sum_{i,j} a_{i,j} \cdot \overline{v}_{L,i,j} \cdot \left(1 - \overline{\varepsilon}_{i,j}\right) = \left\langle \overline{v}_{L,i,j} \cdot \left(1 - \overline{\varepsilon}_{i,j}\right) \right\rangle \tag{11}$$

Where $a_{i,j}$ are weight factors defining the share of the total measuring cross-section which is represented by the local control volume of the sensor with the indexes i,j. The symbol $\langle\ \rangle$ denominates a spatial averaging over the measuring cross-section. For an arbitrary quantity distributed over the measuring cross-section, the averaging is performed as follows:

$$\left\langle x_{i,j} \right\rangle = \sum_{i,j} a_{i,j} \cdot x_{i,j} \tag{12}$$

After combining eq. (10) and eq. (11), the calibration factor can be made explicit:

$$C = \frac{J_L + \Delta w_{bub}\left(1 - \left\langle \overline{\varepsilon}_{i,j} \right\rangle\right)}{\left\langle \overline{w}_{MB,i,j} \right\rangle - \left\langle \overline{w}_{MB,i,j} \cdot \overline{\varepsilon}_{i,j} \right\rangle} \tag{13}$$

After the calibration, a liquid velocity distribution is calculated using eq. (10). The calibration factor can only determined in the described way when the two-dimensional measuring plane is free from regions with flow recirculation. In case of the experiments with the movable diaphragm, this can be guaranteed only when the sensor was located upstream the diaphragm. As the experimental results shows, the flow downstream of the half-moon shaped plate was often affected by a large recirculation area. Since the marker bubble method does not distinguish between upwards and downwards motion of bubbles, in both cases, a positive velocity is measured. In the result, the superficial liquid velocity in such a cross-section is overestimated by eq. (11) for given velocity and gas fraction profiles, because for a correct integration of the superficial velocity the velocity in the downwards flow regions within the cross-section enter with a positive instead of a negative sign. Consequently, the calibration factor obtained after the transformations is under-

estimated. For this reason, a calibration according to eq. (13) was performed only for negative distances between sensor and diaphragm, namely for Δz = -520, -250, -160, -80, -40, -20, -15, -10 mm. The individual calibration factors were averaged and the average factor was applied also for the positive distances Δz = 10, 15, 20, 40, 80, 160, 250, 520 mm. In order to keep the bubble deformation and the bubble rise velocity in a narrow band, the interval for the diameter of the marker bubbles was set to 4 - 5 mm. First, this is a compromise between the tendency to make marker bubbles as small as possible to approach the spherical shape as much as possible, and the advantage of bubbles around 6 mm equivalent diameter, for which the rise velocity is nearly bubble-size independent (Fig. 7.1). Secondly, the limits have to be defined in a way, that there are still enough bubbles found in the selected interval.

In Fig. 7.1, the rise velocity is shown as a function of the equivalent bubble diameter as well as of the maximum diameter of the bubble that is in reality deformed. The correlation of Wellek (Wellek et al., 1966) was used to predict the maximum diameter of the ellipsoidal bubble as a function of the Eötvös number. The diameter in x,y-direction which was used to characterize the bubble size for this method, lies between the equivalent diameter and the maximum diameter according to Wellek. For both extreme values of the diameter, the bubble rise velocity is nearly the same and has a value of about 0.235 m/s, which was used in eq. 10 and 13.

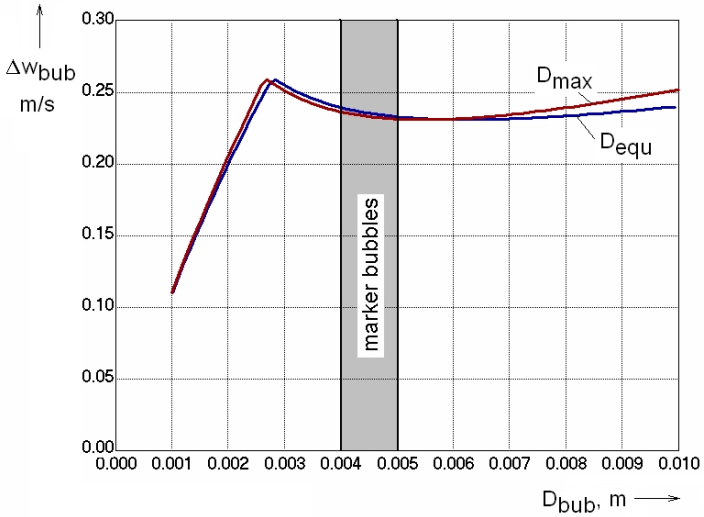

Fig. 7.1 Relative bubble rise velocity calculated on basis of the drag force as a function of the equivalent and the maximum bubble diameter, see Schiller et al. (1933)

7.4 Void fraction distributions decomposed according to bubble size classes

The assignment of bubble numbers $b_{i,j,k}$ to the elements of the local instantaneous gas fraction array $\varepsilon_{i,j,k}$ allows to calculate bubble-size selective time averages of the void fraction:

$$\bar{\varepsilon}_{i,j,[D_1,D_2]} = \frac{1}{k_{\max}} \sum_{k=1}^{k_{\max}} \varepsilon_{i,j,k} \quad \forall [i,j,k] : b_{i,j,k} = n \;\&\; D_{xy,n} \in [D_1, D_2] \tag{14}$$

These bubble-size resolved void fraction distributions grant access to the spatial non-uniformity of the flow structure. They can either be plotted as distributions of the void fraction for selected bubble-size classes or as local bubble size distribution.

7.5 Assessment of lateral bubble velocities

The attempt was made to get a rough estimate for the movement of the bubbles within the measuring plane of the sensor. Due to the asymmetric obstruction of the pipe, the flow cannot be considered axially parallel, i.e. significant lateral components for both gas and liquid velocities have to be expected, which are most pronounced in

the direct vicinity of the diaphragm. In fact, a visualization of time sequences of two-dimensional instantaneous gas fraction distributions captured by the wire-mesh sensors show lateral movements of bubbles while they cross the measuring plane. Unlike the estimation of the axial velocity which needed the use of the marker-bubble method described above, the estimation of the lateral velocity of a bubble was made by directly tracking the transversal movement of the centre of mass of its two-dimensional image. When some bubble passes the wire mesh it will be divided axially into several slices in the measuring plane. Each slice corresponds to a measuring time step i. The points belonging to a specific bubble are identified by the bubble number n, i.e. an element with the indices i,j,k belongs to bubble n if $b_{i,j,k} = n$. The centre of mass of each slice of the bubble can be found by averaging the x and y coordinates of each element that belongs to the given bubble weighted by the local instantaneous gas fraction $\varepsilon_{i,j,k}$:

$$x_{CM,n}(t) = \frac{\sum_{\forall i,j:b_{i,j,k}=n} \varepsilon_{i,j,k} \cdot i \cdot \Delta x}{\sum_{\forall i,j:b_{i,j,k}=n} \varepsilon_{i,j,k}} \qquad y_{CM,n}(t) = \frac{\sum_{\forall i,j:b_{i,j,k}=n} \varepsilon_{i,j,k} \cdot j \cdot \Delta y}{\sum_{\forall i,j:b_{i,j,k}=n} \varepsilon_{i,j,k}} \quad \text{where } t = \Delta t \cdot k \tag{15}$$

The components $v_{x,n}$ and $v_{y,n}$ of the velocity of bubble n are found by a linear regression of the available time sequence of coordinates of the centre of mass during the bubble passage. The result of the linear fit is presented in the form:

$$x_{CM,n}(t) = v_{x,n} \cdot t + c_x \qquad y_{CM,n}(t) = v_{y,n} \cdot t + c_y \tag{16}$$

where the constants c_x and c_y are meaningless. To obtain an average gas velocity in every point (i,j) of the plane, void fraction weighted time-averages of these two quantities were calculated over all bubbles found during the total measuring period ($t_{meas} = 10s = \Delta t \cdot k_{max}$):

$$\bar{v}_{G,x}(i,j) = \frac{1}{\sum_{k=1}^{k_{max}} \varepsilon_{i,j,k}} \cdot \sum_{k=1}^{k_{max}} \left\{ \begin{matrix} \varepsilon_{i,j,k} \cdot v_{x,b_{i,j,k}} \; if \; b_{i,j,k} \neq 0 \\ 0 \; if \; b_{i,j,k} = 0 \end{matrix} \right\} \tag{17a}$$

$$\bar{v}_{G,y}(i,j) = \frac{1}{\sum_{k=1}^{k_{max}} \varepsilon_{i,j,k}} \cdot \sum_{k=1}^{k_{max}} \left\{ \begin{matrix} \varepsilon_{i,j,k} \cdot v_{y,b_{i,j,k}} \; if \; b_{i,j,k} \neq 0 \\ 0 \; if \; b_{i,j,k} = 0 \end{matrix} \right\} \tag{17b}$$

The resulting time-averaged velocities provide an estimation of the lateral velocity field. This calculation was made for all available distances upstream and downstream of the diaphragm.

8. Experimental results

8.1 Typical observations

The discussion of results in the following chapters is focused on some selected test points. A complete series of plots of all test points as well as a description of the data files and file name conventions is added in the attachments A - C.

A quite typical flow field is found in the air-water test 097 at J_G = 0.09 m/s and J_L = 1.6 m/s (Fig. 8.1). The figure presents void fraction and velocity distributions at a plane that represents a central cut along the pipe axis, perpendicularly to the linear edge of the half-moon shaped diaphragm. Furthermore, two-dimensional distributions in each of the 16 measuring planes are given, together with a graphical indication of their axial location.

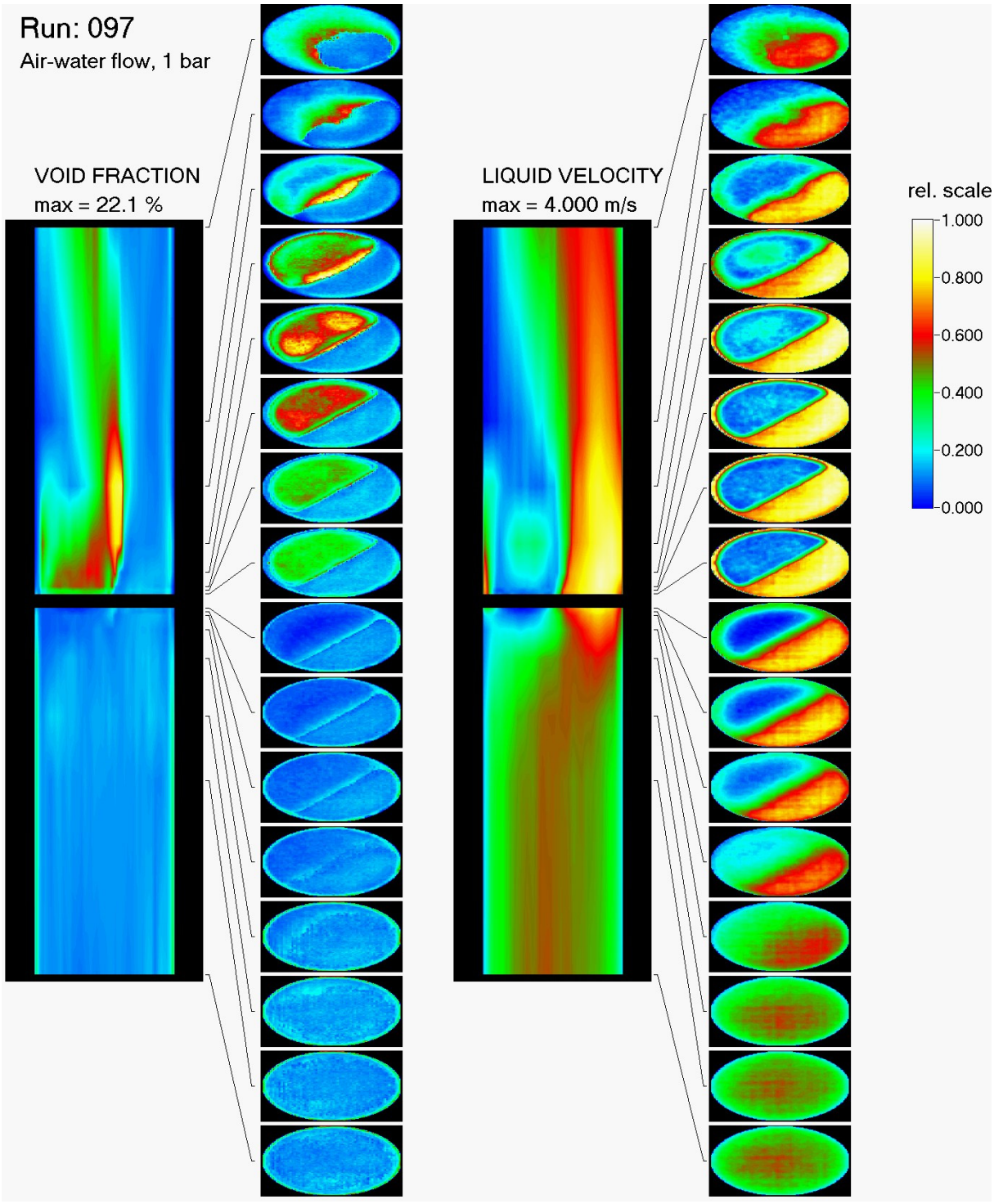

Fig. 8.1 Time averaged void fraction and liquid velocity distributions up- and downstream of the obstacle in the air-water test run 097, J_L = 1.611 m/s, J_G = 0.0898 m/s

The undisturbed flow at the conditions of this test is characterized by a wall peak of the void fraction profile, which can be found up to the axial position 160 mm upstream of the diaphragm. Closer to the diaphragm, i.e. 80 mm upstream of it, the influence of the cross-section obstruction becomes evident. The velocity profile becomes asymmetric with a more and more pronounced maximum on the unobstructed side.

On the front side of the diaphragm a stagnation point is clearly visible in the velocity plot. In the same time, this region shows a local minimum of the void fraction. On the curved stream lines upstream of the stagnation point, the fluid experiences a strong acceleration. In the result, the heavier phase, i.e. the water, is accumulated and the gaseous phase is moved out of the stagnation region.

High velocities are found both in the unobstructed part of the pipe cross-section as well as in the 10 mm wide gap between the circular edge of the obstacle and the pipe wall on the other side. The flow separates from the edge of the diaphragm and a high velocity jet downstream of the obstacle is formed. On the side of the unobstructed half of the cross-section, the jet ranges beyond the end of the measuring domain, i.e. the equilibrium profile found 520 mm upstream of the obstacle is not re-established at the distance of 520 mm downstream. The jet is slightly bended towards the obstructed side of the pipe. It can be concluded that fully developed flow profiles require an inlet length of much more than L/D = 2.5 to establish. A velocity peak is also found downstream of the 10 mm wide circular gap between obstacle and pipe wall on the side opposite to the main jet, though this maximum vanishes after about L/D = 1.

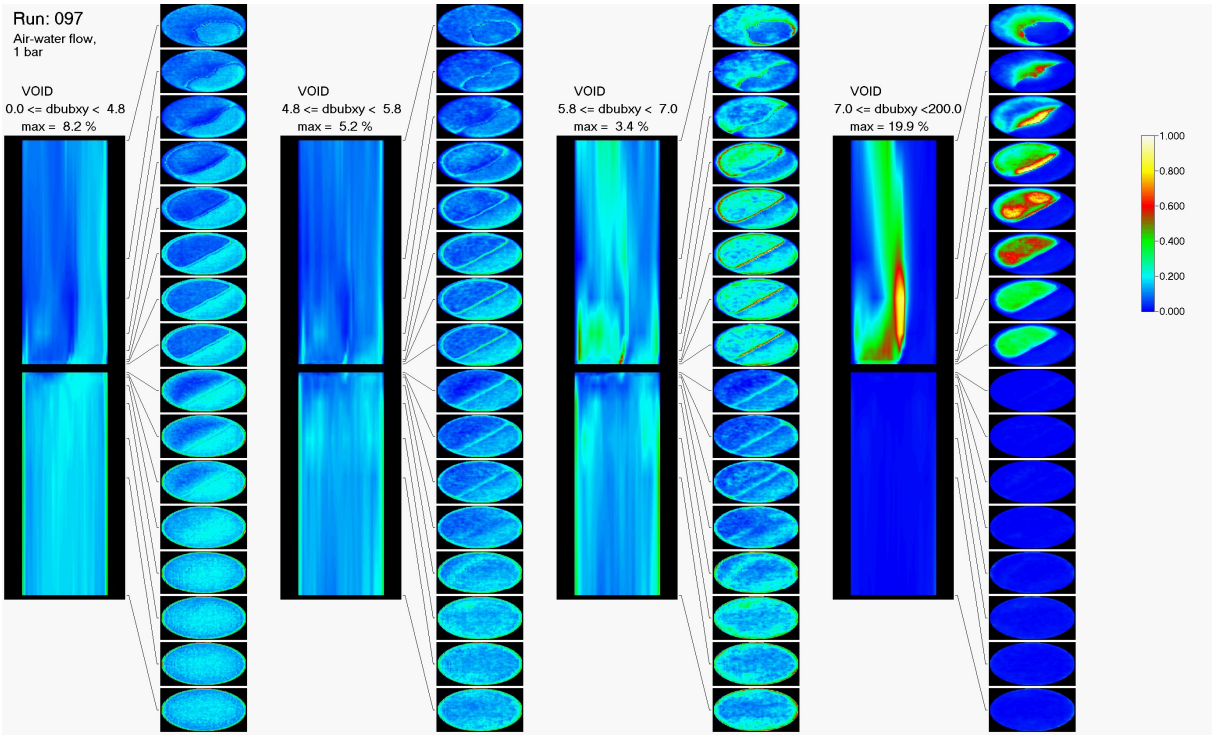

Fig. 8.2 Time averaged void fraction distributions decomposed in bubble-size classes up- and downstream of the obstacle in the air-water test run 097, J_L = 1.611 m/s, J_G = 0.0898 m/s, T = 30 °C

Both high velocity regions show low void fractions. The former wall peak of the void fraction profile remains on the unobstructed side, while it almost vanishes on the side

of the obstacle. Upstream of the diaphragm there is a void maximum formed that nearly follows the linear edge of the half-moon plate. It is presumably caused by a repelling action of the lift force caused by the strong velocity gradient at the boundary of the jet that starts to form. Later, downstream of the obstacle, a similar effect is found again, causing a quite complicated two-dimensional gas fraction distribution. On the one hand side, there is a stripe of gas accumulation everywhere, where a boundary to a high velocity region is present. In the end, this results in a hole in the void fraction distribution 520 mm above the obstacle, which can be qualified as a coherent structure, which is probably caused by the repelling effect of the lift force. Later it will be shown that this structure is not found in experiments with steam-water mixture at high pressure. This finding supports the hypothesis of the dominating effect of the lift force, since the lift force reversal according to Tomiyama shifts towards smaller bubble sizes when pressure and temperature are increased, compare Tomiyama et al. (1995) and Tomiyama et al. (1998).

A look into the present bubble sizes nevertheless reveals peculiarities compared to the findings of Tomiyama. Void fraction distributions decomposed into bubble size classes are shown in Fig. 8.2. It is clearly visible that the obstacle provokes a growth of bubbles, since lateral diameters of larger then 5.8 mm scarcely found upstream of the diaphragm become dominating in the wake of the obstacle. Even bubbles that are much larger than the critical diameter according to Tomiyama cannot enter the almost bubble-free jet still observed at 520 mm above the obstacle. This effect requires further investigation. Furthermore it can be seen that the earlier mentioned double-peak in the two-dimensional void fraction distribution at the position 40 mm downstream of the obstacle is mainly caused by bubbles of more than 7 mm lateral diameter.

On the other hand, there is a strong gas fraction maximum, corresponding to an elliptical region with a local velocity maximum at about L/D = 0.5 straight above the obstacle, which is obviously a recirculation area. This can be deduced from the superficial liquid velocities calculated using eq. (11). When this value is plotted as a function of the axial location (Fig. 8.3), it is found that the reconstructed superficial velocity significantly exceeds the set value known from the boundary conditions of the test. Remember, that the calibration coefficient was kept constant and equal to the value obtained as an average for all level upstream of the obstacle, i.e. where recirculation regions can be excluded. The fact that a maximum, and not a minimum is seen, is caused by the fact that the marker bubble method is not sensitive to the direction of the bubbles. The bubble velocities estimated by relating the lateral extension of the bubbles to their

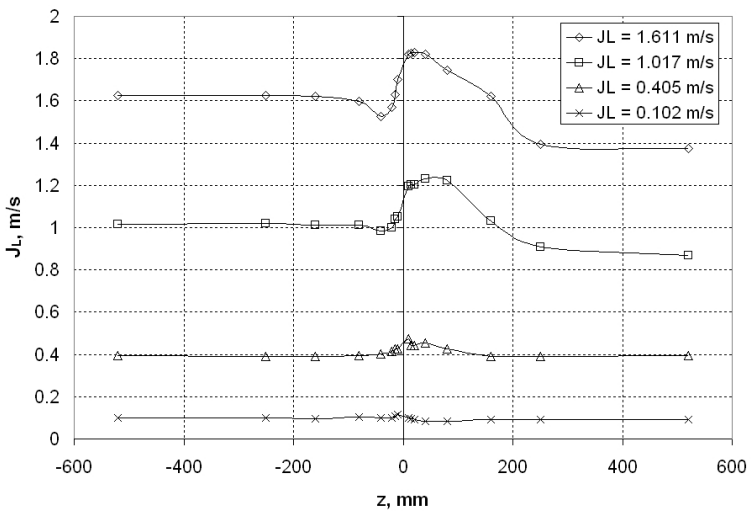

Fig. 8.3 Reconstructed superficial liquid velocities as a function of the distance between obstacle and sensor for the air-water tests 091, 094, 096 and 097 at J_G = 0.0898 m/s

passage time are always positive. Therefore, in a recirculation area a local maximum is found. If a part of the cross-section is affected by downwards flow, the volume flow rate in this region is added to the flow rate in the upwards flow region and the reconstructed superficial velocity is systematically overestimated.

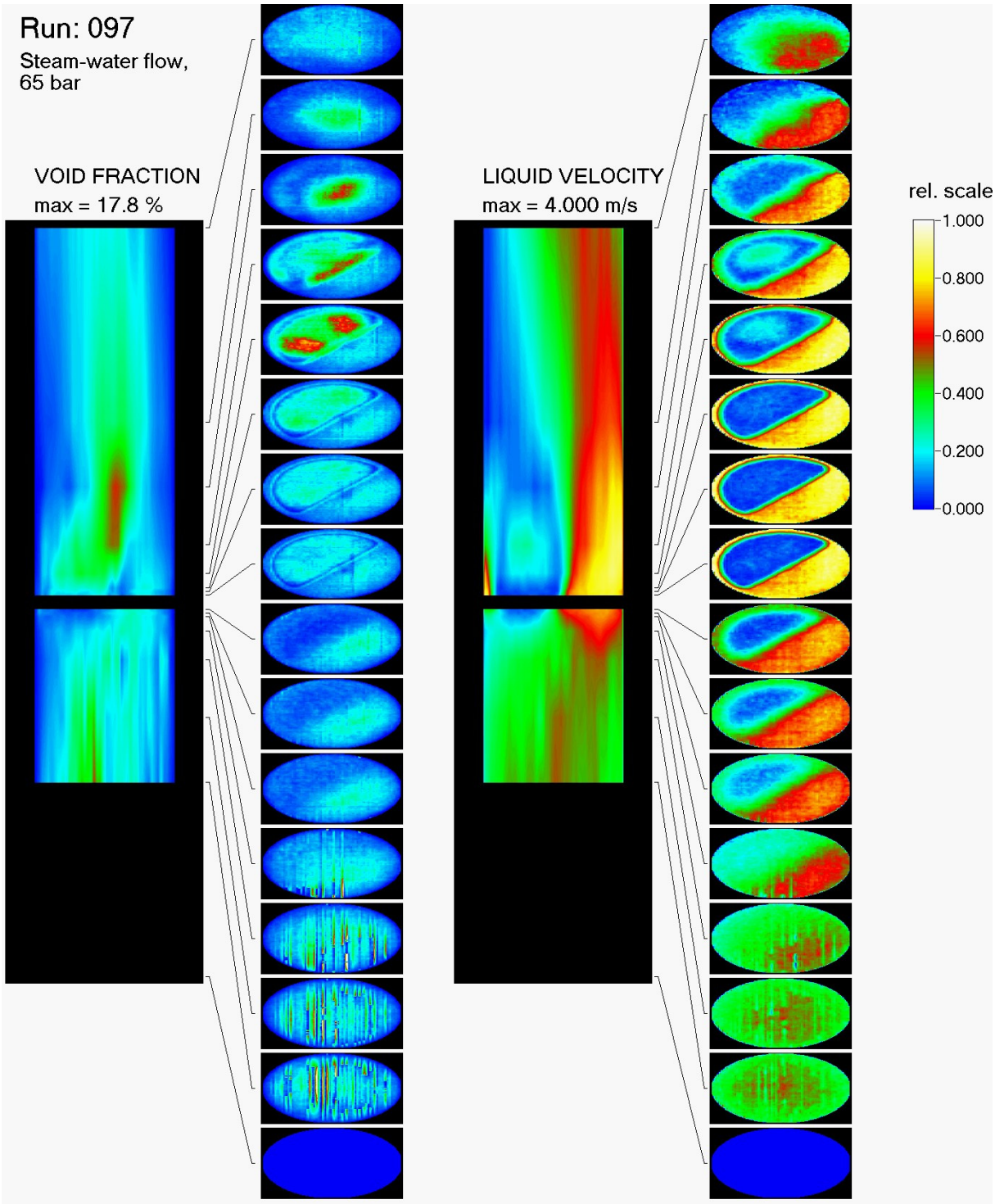

Fig. 8.4 Time averaged void fraction and liquid velocity distributions up- and downstream of the obstacle in the steam-water test run 097 at 6.5 MPa, J_L = 1.611 m/s, J_G = 0.0898 m/s (at injection position)

The strong accumulation of the gaseous phase observed within the recirculation area reaches its absolute maximum of the void fraction is found 160 mm downstream.

Bubbles with a lateral diameter of less than 4.8 mm do not contribute to the gas accumulation in the recirculation region. Close to the obstacle (at z = 20 mm), the gas accumulation covers almost the entire backside of the half-moon shaped plate. More downstream, the bubbles are transported towards the central region of the pipe. At the position 40 mm above the obstacle, the gas fraction distribution clearly shows two large maximum regions, which are outside the centre plane and therefore do not appear in the centre plane plot.

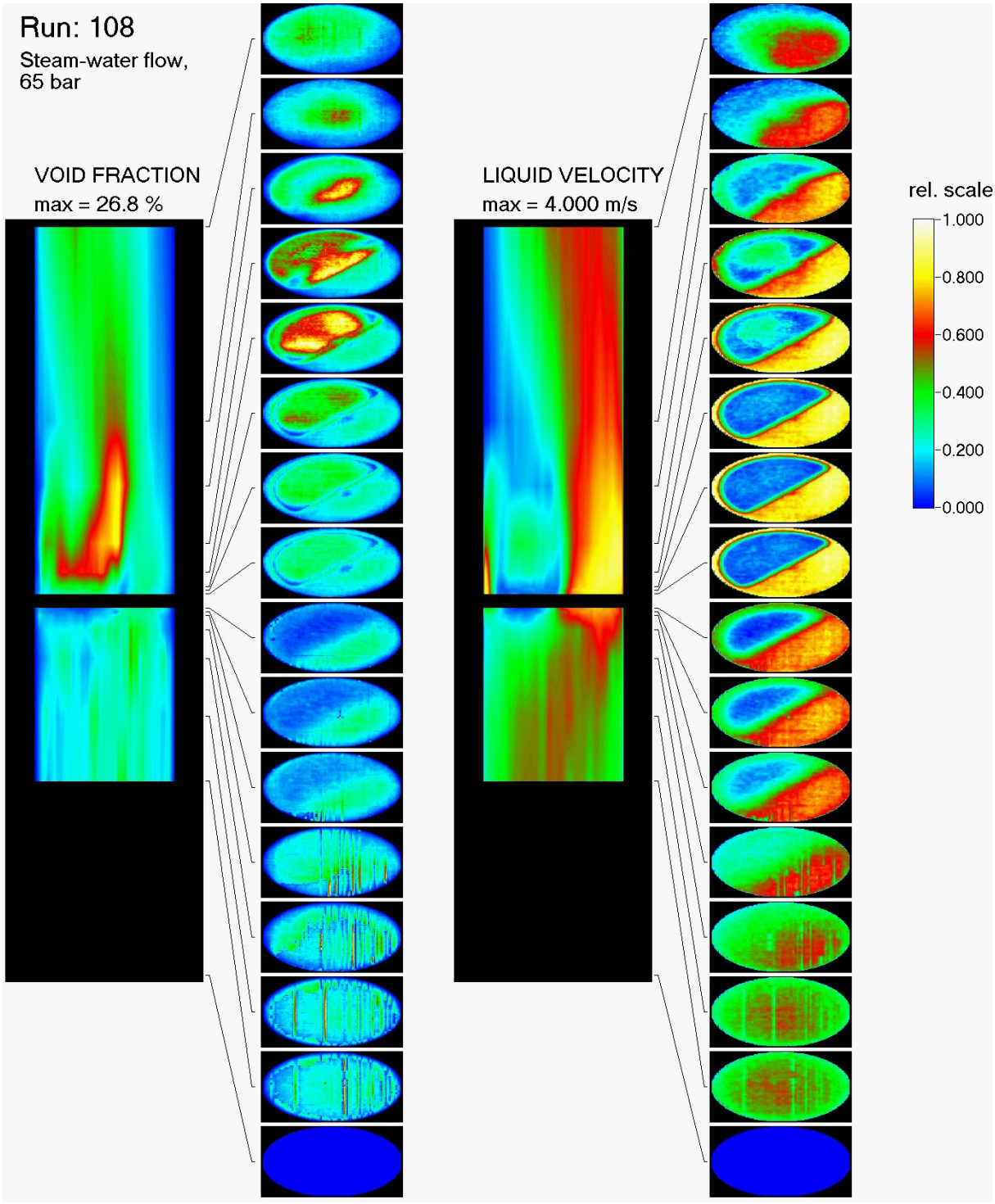

Fig. 8.5 Time averaged void fraction and liquid velocity distributions up- and downstream of the obstacle in the steam-water test run 108 at 6.5 MPa, J_L = 1.611 m/s, J_G = 0.140 m/s (at injection position)

Fig. 8.4 in general shows similar structures of the void fraction and velocity distributions despite of already mentioned the fact that the hole in the void fraction distributions 520 mm downstream of the obstacle is not observed.

The overall void fraction is significantly lower, which has to be attributed to some steam condensation occurring in the test section. This is due to a sub-cooling of the liquid phase, which is inevitably caused by the pressure drop in the test section and the pipe connecting it to the steam drum, where finally saturation conditions are present.

A better agreement of the overall void fraction is achieved in test 108, that was carried out at an identical superficial liquid velocity, but at a higher steam injection of J_G = 0.14 m/s (Fig. 8.5). In both tests 097 and 108, the initial void fraction distribution at z = - 250 mm is characterized by a central peak in contrast to the wall peak found in the air-water experiments. This is another consequence of the shift of the lift force reversal to smaller bubble diameters at higher temperatures according to Tomiyama (Tomiyama et al., 1995 and Tomiyama, 1998). Void fraction distributions for the test 108 decomposed according to bubble-size classes are shown in Fig. 8.6.

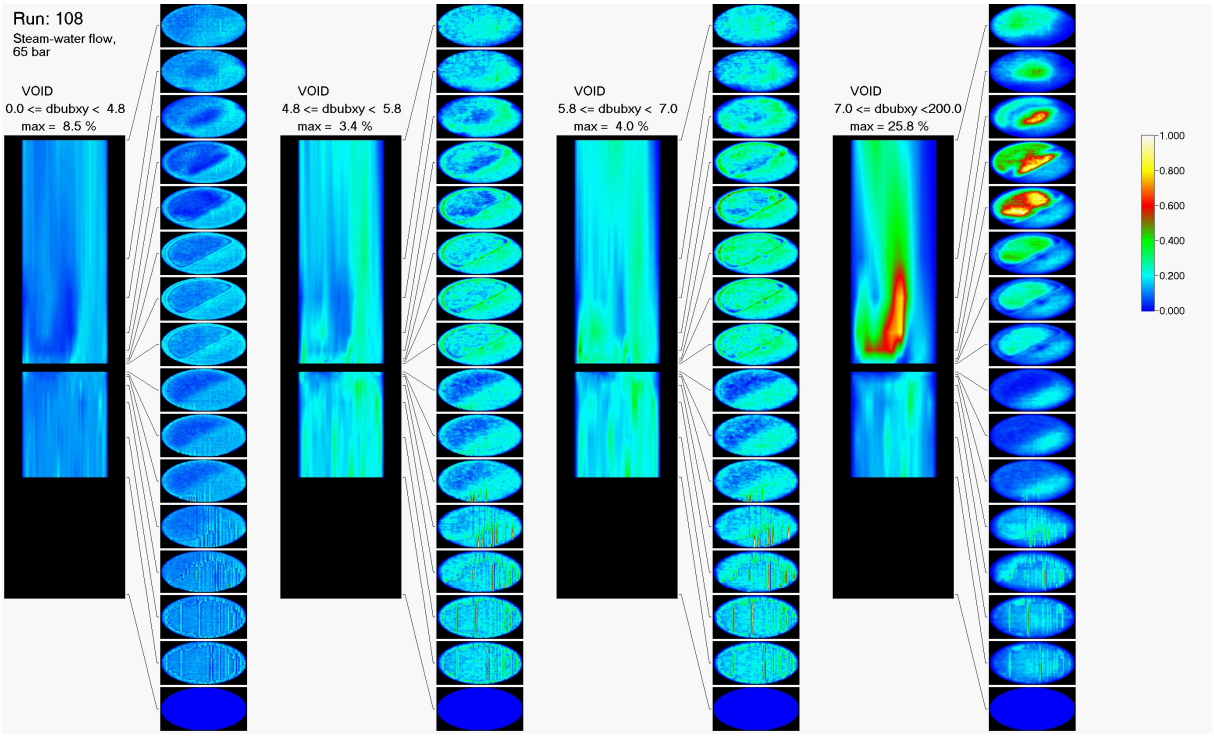

Fig. 8.6 Time averaged void fraction distributions decomposed in bubble-size classes up- and downstream of the obstacle in the steam-water test run 108 at 6.5 MPa, J_L = 1.611 m/s, J_G = 0.140 m/s (at injection position)

8.2 Tendencies with changing superficial liquid velocity

When, starting from the air-water test 097, the superficial liquid velocity is decreased, while the superficial air velocity is kept constant at J_G = 0.09 m/s, then some qualitative changes in the structure of the void fraction distributions is observed (Fig. 8.7). Due to the decrease of the velocity gradient at the pipe wall, the wall peaked profile in the undisturbed region upstream of the obstacle is no more found at liquid velocities below 1 m/s. For similar reasons, the oval region depleted from gas

520 mm above the obstacle is no more found in the tests 094 (J_L = 0.4 m/s) and 091 (J_L = 0.1 m/s), while it is still present in test 096 at J_L = 1.0 m/s.

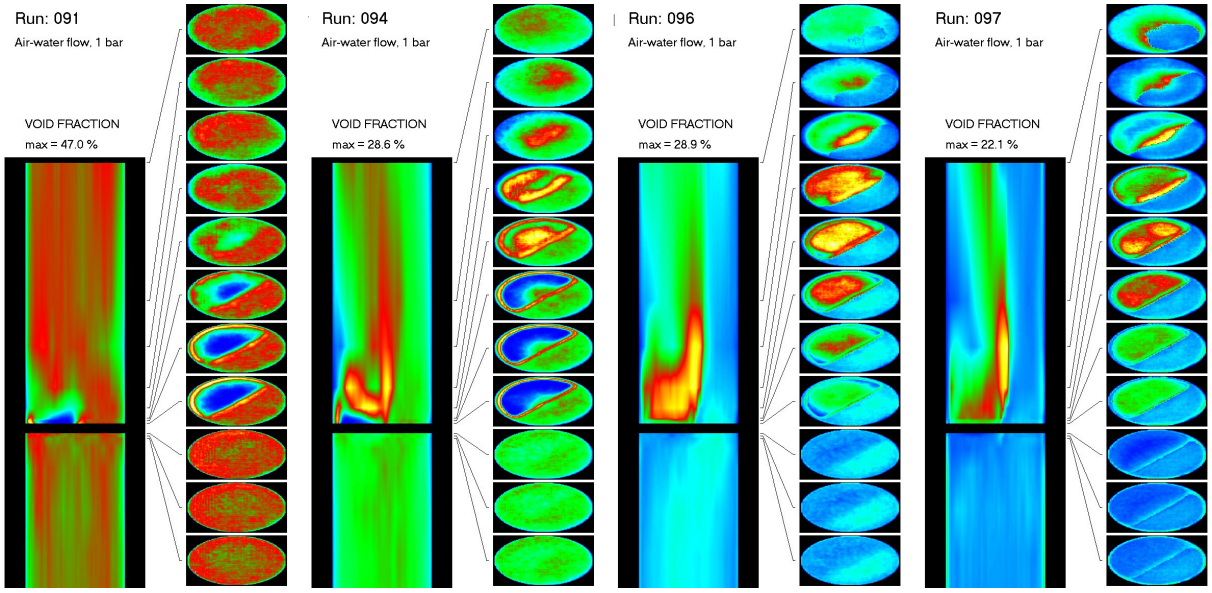

Fig. 8.7 Effect of the variation of the superficial liquid velocity on the time averaged void fraction distributions up- and downstream of the obstacle in the air-water test runs 091, 094, 096 and 097 at J_G = 0.0898 m/s

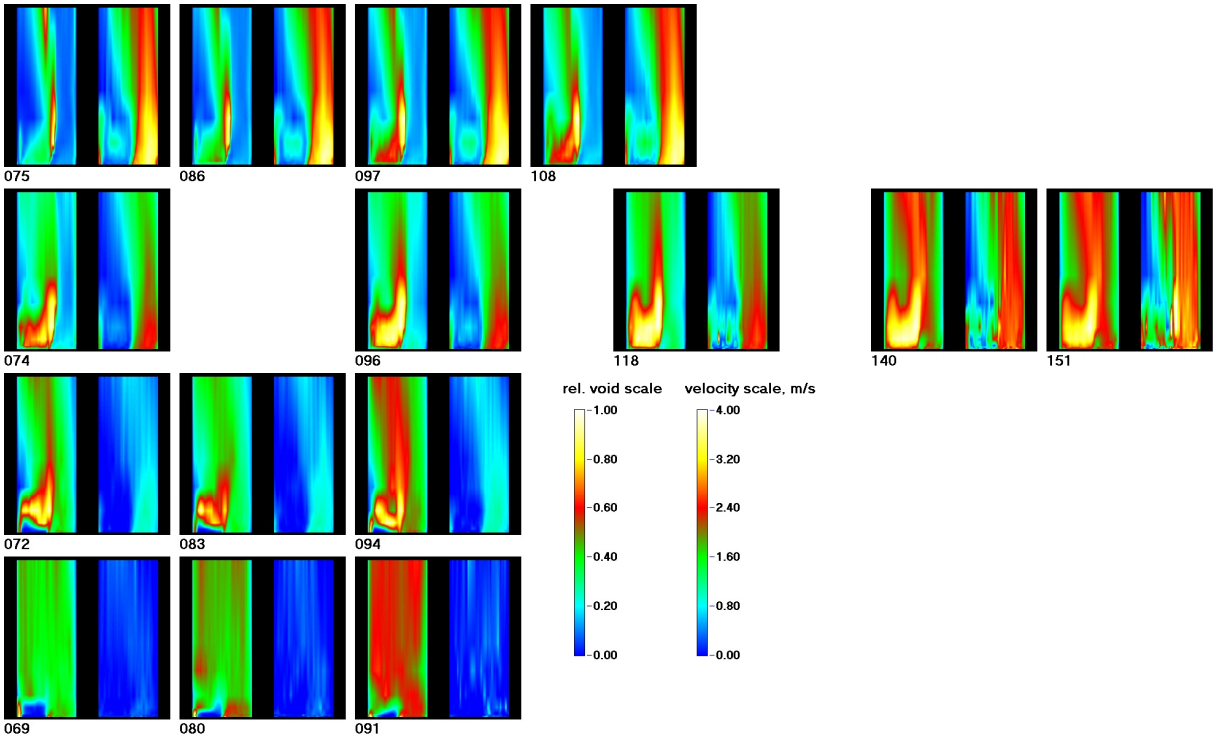

Fig. 8.8 Overview of the time averaged void fraction (left) and liquid velocity (right) distributions along a vertical plane perpendicular to the linear edge of the half-moon shaped plate in the region downstream of the obstacle for all air-water experiments according to the test matrix at Tab. 5.1

Another tendency is found in the void fraction close to the stagnation point. In the test 096 (J_L = 1.0 m/s) there is still a decrease of the void fraction found in front of the obstacle, similar to case 097 at J_L = 1.6 m/s, but the lower velocity in test 094

(J_L = 0.4 m/s) is no more sufficient to expel the bubbles from the stagnation point region. In test 091 at J_L = 0.1 m/s, there is even an increase of void fraction in front of the obstacle that is caused by the pile-up of rising bubbles.

Downstream of the obstacle, the decrease of the liquid velocity leads to a shrinking of the recirculation area, which is completely missing at J_L = 0.1 m/s (test 091). A depletion of the gas phase from a region closely above the obstacle is observed, instead, in the tests 094 and 091.

Experiments carried out at different gas injection rates mostly behave similar to the discussed cases with J_G = 0.09 m/s, independently from whether the superficial air velocity is higher or lower (see overviews in Fig. 8.8 and Fig. 8.9). Differences were observed concerning the wall peak in the air-water experiments of the gas fraction profile in the undisturbed region upstream of the obstacle, which is vanishing at higher superficial gas velocities, when the horizontal line of J_L = 1 m/s in the test matrix (Tab. 5.1) is followed towards high gas flow rates (see attachment B). The highest superficial gas velocity, where a wall peak was found, was reached in test point 096 at J_G = 0.09 m/s. Starting from J_G = 0.22 m/s (point 118) the profiles are completely changed to a central peaked one.

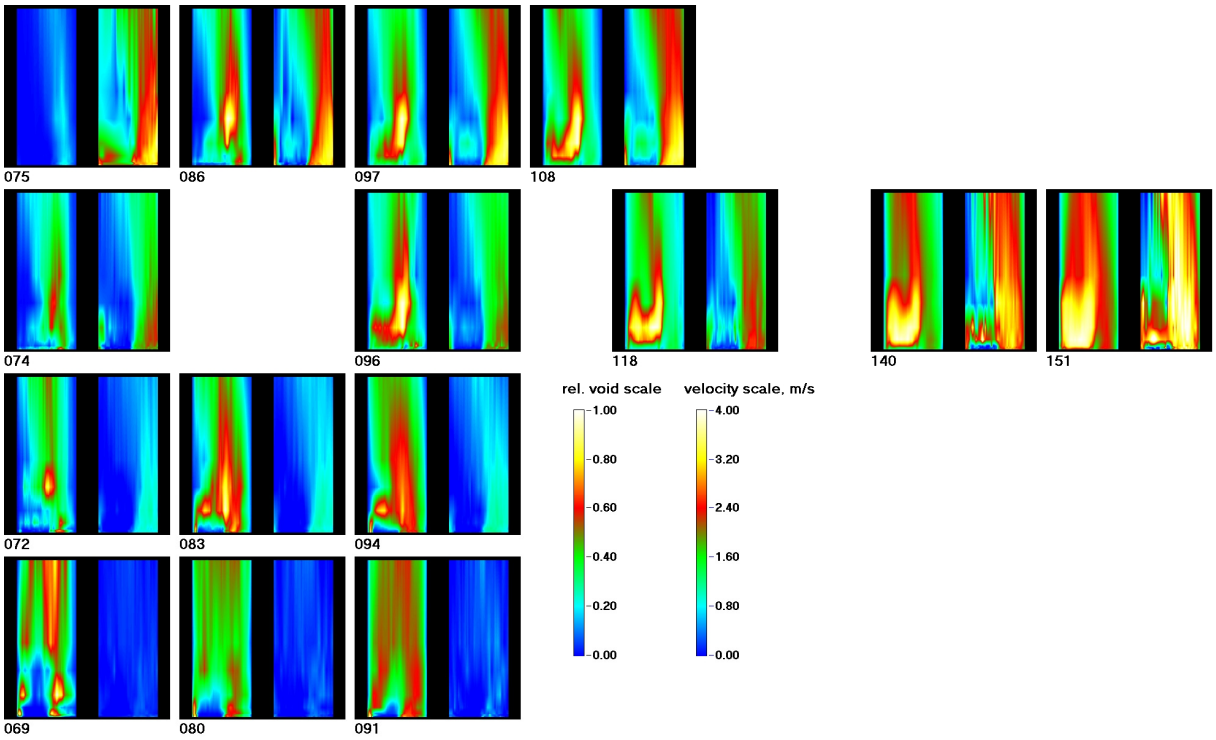

Fig. 8.9 Overview of the time averaged void fraction (left) and liquid velocity (right) distributions along a vertical plane perpendicular to the linear edge of the half-moon shaped plate in the region downstream of the obstacle for all steam-water tests at 6.5 MPa according to the test matrix at Tab. 5.1

8.3 Lateral bubble velocities

Plots of the lateral velocity components in x and y directions show the deviation of the flow around the obstacle (Fig. 8.10 and Fig. 8.11). The vectors in these figures represent the average velocity of the instantaneous cross-sections of all bubbles in the time interval when they pass the measuring plane. The data of the air-water test point 097 is presented. For a better visualization the colour of the vectors indicates

the absolute value of the lateral velocities and corresponds to the length of it. Blue means minimal – and yellow maximal velocities respectively.

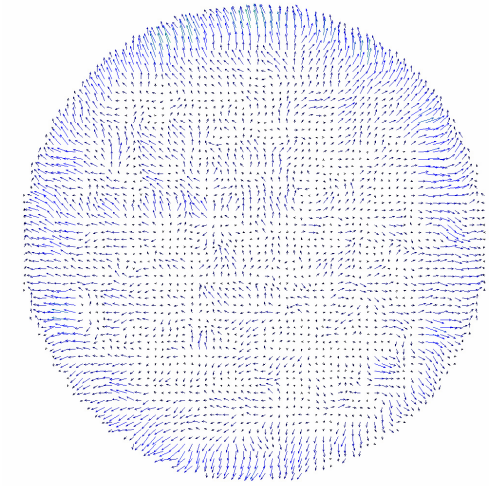

z = -520 mm

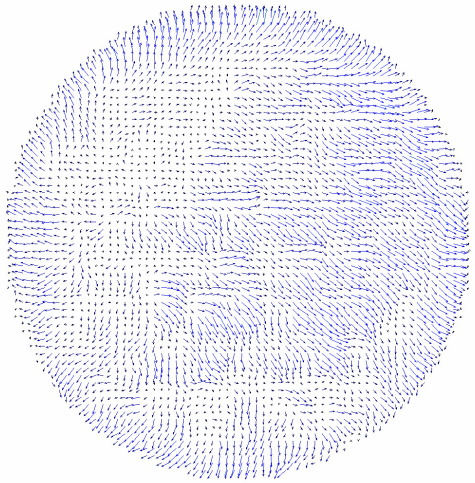

z = -160 mm

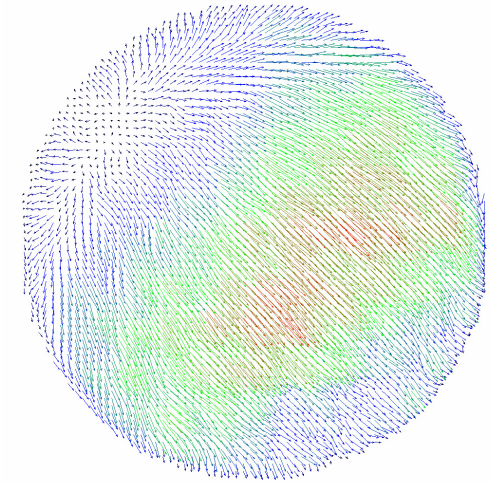

z = -80 mm

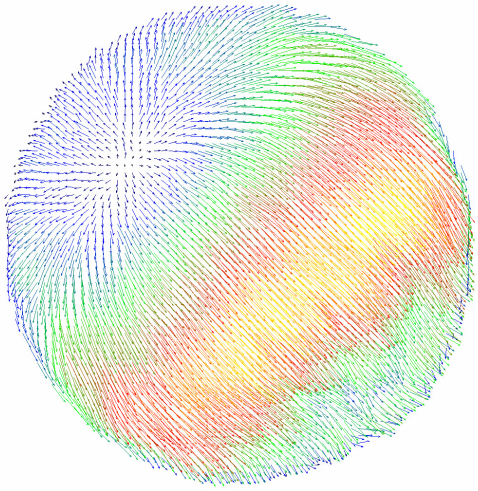

z = -40 mm

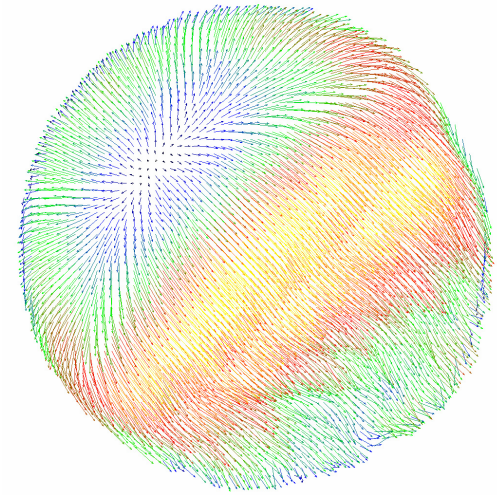

z = -20 mm

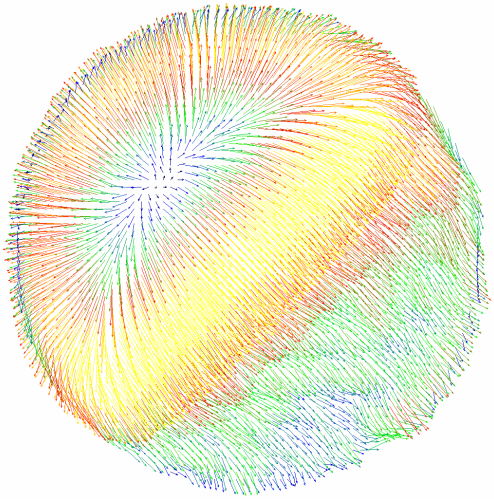

z = -10 mm

Fig. 8.10 Vector plots of the lateral velocity components upstream of the obstacle in the air-water test 097 at J_L = 1.611 m/s and J_G = 0.0898 m/s

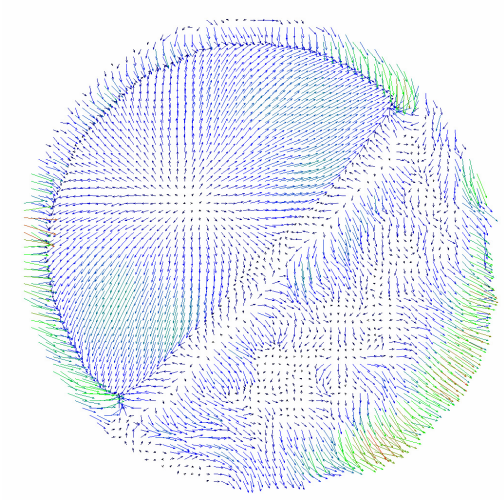

z = 10 mm

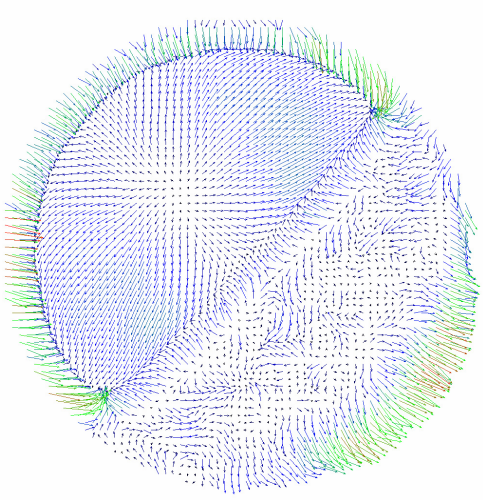

z = 20 mm

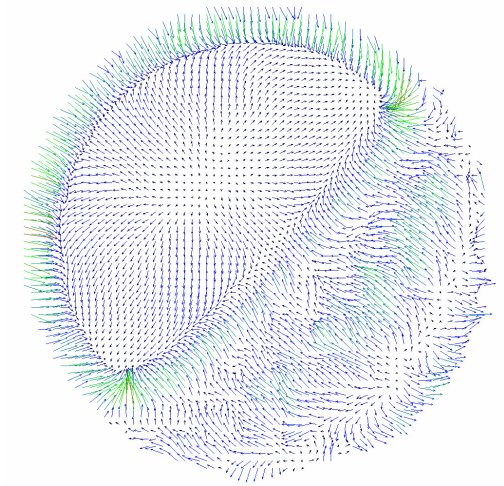

z = 40 mm

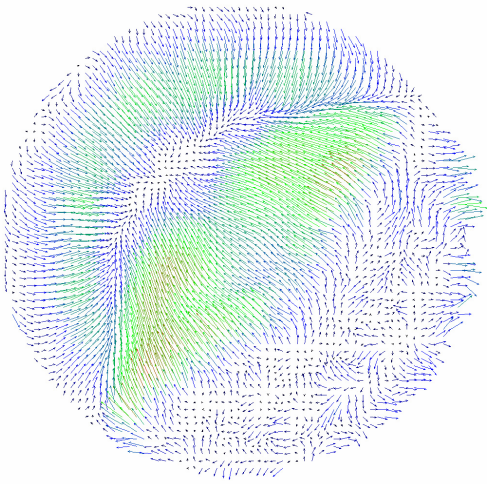

z = 160 mm

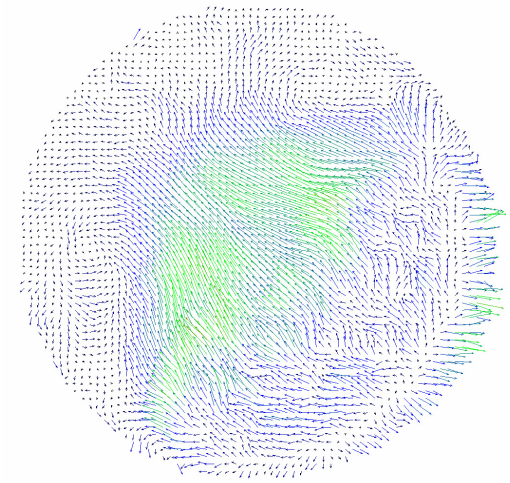

z = 250 mm

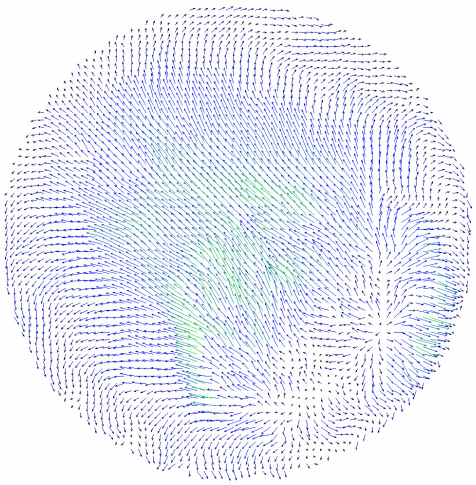

z = 520 mm

Fig. 8.11 Vector plots of the lateral velocity components downstream of the obstacle in the air-water test 097 at J_L = 1.611 m/s and J_G = 0.0898 m/s

At maximal distance upstream of the diaphragm (Fig. 8.10, z = -520 mm), the vector field is dominate by a statistical scattering of the velocities except at the periphery of the pipe cross-section, where an unphysical tendency to deliver velocity vectors that point in a radial outwards direction is found. Since the influence of the diaphragm starts to be recognizable only at about z = -160 mm, it can be assumed that there is a parallel flow at the maximal distance. The outwards pointing vectors are therefore to be considered the result of a systematic measuring error (discussion in section 10.3).

At z = -160 mm upstream of the obstacle, a pronounced lateral fluid movement from the obstructed to the unobstructed side of the pipe starts to develop. It becomes more and more intensive the more the diaphragm is approached. Soon the diverging flow pattern caused by the stagnation point starts to become visible on the obstructed side. At the closest distance of z = -10 mm, the contour of the half-moon shaped plate is clearly reflected in the vector plot.

The latter is found even in a more pronounced way in the vector fields closely downstream of the obstacle (Fig. 8.11). On the unobstructed side, the vectors continue to point away from the obstacle still until z = +40 mm, where for the first time the vectors inverse. This corresponds to the shape of the jet found on the unobstructed side, which is bended towards the free side of the cross-section closely after the flow separation and later towards the obstructed side (see Fig. 8.1).

Straight above the half-moon shaped plate, a similar flow pattern is found as below. Here, again diverging vector field is found that corresponds to a stagnation point, which this time is formed on the downstream side of the obstacle. This is a clear indication for a downwards flow in the wake of the half-moon plate and confirms the hypothesis of a recirculation in this region. At z = +160 mm, the vector field turns to a converging one, because this is the upper

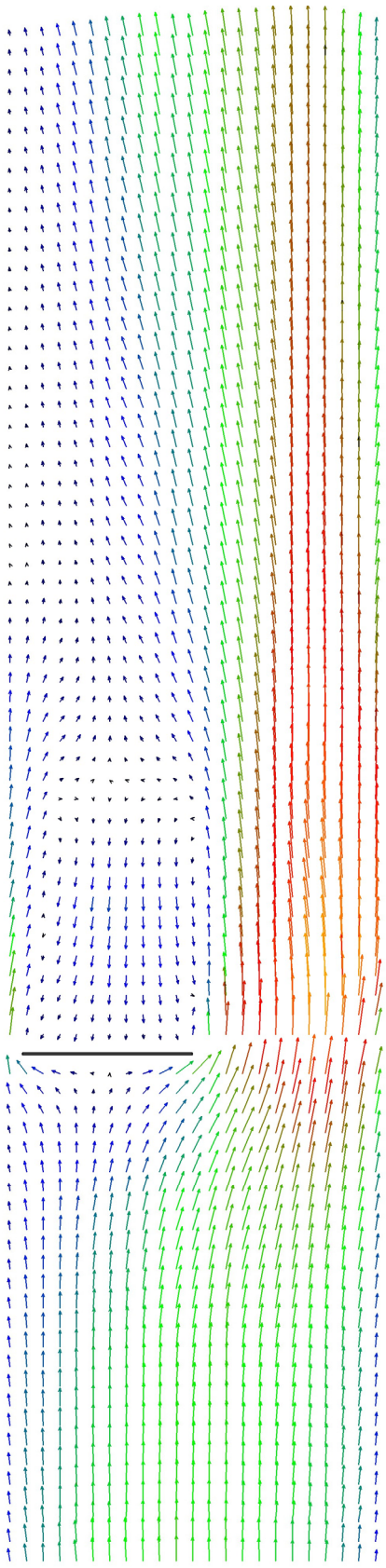

Fig. 8.12 Vector plots combining the lateral and axial velocity components, test run 097

end of the recirculation region. At the two last measuring positions (z = +250 and +520 mm) there is a dominating flow from the unobstructed towards the obstructed side of the pipe cross-section that is necessary to re-establish an equilibrium velocity profile, which was not reached again within the available range of the obstacle translation in none of the tests.

Using the assumption that the lateral movement of the bubbles relative to the liquid can be neglected due to the domination of the bubble rise, a vector field of the liquid velocity in the vertical mid-plane of the pipe perpendicular to the linear edge of the half-moon shaped obstacle can be constructed by combining the lateral and the axial velocities. The result for the air-water test run 097 is shown in Fig. 8.12. In this figure, the axial velocity components in the recirculation region were inverted manually. This operation was limited to a region that is surrounded by a belt where the velocity is found to be close to zero. The spatial resolution of the vector plot was reduced compared to the resolution of the mesh sensor by factor of two in order to keep the picture transparent. The overall structure of this field is typical for all test runs with superficial liquid velocities of 1 and 1.6 m/s. For smaller superficial liquid velocities, the vector plots are much more affected by noise, which makes the interpretation difficult.

9. Comparison between the CFX Pre-Test Calculation and the experimental data

In preparation for the direct comparison of the CFD results with the experiments the 3D dataset from the wire-mesh sensor has been imported into the CFX graphical postprocessor in order to allow for the application of identical data processing, colour schemes and therefore a more direct comparison of the CFD results and experimental data. Since experimental data have a fine (64×64) planar resolution in the x-y-plane but a limited coarser resolution in z-direction with respect to measuring planes, a pre-interpolation of the experimental data in z-direction has been applied with an axial resolution of the interpolated data with $\Delta z = 1$ mm.

As aforementioned in chapter 6, in preparation for the experiments were carried out 2 steady-state ANSYS CFX calculations on different grids. Already the calculation on the coarse grid has qualitative reproduced the structure of the two-phase flow field around the diaphragm for test conditions of TOPFLOW-074. This concerns shape and extension of the recirculation area, the stagnation zone upstream of the diaphragm as well as the velocity maximum in the non-obstructed part of the cross-section and the void fraction maximum in the recirculation area. Smaller details, like the velocity maximum above the gap between the circular edge of the obstacle and the inner wall of the pipe are also found in a good agreement between experiment and this calculation.

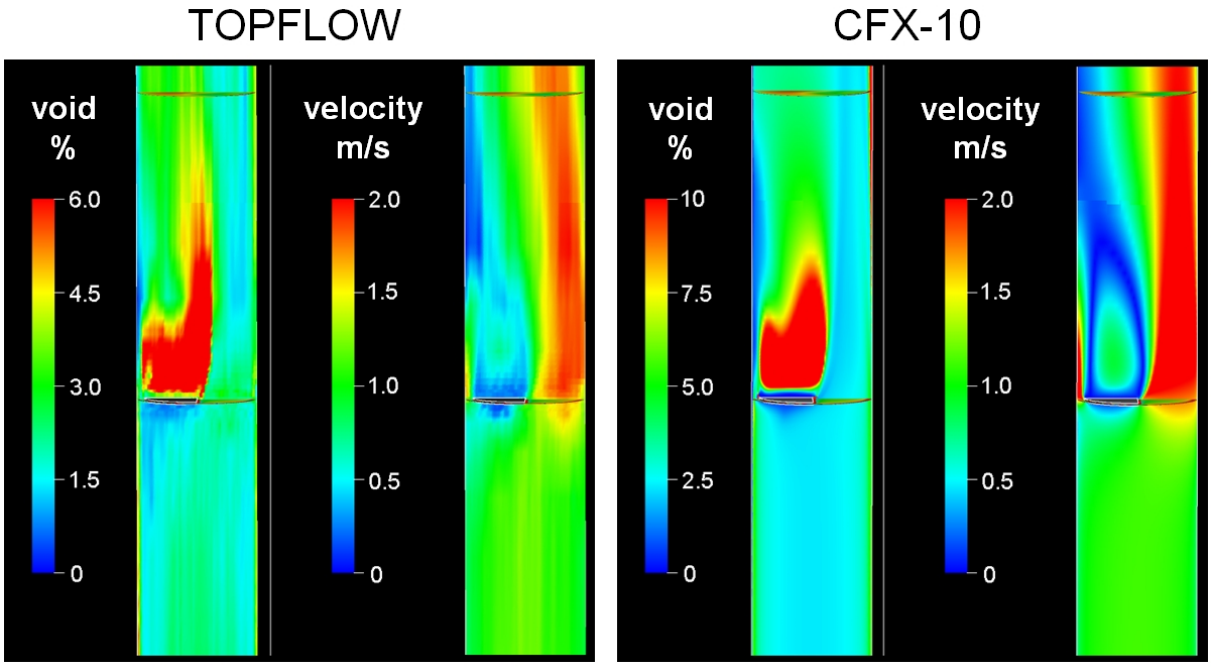

Fig. 9.1 Confrontation of experiment and CFX pre-test calculation by comparison of time averaged void fraction and liquid velocity distributions up- and downstream of the obstacle in the air-water test run 074, J_L = 1.017 m/s, J_G = 0.0368 m/s

A comparison of the pre-test calculation on the finer grid with measurement data are shown in Fig. 9.1 for absolute water velocity and gas volume fraction distributions. The velocity field behind the obstacle shows the same location and intensity of the recirculation zone and stagnation regions on the obstacle surface. The reattachment length of the flow to the pipe wall downstream the obstacle is slightly increased in the CFD simulation, which is probably linked to the higher amount of entrained gas void fraction in the vortex behind the obstacle. Furthermore the present simulation tends to over-predict the void fractions in the wake. This is a result of the assumption of a mono-disperse bubbly flow with a bubble size differing from reality and neglecting bubble coalescence with formation of larger bubbles in the wake of the obstacle. The agreement can be improved by using measured bubble-size distributions from the region upstream of the obstacle as a boundary condition for post-test calculations or by application of the inhomogeneous MUSIG model for the prediction of bubble size distributions from local flow conditions.

10. Uncertainty analyses of the velocity assessments

10.1 General remarks

The methods presented to obtain profiles of the axial as well as lateral components of the liquid respectively the bubble velocities reveal valuable insight into the structure of the flow surrounding the obstacle, although it is clear that high accuracy cannot be expected. Firstly, in case of the profiles of the axial liquid velocity, the method has to rely on an assumption about the constancy of the shape of marker bubbles in terms of the relation between their lateral and axial extension. This ratio nevertheless may vary in dependence on many parameters within the profile present in the measuring cross-section, while the calibration is done on basis of an integral

superficial velocity. Additionally, a velocity dependent effect of the sensor itself causing a deformation of the marker bubbles can contribute to the error.

Secondly, the flow in the vicinity of the obstacle experiences strong accelerations. In the resulting pressure field, the bubble rise velocity can no more be considered to remain a constant value, like it was done in eq. 10. Additionally, non-zero lateral components of the relative bubble velocity have to be expected in these regions. Both effects requires special attention, since it has to be demonstrated, that it dues not qualitatively distort the determined velocity distributions and vector fields.

In case of the lateral bubble velocity, the measurement is much more direct, although a considerable disturbance of the wire grids has to be expected. Bubbles that perform a lateral movement within the measuring plane are supposedly much more obstructed by the electrode wires, than bubbles penetrating the plane in axial direction, since the first come in contact with more electrode wires.

10.2 Liquid velocity estimation by marker bubble method

10.2.1 Reconstruction of the superficial liquid velocity

The quality of the reconstruction of the superficial liquid velocity on basis of the calibration coefficient C that is obtained by averaging the result of eq. (13) over all undisturbed measuring positions upstream of the obstacle, allows conclusions about the accuracy of the achieved measurement of the axial liquid velocity. In the optimal case, the superficial liquid velocity obtained from eq. (11) using the liquid velocity distribution according to eq. (10) is equal to the value corresponding to the set liquid flow rate in the given test, except in those measuring planes, which were affected by a recirculation. As discussed before, at those positions, the reconstructed superficial velocity must be bigger than the one corresponding to the water supply rate.

Typical axial runs of the reconstructed superficial liquid velocity curves are shown in Fig. 8.3 for the air-water test points 091, 094, 096 and 097, i.e. at a constant superficial gas velocity of $J_G = 0.0898$ m/s. They reveal that, in reality, the reconstructed superficial liquid velocity is not perfectly constant. Closely upstream of the obstacle, the inhomogeneous pressure field generates systematic measuring errors that affect the integral superficial velocity. In the recirculation region behind the obstacle, the reconstructed values are by about 20 % higher than the superficial velocity corresponding to the water volume flow. Test point 091 is an exception from this observation, since a recirculation is not found at the lowest liquid flow rate (compare Fig. 8.8).

Further downstream, the reconstructed superficial liquid velocity falls back even below the value arising for the water supply. It can be concluded that at this point the recirculation region has ended and the further decrease is caused by other error contributions. The superficial velocity at the most distant position (z = +520 mm) is more than 20 % below the set value at $J_L = 1.611$ m/s. The error decreases towards smaller liquid velocity and practically vanishes at $J_L = 0.405$ m/s. The nature of the errors generating these deviations is not known. It must be assumed that additional effects of bubble deformation in the vicinity of the strong liquid jet downstream of the obstacle may be the reason. The found underestimation of the superficial liquid velocity characterises the general magnitude of these effects.

10.2.2 Comparison with cross-correlation

A direct measurement of an average bubble velocity by cross-correlation between a pair of sensors put into the flow in a short distance between each can be used to check the correctness of the proposed marker bubble method. Experimental data from the large vertical test suitable for such a comparison were obtained in earlier air-water test series without the obstacle, for which two identical mesh sensors were available. The vertical test section was equipped with the same gas injector used in the experiments with the half-moon shaped obstacle.

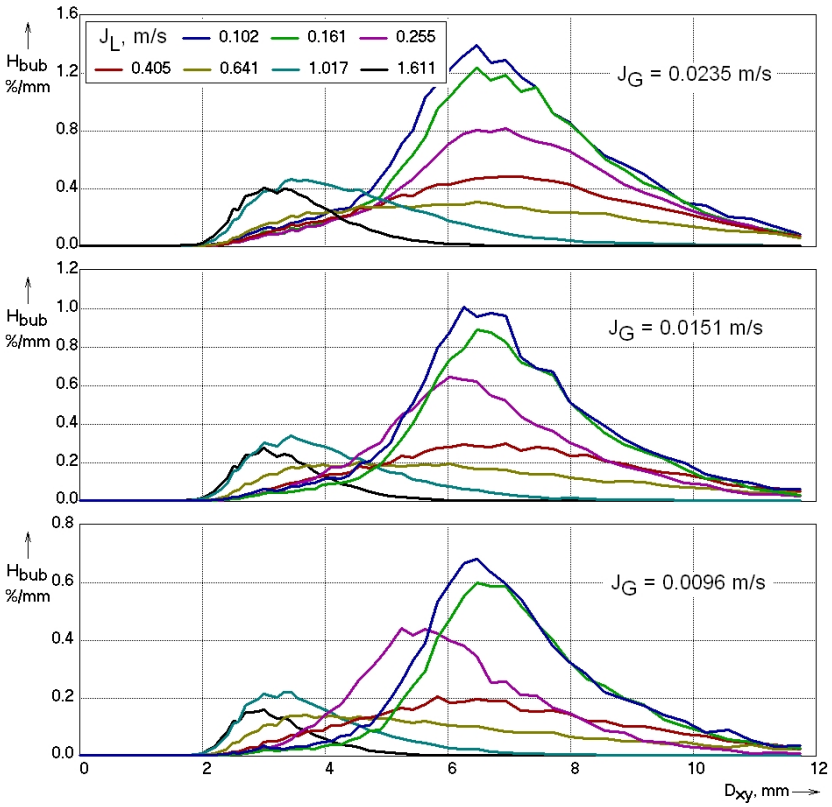

Fig. 10.1 Bubble size distributions in the air-water tests performed at the test section DN200 without obstacle and with a pair of wire-mesh sensors

The direct gas velocity measurement is performed by a point-to-point cross-correlation analysis between the signals of the first and the second wire-mesh sensor. The flow in the test section was not disturbed by non-axisymmetric inserts. It can therefore be assumed that all measured averaged quantities are only functions of the radius. Cross-correlation functions were averaged over ring-shaped domains to obtain radial gas velocity profiles (Prasser et al., 2005a).

Until now, it was not possible to cross-correlate the wire-mesh sensor signals for the experiments in a bubble-size selective way, since the cross-correlation coefficients are too small to obtain stable maxima in cases with liquid velocities below 1 m/s. For this method, the applied distance of 65 mm between the sensors is too large. In order to get close to a characterization of the velocity of marker bubbles with a diameter D_{xy} between 4 and 5 mm, experimental points with low superficial air velocity were selected, where the bubble-size distributions are as close as possible to the size of the selected marker bubbles. The points chosen from the test matrix were recorded at a superficial gas velocity of J_G = 0.0096, 0.0151 and 0.0235 m/s and at various superficial liquid velocities between J_L = 0.102 and 1.611 m/s (test points 036 - 042, 047 - 053 and 058 - 064). Parallel to the cross-correlation analysis, the data was treated by the marker bubble method. The bubble size distributions for these test runs are shown in Fig. 10.1. At low superficial liquid velocities, there is a most probable bubble diameter of about 6 - 7 mm, which decreases down to about 3 mm when the superficial velocity is increased to 1 - 1.6 m/s. In all cases, enough void is in the diameter range chosen for the marker bubbles.

In Fig. 10.2, radial averaged uncorrected marker bubble velocities $\overline{v}_{MB}$ are compared to the gas velocities obtained by the cross-correlation $v_{G,corr}$. The variation of the velocities within each test regime is the result of the radial velocity profile. The fact that the individual data points are arranged in a nearly linear manner confirm the applicability of the marker bubble method. Some points escaping from the main trend are due to errors of the cross correlation. The slope is close to 1 which nearly agrees to the calibration coefficients found in the analysis of the data from the obstacle experiments, which were in the range between 0.7 and 1.3.

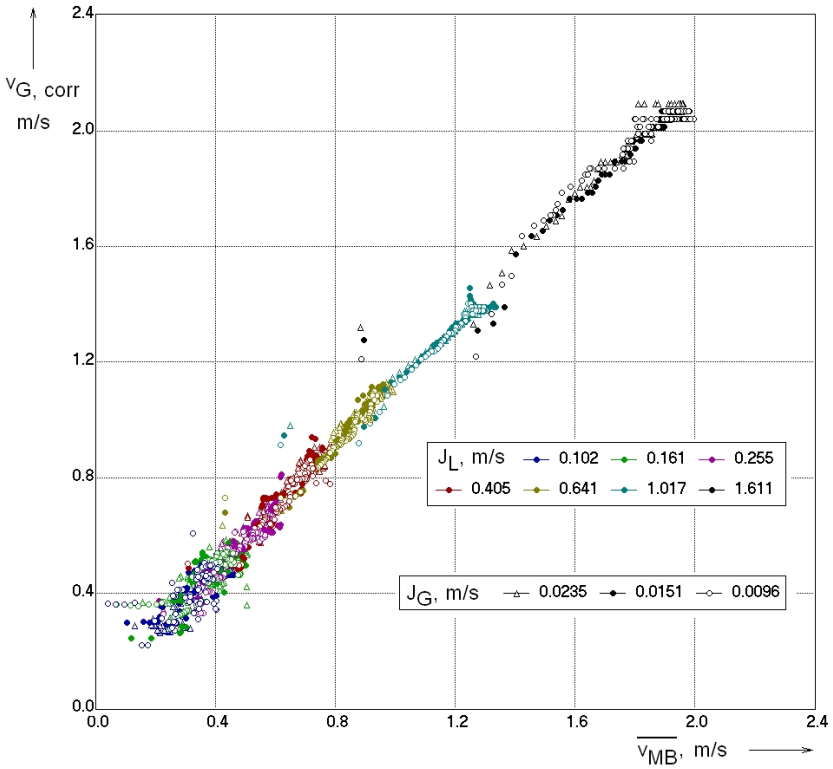

Fig. 10.2 Comparison between the non-calibrated marker bubble velocities and gas phase velocities obtained by cross-correlation between a pair of wire-mesh sensors from radial profiles obtained during air-water tests at the vertical test section DN200 without obstacle

10.2.3 Assessment of the influence of acceleration and deceleration

A second important issue is the assessment of the systematic measuring error that is introduced into the velocity distributions by the action of the strong acceleration or, respectively deceleration of the flow in the surroundings of the obstacle as well as a certain influence of strong velocity gradients. The marker bubble method described in section 7.3 is based on the assumption that the local axial component of the liquid velocity can be deduced from the marker bubble velocity minus the bubble rise velocity relative to stagnant liquid calculated for the chosen marker bubble size. If the flow experiences a strong acceleration, the real bubble velocity relative to the water phase may significantly deviate from this value. If, for example, the flow is accelerated, like on the non-obstructed side of the pipe, the additional pressure gradient amplifies the hydrostatic pressure gradient and an increase of the relative bubble rise velocity is observed. On the other side, the increase of the bubble rise velocity cannot take place instantaneously because of the counteraction of the inertia of the bubble, which is enhanced by the added mass force.

A direct analysis of the uncertainties arising from the mentioned effects is very complicated, since the accelerations would have to be calculated by differentiating velocity distributions that are affected by the systematic errors themselves. Accelerations are therefore available only in an implicit way. Furthermore, the differentiation amplifies statistic fluctuations of the velocities.

It was therefore decided to assess the influence of the acceleration on basis of the modelling results obtained by CFX-10. The calculation took into account all relevant bubble forces except the added mass force. Since the latter leads to a longer conservation of the undisturbed bubble velocity in an accelerating or decelerating velocity field, it was assumed that the results obtained when the added mass force is omitted are conservative, i.e. neglecting the added mass force leads to systematic deteriorations of the measured liquid velocity field larger than in reality.

Calculation results are available only for the test point 074 with J_L = 1.017 m/s. It can be assumed that the magnitude of the errors defined for the conditions of this test point are conservative for all test points with a lower superficial liquid velocity, where the acceleration effects are less pronounced. In case of those points at J_L = 1.611 m/s higher errors have to be expected.

The easiest way to assess the applicability of eq. 10, i.e. check if the assumption of a constant relative marker bubble velocity is acceptable, is a comparison between the liquid velocity distribution calculated by CFX with a simulated measuring result, obtained from the calculated gas velocity distribution by subtracting the constant bubble rise velocity of 0.235 m/s. A focusing on the range of marker bubble diameters (4 - 5 mm) is not necessary, since the CFX calculation was performed with mono-disperse bubbles of 5 mm diameter.

The result is shown in Fig. 10.3, where the calculated liquid velocity distribution (left) is compared to the simulated measurement using the constant bubble rise velocity (right). It is clearly visible, that the acceleration effects do not deteriorate the distribution in a qualitative way. Examples for quantitative deviations are the slight overestimation of the size of the deceleration region in front of the stagnation point and the small local velocity minimum close to the centre of the recirculation area at z = 10 mm. More quantitative details are visible in Fig. 10.4 - Fig. 10.5, where the deviation caused by the acceleration is plotted directly. In the lateral profiles of the axial velocity in Fig. 10.5, the curves represent the simulated measuring results, while the error bars point at the real calculated axial liquid velocities. In all figures, absolute values are shown, i.e. the recirculation area is characterized by a local maximum.

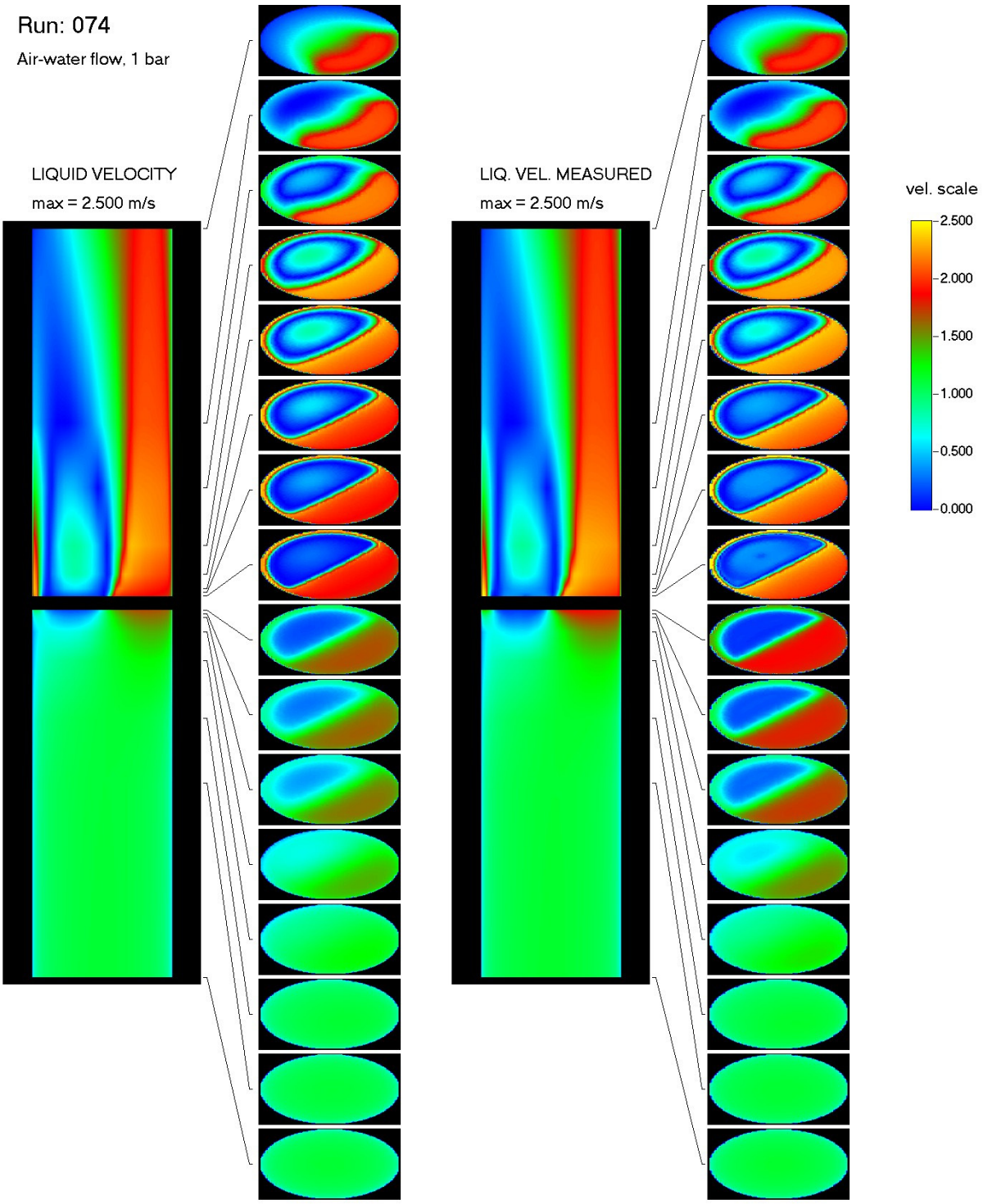

Fig. 10.3 Effect of the acceleration and deceleration of the fluid in the vicinity of the obstacle, assessed by comparing the liquid velocity distribution with the simulated measuring result by subtracting a constant bubble rise velocity from the gas velocity for the results of the CFX pre-test calculations, test 074, J_L = 1.017 m/s, J_G = 0.0368 m/s

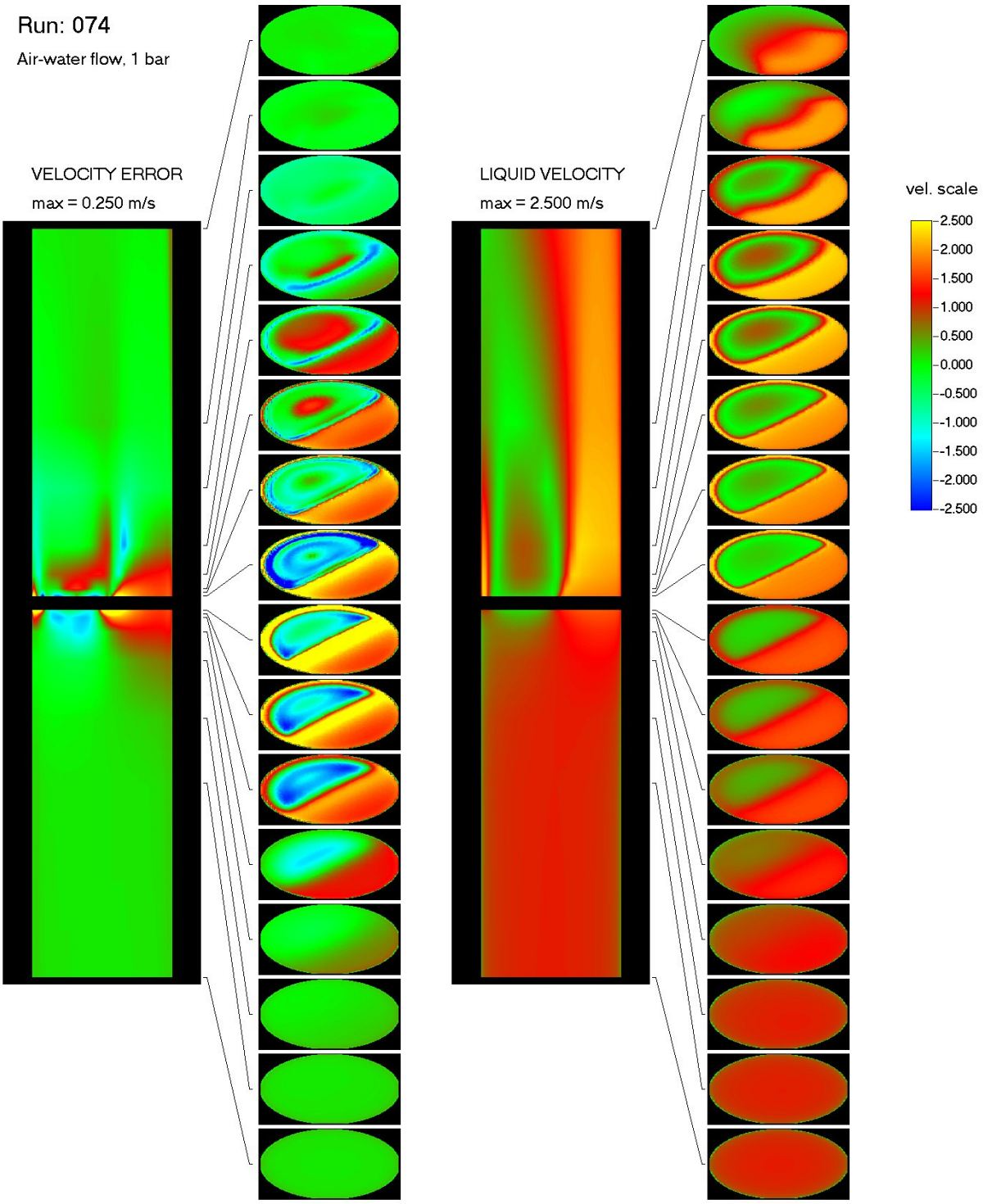

Fig. 10.4 Velocity measuring error due to acceleration and deceleration of the fluid in the vicinity of the obstacle, assessed on basis of the results of the CFX pre-test calculations, test 074, J_L = 1.017 m/s, J_G = 0.0368 m/s

It is concluded that the marker bubble method can lead to systematic errors caused by acceleration, which are in the range of 10 - 20 % of the amplitude of the velocity profiles. Locally, the error can of course be bigger. The error rapidly decreases with growing distance from the obstacle.

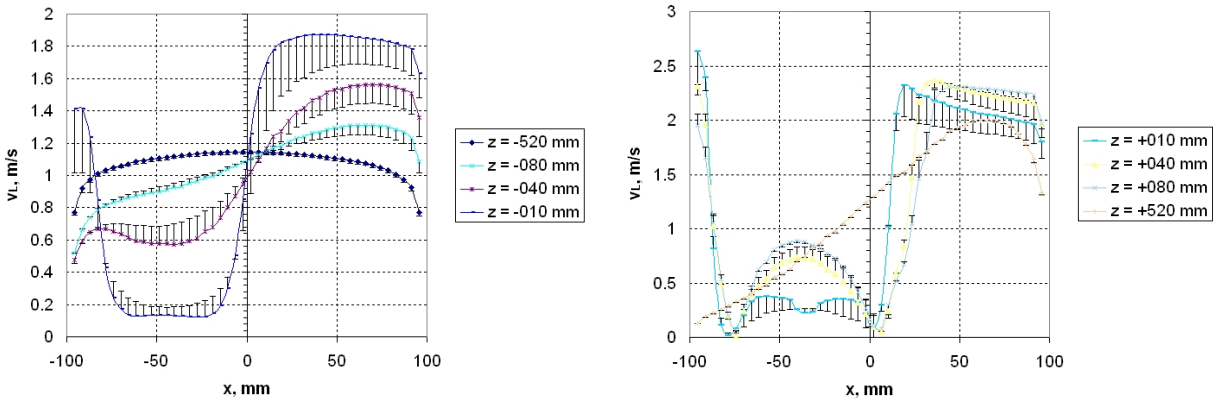

Fig. 10.5 Lateral profiles of the simulated measured axial liquid velocity at selected axial positions up- (left) and downstream (right) of the obstacle and bars for the systematic error caused by acceleration / deceleration, assessed on basis of the CFX pre-test calculation, test run 074, J_L = 1.017 m/s, J_G = 0.0368 m/s

10.3 Lateral bubble velocities

For the time being, there is only a way to asses the influence of the bubble deformation in the shear field close to the wall on the result of the lateral velocity estimation. At the position z = -520 mm upstream of the obstacle, the flow can be envisaged as axisymmetric. The lateral components of the bubble velocity are therefore equal to zero. Elliptically deformed bubbles that have a preferable inclination of their semi-minor axis towards the pipe wall cause an apparent lateral velocity component that is directed towards the wall, too. This is due to the fact that the centre of mass of the part of the measuring cross-section that is occupied by the bubble moves towards the wall, when the bubble passes through the sensor plane, even if the bubble itself

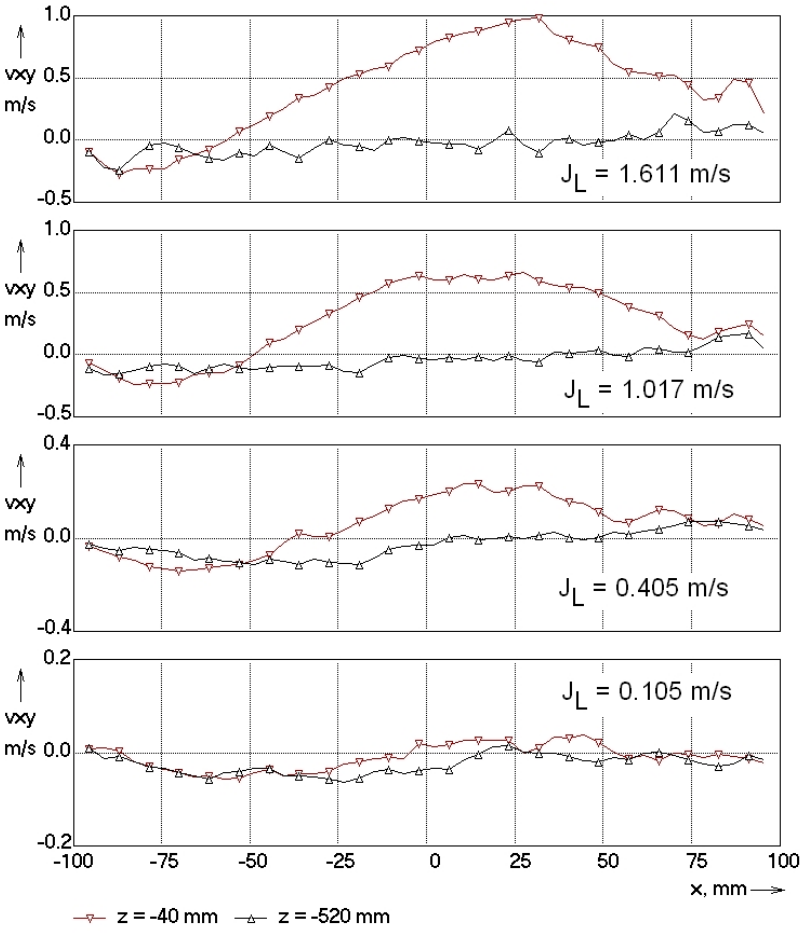

Fig. 10.6 Distribution of the lateral velocity along a diameter of the pipe oriented perpendicularly to the linear edge of the half-moon shaped obstacle for two different upstream distances, liquid velocity varied, J_G = 0.0898 m/s

moves in a vertical direction parallel to the z-axis. The resulting velocities are in the order of 0.1 - 0.2 m/s, as shown in Fig. 10.6.

The same figure contains profiles of the lateral velocity component perpendicular to the linear edge of the obstacle for z = -40 mm, where a strong lateral movement of the fluid from the obstructed towards the non-obstructed side is present. These real lateral velocities are significantly higher than the error caused by the systematic bubble deformation effect.

11. Conclusions

A novel technique to study the two-phase flow field around an asymmetric diaphragm in a vertical pipe is presented, that allows producing data for CFD code validation in complex geometries. Main feature is a translocation of the diaphragm to scan the 3D void field with a stationary wire-mesh sensor. Besides the measurement of time-averaged void fraction fields, a novel data evaluation method was developed to extract estimated liquid velocity profiles from the wire-mesh sensor data. The flow around an obstacle of the chosen geometry has many topological similarities with complex flow situations in bends, T-junctions, valves, safety valves and other components of power plant equipment and flow phenomena like curved stream lines, which form significant angles with the gravity vector, flow separation at sharp edges and recirculation zones in their wake are present. It is the goal of the ongoing CFD code development to accurately model such phenomena in a two-phase flow. Therefore, the experiments provide a good basis for the test and the validation of the codes and their underlying multiphase flow and turbulence models. Due to the generalizing capability of CFD codes, that can adapt to different geometric boundary conditions by the mesh generation, a successful validation on the kind of obtained experimental data guarantees the applicability of the code to other equally complex flow fields.

A pre-test calculation carried out by ANSYS CFX 10.0 resulted in a good agreement with the experiment in terms of all significant qualitative details of the void fraction and liquid velocity distributions. The structure and the geometry of the entire flow field in general as well as the dimensions of recirculation and stagnation zones in particular were predicted in good agreement with the experiment. The fact that for the time being a simple mono-disperse bubbly flow was assumed, lead to an overestimation of void fractions especially in the wake of the obstacle, while the velocity profiles are matching better. It is planned to continue with post-test calculations in order to achieve a better quantitative agreement by using measured bubble-size distributions from the region upstream of the obstacle as inlet boundary condition and in a further step by applying the inhomogeneous MUSIG model for the prediction of bubble size distribution and bubble coalescence. The experimental data will be used to validate this recently developed and implemented model against detailed bubble size and bubble scale resolved void fraction measurements.

12. References

Ahmed, W.H., Ching, C.Y., Shoukri, M., (2005). Development of void fraction and liquid Turbulence of two phase flow downstream of sudden expansions, 4th International Conference on Transport Phenomena in Multiphase systems, Gdansk Poland.

Anagnostopoulos, J., Mathioulakis, D.S., (2004). A flow study around a time-dependent 3-D asymmetric Constriction. Journal of Fluids and Structures, Volume 19, Issue 1, 49-62.

ANSYS CFX 10.0 Users Manual (2005). ANSYS Inc.

Beyer, M., Carl, H., Schütz, P., Pietruske, H., Lenk, S., (2004). Betriebshandbuch für die Mehrzweck-Thermohydraulikversuchsanlage TOPFLOW. Forschungs-zentrum Dresden-Rossendorf, Wissenschaftlich-Technische Berichte, FZR-405.

Boccardi, G., Bubbico, R., Celata, G.P., Cumo, M., Di Tosto, F., (2004). Geometry Influence on Two-Phase Flow in Safety Valves. 5th International Conference on Multiphase Flow, ICMF'04, Yokohama, Japan, paper #478.

Founti, M., Klipfel, A., (1998). Experimental and computational investigations of nearly dense two-phase sudden expansion flows. Experimental Thermal and Fluid Science, Volume 17, Issues 1-2, 27-36.

Founti, M.A., Kolaitis, D.I., Katsourinis, D.I., (2001). Particle induced erosion wear in a sudden expansion flow and in a long pipe transporting crude oil. ASME Fluids Engineering Division Summer Meeting, New Orleans, Louisiana, USA.

Frank, Th., Shi, J., Burns, A.D., (2004). Validation of Eulerian multiphase flow models for nuclear reactor safety applications. 3rd TPFMI, Pisa, Italy, 1-8.

Frank, Th., (2006). Abschlussbericht zum Forschungsvorhaben 150 1271; Entwicklung von CFD-Software zur Simulation mehrdimensionaler Strömungen im Reaktorkühlsystem. ANSYS Germany, Technical Report TR-06-01, 1-72.

Kondo, K., Yoshida, K., Okawa, T., Kataoka, I., (2002). Flow patterns of gas-liquid two-phase flow in round tube with sudden expansion. 10th International Conference on Nuclear Engineering, ICONE10, Arlington, VA, USA.

Kondo, K., Yoshida, K., Okawa, T., Kataoka, I., (2004). Prediction of void fraction distribution for turbulent bubble flow in a vertical pipe with sudden expansion. 3rd International Symposium on Two-Phase Flow Modelling and Experimentation, Pisa.

Kondo, K., Yoshida, K., Okawa, T., Kataoka, I., (2005). A study on bubble motion in turbulent flow field for predicting multi-dimensional void fraction distribution in sudden expansion channel, 13th International Conference on Nuclear Engineering Beijing, China, ICONE13-50644.

Manera, A., Prasser, H.-M., Van der Hagen, T. H. J. J., Mudde, R. F., de Kruijf, J. M., (2001). A comparison of void-fraction measurements during flashing-induced in-stabilities obtained with a wire-mesh sensor and a gamma-transmission set-up. 4th International Conference on Multiphase Flow, New Orleans, Louisiana, USA, paper #436.

Morel, C., Pouvreau, J., Laviéville, J., Boucker, M., (2004). Numerical simulation of a bubbly flow in a sudden expansion with the NEPTUNE Code. 3rd International Symposium on Two-Phase Flow Modelling and Experimentation, Pisa.

Nishimura, M., Itoh, G., Furukawa, S., Takeshima, K., (2000). Development of Large capacity Main Steam Isolation Valves and Safety Relief Valves for next Generation BWR Plant.

Ota, T., Takeuchi, E., Yoshikawa, H., (2001). LES of three-dimensional turbulent separated reattached flow around a surface-mounted square plate. ASME Fluids Engineering Division Summer Meeting, New Orleans, Louisiana, USA.

Pietruske, H., Prasser, H.-M., (2005). Wire-mesh sensors for high-resolving two-phase flow studies at high pressures and temperatures. NURETH-11, Avignon, France, paper #533.

Prasser, H.-M., (2000). High-speed measurement of the void fraction distribution in ducts by wire-mesh sensors. International Meeting on Reactor Noise, Athens, Greece.

Prasser, H.-M., Scholz, D., Zippe, C., (2001). Bubble size measurement using wire-mesh sensors. Flow Measurement and Instrumentation, 12/4, 299-312.

Prasser, H.-M., Beyer, M., Böttger, A., Carl, H., Lucas, D., Schaffrath, A., Schütz, P., Weiss, F.-P., Zschau, J., (2004a). TOPFLOW Tests on the Structure of the Gas-Liquid Interface in a Large Vertical Pipe. Jahrestagung Kerntechnik, Düsseldorf, 69-74.

Prasser, H.-M., (2004b). Influence of the Gas Injection on the Void Fraction Profiles and Bubble Size Distributions of an Air-Water Flow in Vertical Pipes. 5th ICMF, Yokohama, Japan, paper #187.

Prasser, H.-M., Krepper, E., (2004c). Air water flow in a vertical pipe with sudden changes off the superficial water velocity. 3rd International Symposium on Two-Phase Flow Modelling and Experimentation, Pisa, Italy.

Prasser, H.-M., Beyer, M., Böttger, A., Carl, H., Lucas, D., Schaffrath, A., Schütz, P., Weiss, F.-P., Zschau, J., (2005a). Influence of the pipe diameter on the structure of the gas-liquid interface in a vertical two-phase pipe flow. Nuclear Technology. 152, 3-22.

Prasser, H.-M., Beyer, M., Carl, H., Pietruske, H., Schütz, P., (2005b). Steam-water experiments at high pressure to study the structure of the gas-liquid interface in a large vertical pipe. Annual Meeting on Nuclear Technology, Nuremberg, paper #215.

Prasser, H.-M., Misawa, M., Tiseanu, I., (2005c). Comparison between Wire-Mesh Sensor and ultra-fast X-ray Tomograph for an Air-Water Flow in a vertical pipe. Flow Measurement and Instrumentation, Vol. 16, 73-83.

Rinne, A., Loth, R., (1996). Development of Local Two-Phase Flow Parameters for Vertical Bubbly Flow in a Pipe with Sudden Expansion. Experimental Thermal and Fluid Science, Volume 13, Issue 2, 152-166.

Schiller, L., Naumann, A., (1933). A drag coefficient correlation, VDI-Zeitschrift, 77, p 318.

Scholz, D., (2000). Bewertung der Genauigkeit eines Gittersensors zur Visualisierung einer Zweiphasenströmung durch Vergleich mit optischen Hochgeschwindigkeitsaufnahmen. Forschungszentrum Dresden-Rossendorf, Wissenschaftlich-Technische Berichte, FZR-300.

Sotiriadis, A.A., Thorpe, R.B., (2005). Liquid re-circulation in turbulent vertical pipe flow behind a cylindrical bluff body and a ventilated cavity attached to a sparger. Chemical Engineering Science, Volume 60, Issue 4, 981-994.

Tomiyama, A. Sou, I. Zun, N. Kanami, T. Sakaguchi, (1995). Effects of Eötvös number and dimensionless liquid volumetric flux on lateral motion of a bubble in a laminar duct flow, Advances in Multiphase Flow, pp. 3-15.

Tomiyama, A., (1998) Struggle with computational bubble dynamics, in: Proceedings of Third International Conference on Multiphase Flow, ICMF 98, Lyon, France, June 8-12.

Wellek, R.M., Agrawal, A.K., Skelland, A.H.P., (1966). Shapes of liquid drops moving in liquid media, AIChE Journal, vol. 12, pp. 854-860.

Acknowledgements

The authors thank the technical team of TOPFLOW, by name Klaus Lindner, Heiko Rußig, Marko Tamme und Steffen Weichelt. Electronic equipment for wire-mesh sensors was developed in co-operation with TELETRONIC GmbH (www.tz-rotech.de/teletronic/).

13. Nomenclature and indexes

13.1 Symbols

Sign	Unit	Denomination
A	m^2	area
a	-	weight factor
b	-	matrix of bubble numbers
C	-	calibration factor
c_x, c_y	mm	constants
D	mm	diameter
D_{equ}	mm	volume-equivalent bubble diameter
D_{xy}	mm	bubble diameter in the horizontal (xy) plane
Δ	-	difference
f	Hz	frequency of measurements
H	%/mm	frequency of occurrence
i, j, k	-	numeric indexes
J	m/s	superficial velocity
L	m	length

n	-	bubble number
p	MPa	pressure
T	°C	temperature
t	s	time
V	m³	volume
v, w	m/s	velocity
x, y	mm	co-ordinates
z	ms or mm	co-ordinates
ε, eps	%	volumetric gas fraction

13.2 Indices and abbreviations

Sign	Denomination
air	air
bub	bubble
CFD	computational fluid dynamics
CFX	CFD software
CM	centre of mass
cr	criterion
DN	nominal diameter
equ	equivalent
FZD	Forschungszentrum Dresden-Rossendorf
G	gas
inj	injection
L	liquid
max	maximal
MB	marker bubble
meas	measurement
MUSIG	Multi Bubble Size Group Model (CFX)
S	saturation

13.3 Figures

13.4 Tables

Attachment A: Description of data files

A.1 Nomenclature of the files

During record of experimental data and data evaluation are created files with the following nomenclature:

NNN_DDD_VVV_lgel_m008_lcc_aaab_x.1x64x64.pkt.typ;

The letters encrypted in the following way:

NNN - identification of the measuring run (L11-air; D14-steam),

DDD - inner diameter of the pipe in mm – to classify the big or the small test section, here the identifier 195 or 200 means 193.7 mm,

VVV - construction of the test section, in this case VTS for vertical test section,

lgel - describes the kind of gas injector, see Fig. 4.5,

m008 - middle injection with orifices of 0.8 mm diameter,

l - stands for t – temperature or p – pressure,

cc - if l is t, then cc shows the middle temperature in °C, otherwise it's the pressure in bar,

aaa - distance between the obstacle and the wire-mesh in mm,

b - + or -, see chapter 5,

x - this position is only important for measurements with 2 sensors,

1x64x64 - one high temperature sensor with 64 to 64 wires was used,

pkt - measuring point, according to Tab 5.1,

typ - file type, see Tab. A1.

Tab: A1: Description of file types for the experiments with the movable obstacle

file type	description	standard
*.a	geometrical properties of the identified bubbles (see section A.2)	text
*.av2	lateral bubble velocity components (see section A.7)	text
*.b	bubble identification number	binary
*.eps_bub	time-averaged void fraction in the form of cross sections decomposed according to bubble size classes (see section A.3)	text
*.epsr	time-averaged void fraction for the 3260 crossing points of the sensor (see section A.4)	text
*.epsrad80	time-averaged void fraction relating to 80 toroidal sections (see section A.4)	text
*.epsxy	time-averaged void fraction in terms of cross section (see section A.4)	text
*.his	bubble size distributions (see section A.5)	text
*.mes	measuring data without any calibration or evaluation	binary
*.uw	calibration matrix	text

Attachment A: Description of data files

*.v	void fraction distribution between 0 – 100 %	binary
*.vel	time-averaged liquid velocity distribution (see section A.6)	text

A.2 Geometrical properties of the bubbles

This file contains a table of geometrical properties sort by bubble numbers with the following entries:

bb - bubble identification number,

im, jm, km - centre of gravity of the bubble in i – flow direction and j, k – cross section plane,

ifront, jfront

kfront - coordinates of the beginning of the bubbles,

iback, jback

kback - coordinates of the end of the bubbles,

mi, mj, mk - momentum of the bubbles in i – flow direction and j, k – cross section plane,

mr - momentum related to the radius,

max - maximum of the void fraction per bubble,

v - volume of the bubble,

r - radius of a volume-equal sphere (see eq. 4),

n - number of elements of a bubble,

deps - part of the void fraction of the current bubble in the total flow volume,

rxymax - maximum radius of the bubble in cross section plane (see eq. 6).

A.3 Void fraction distributions decomposed according to bubble size classes

Based on the theory of data evaluation described in section 7.4 the corresponding results are listed in text files. Depends on the number of bubble classes, setting in the data evaluation software, these files contain tables of time-averaged void fraction values over the cross section plane. Using these tables and special visualisation software, Fig. 8.2 shows lateral and longitudinal views along the diameter of the tube, in this case for 4 bubble classes.

A.4 Void fraction distribution

As aforementioned in Tab. A.1, in general there are three files with void fraction distributions for the total flow. All files contain time-averaged values in various kinds of presentation. The *.epsr files supply information about any of the crossing points with his distance from the centre of the sensor. The *.epsrad80 files show the void fraction distribution averaged not only for the time frames but also over 80 toroidal areas divided the measuring plane. It will be used to generate radial distributions. The *.epsxy files present an overview about the flow. They contain data about all

crossing points of the sensor arranged according to their position in the measuring plane.

Fig. A.1 exemplify a radial void fraction distribution for the measuring point 97 at the farthest height position upstream the obstacle. It shows a typical distribution for a bubbly flow with a wall maximum.

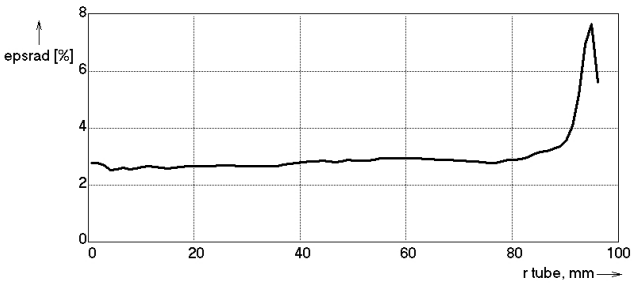

Fig. A.1: Radial void fraction distribution, point 97, J_L = 1.6 m/s, J_G = 0.09 m/s, height: 520-

A.5 Bubble size distributions

These files contain time and cross section averaged bubble size distributions in table form related to the bubble diameter. There are two kinds of distributions: firstly arranged according to a fixed width of the bubble classes equal to 0.25 mm and secondly for a width of bubble classes evaluated in a logarithmic way. The first kind is better for theoretical analyse and the second – for visualisation. The number of rows in these files depends on the maximum bubble size.

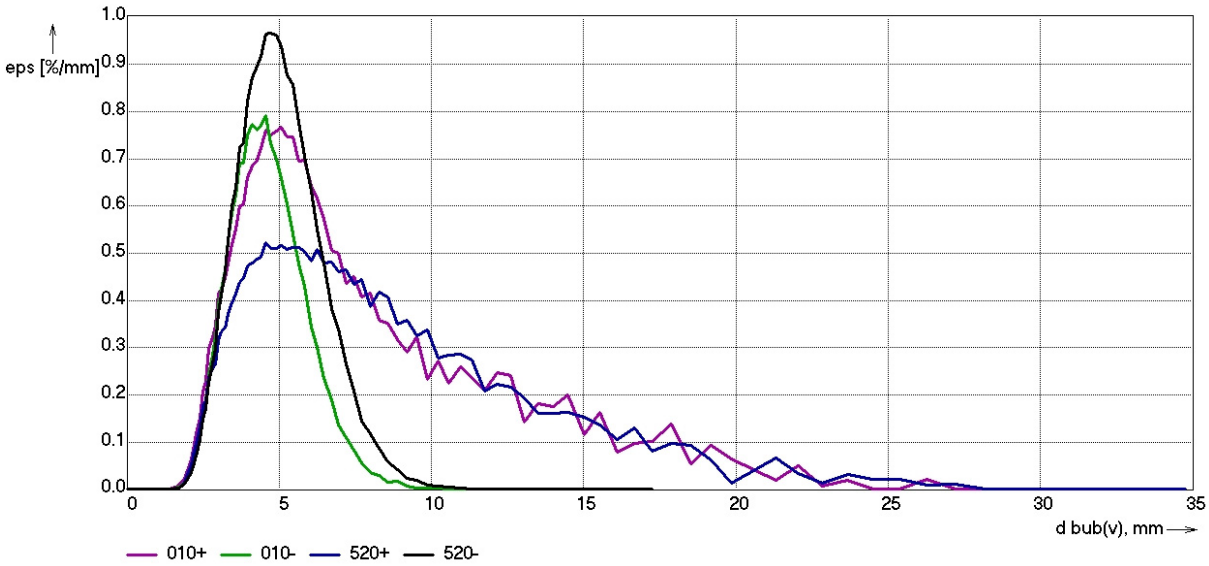

Fig. A.2 Bubble size distributions (J_L=1.6 m/s, J_G=0.09 m/s) for the air-water test 097 at the farthest and nearest distance upstream (-) and downstream (+) of the obstacle related to xy diameters

At the first row the table contains a head which identifies the content of the columns. For these experiments they have the following meanings:

d minimum diameter of the size class and maximum diameter of the previous one [mm],

hdxy volume gas fraction represented by the current bubble class divided to the width of it [%/mm],

hdrelxy normalized bubble size distribution (void fraction related) [1/mm],

hdnxy number of bubbles represented by the bubble class divided by the width of the class and the measuring time (10 s) [1/s*mm].

Here xy means that the distributions were calculated in consideration of the maximum square-equivalent bubble diameter in cross section of the tube (example see Fig. A.2, hdxy related to d).

Additionally, this kind of files supplies 3 bubble size distributions (hdv, hdrelv, hdnv) related to the volume-equivalent bubble diameter. Because these measurements were carried out only with one sensor, there are not radial velocity distributions for the gas phase. In this case the algorithm, that estimates the volume-equivalent bubble diameter, uses the time as the third coordinate in flow direction (see section 7.2).

A.6 Liquid velocity distribution

The algorithm for estimation of the liquid velocity, described in section 7.3, generates files which contain a matrix of velocity values for all crossing points of the sensor arranged according to their position in the measuring plane. Using this data of all available height positions, it is possible to create lateral and longitudinal views of the flow, as illustrated in Fig. 8.1. For the longitudinal views are interpolated between the velocity values of the cross sections along the diameter of the tube orthogonal to the straight edge of the half-moon diaphragm.

A.7 Lateral bubble velocities

Furthermore, using wire-mesh sensor data, it is possible to assess lateral components of local gas velocities (see section 7.5). The appropriate program generates a text file with 6 matrixes: The 1st and the 2nd contain tables of the velocity components in x direction for bubbles bigger and smaller than a limit bubble diameter respectively. In this case the limit was the Tomiyama diameter, which is relevant for the lift force. The 3rd and 4th contain the same information but in y direction and the 5th and 6th show the lateral velocity components in x and y direction averaged for all bubbles. Using this kind of files a special visualisation program makes pictures like in Fig. 8.10 or Fig.8.11.

Attachment B: Void fraction and liquid velocity distributions

B.1 Time averaged void fraction and liquid velocity distributions up- and downstream of the obstacle for air-water test runs at ambient conditions

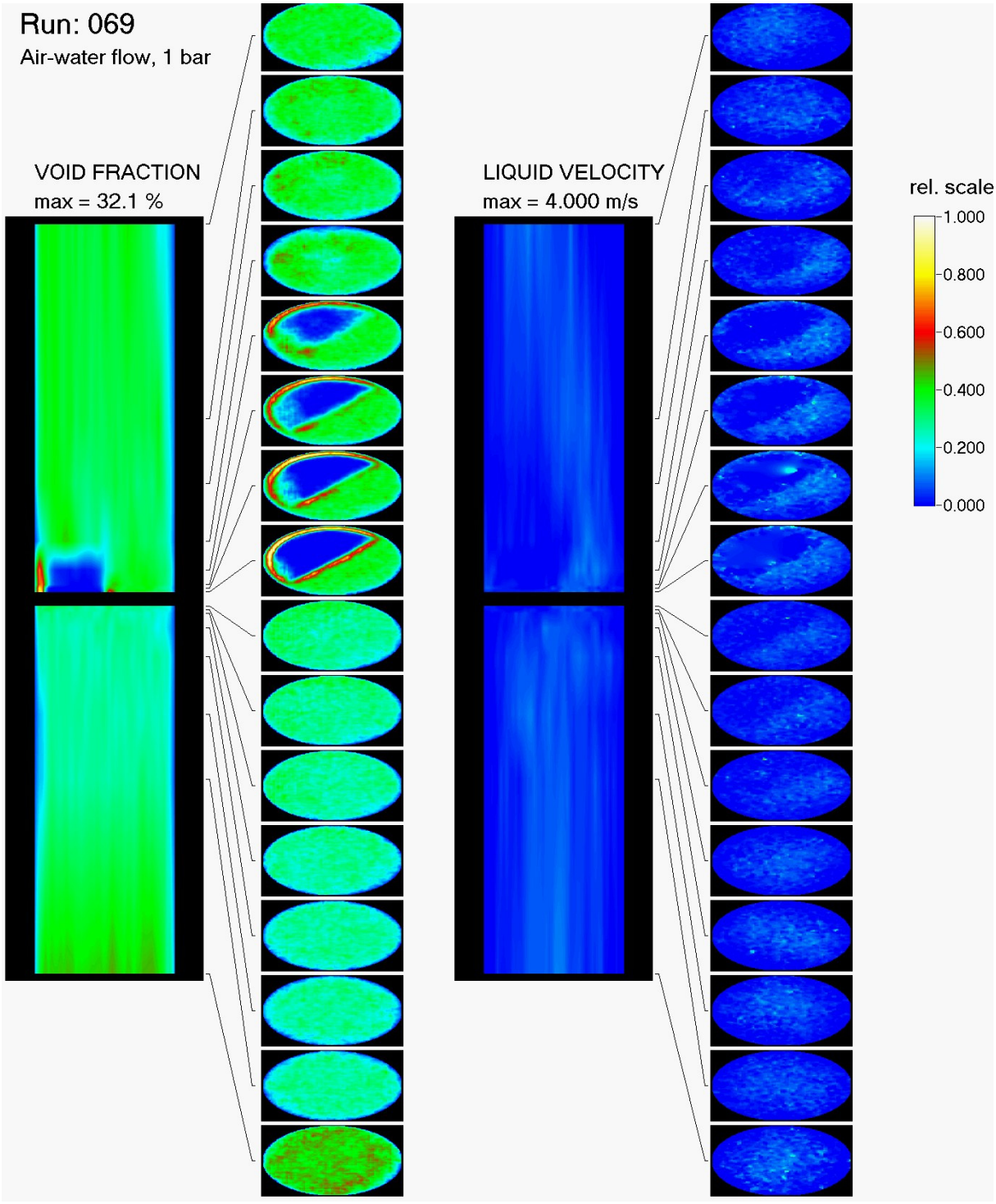

Fig. B.1 Test run 069, J_L = 0.102 m/s, J_G = 0.0368 m/s (at injection position)

Attachment B: Void fraction and liquid velocity distributions

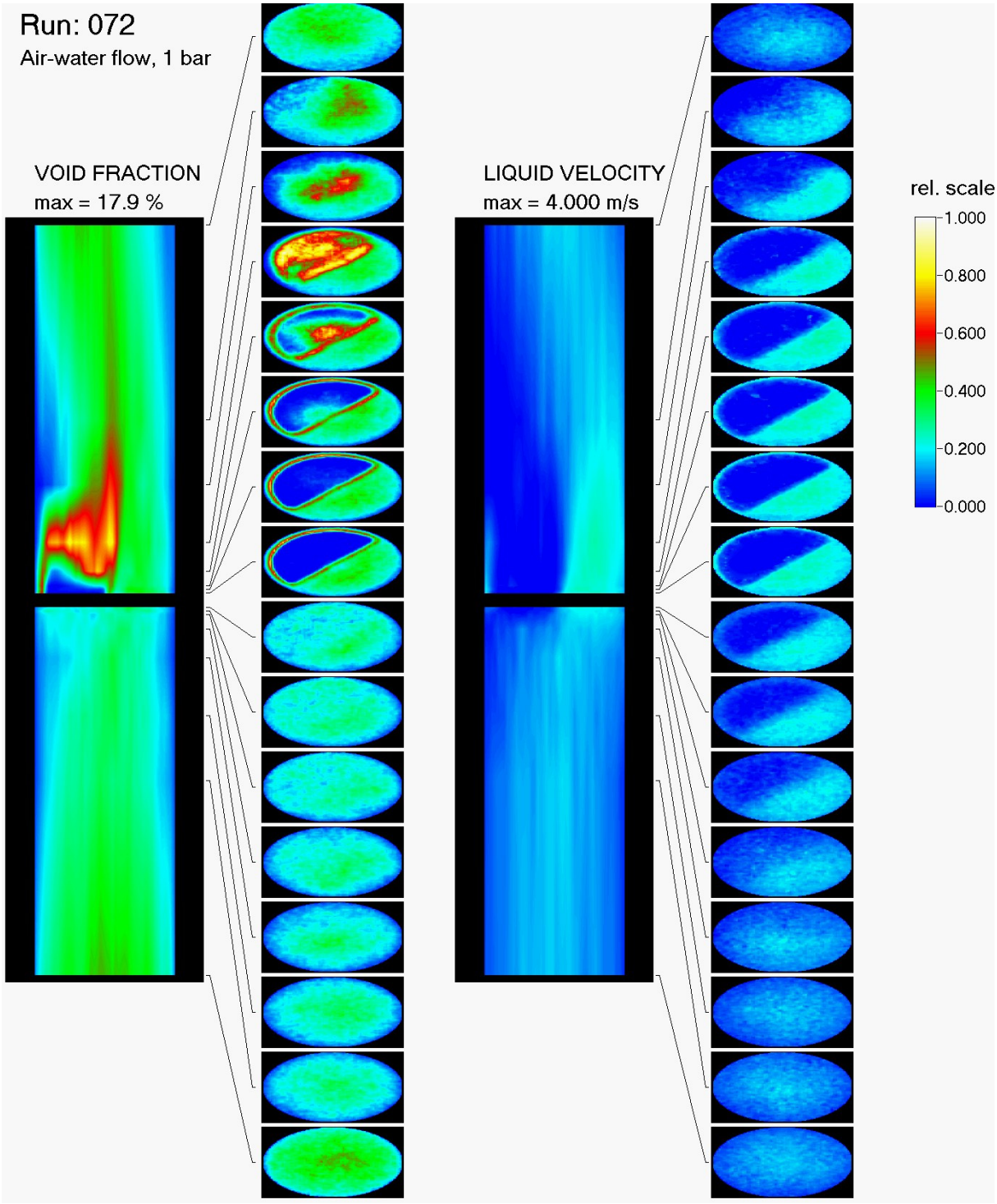

Fig. B.2 Test run 072, J_L = 0.405 m/s, J_G = 0.0368 m/s (at injection position)

Attachment B: Void fraction and liquid velocity distributions

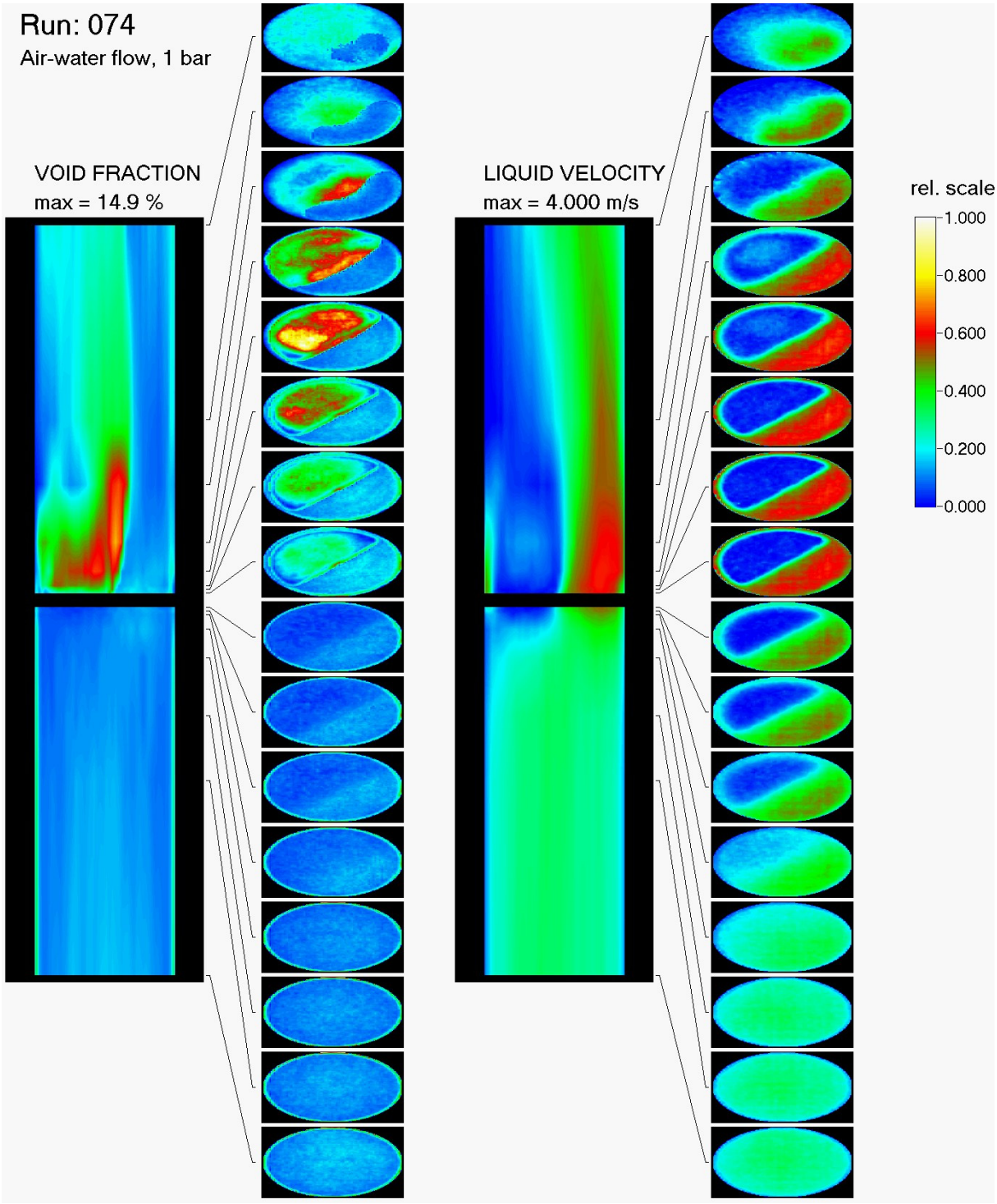

Fig. B.3 Test run 074, J_L = 1.017 m/s, J_G = 0.0368 m/s (at injection position)

Attachment B: Void fraction and liquid velocity distributions

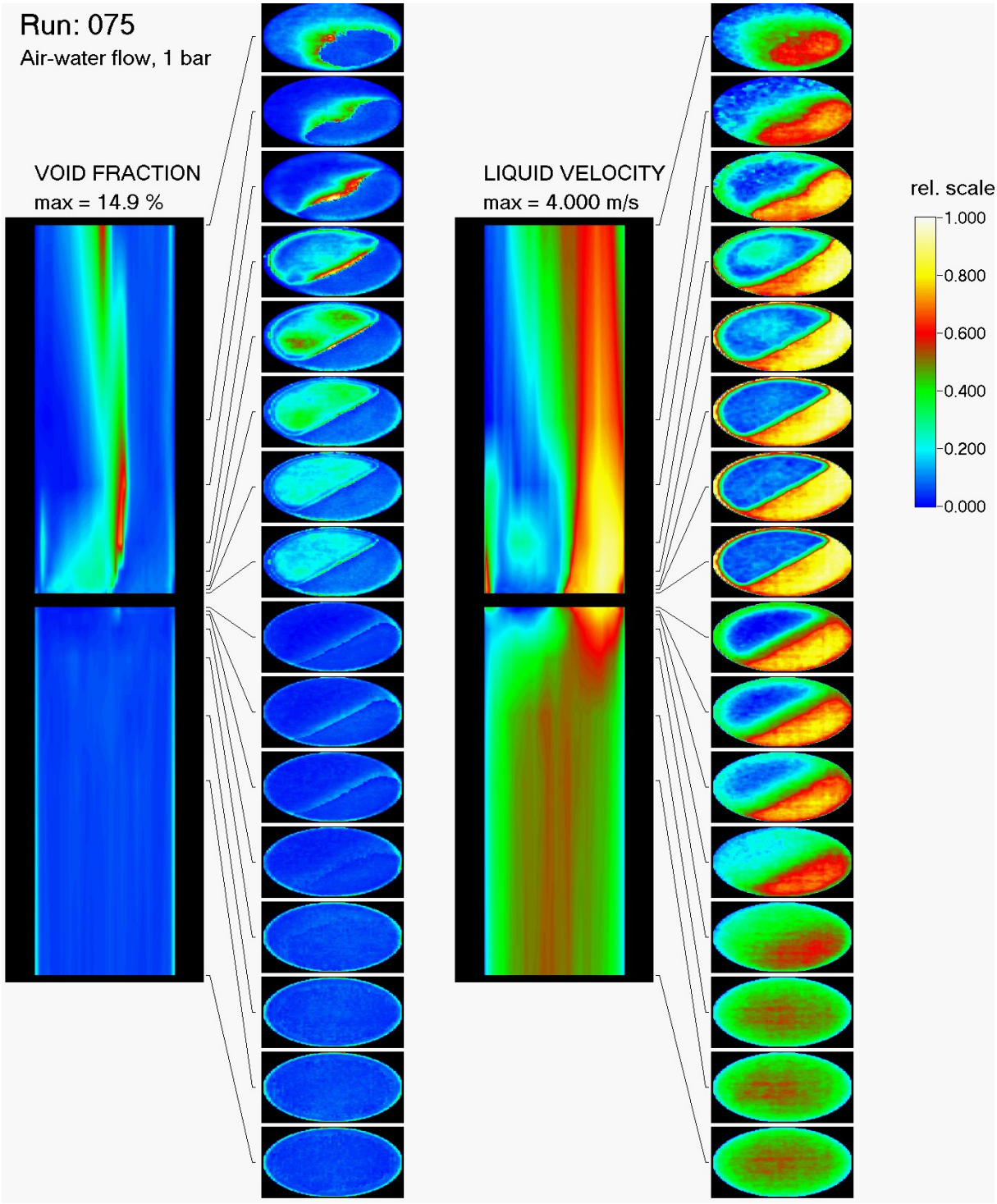

Fig. B.4 Test run 075, J_L = 1.611 m/s, J_G = 0.0368 m/s (at injection position)

Attachment B: Void fraction and liquid velocity distributions

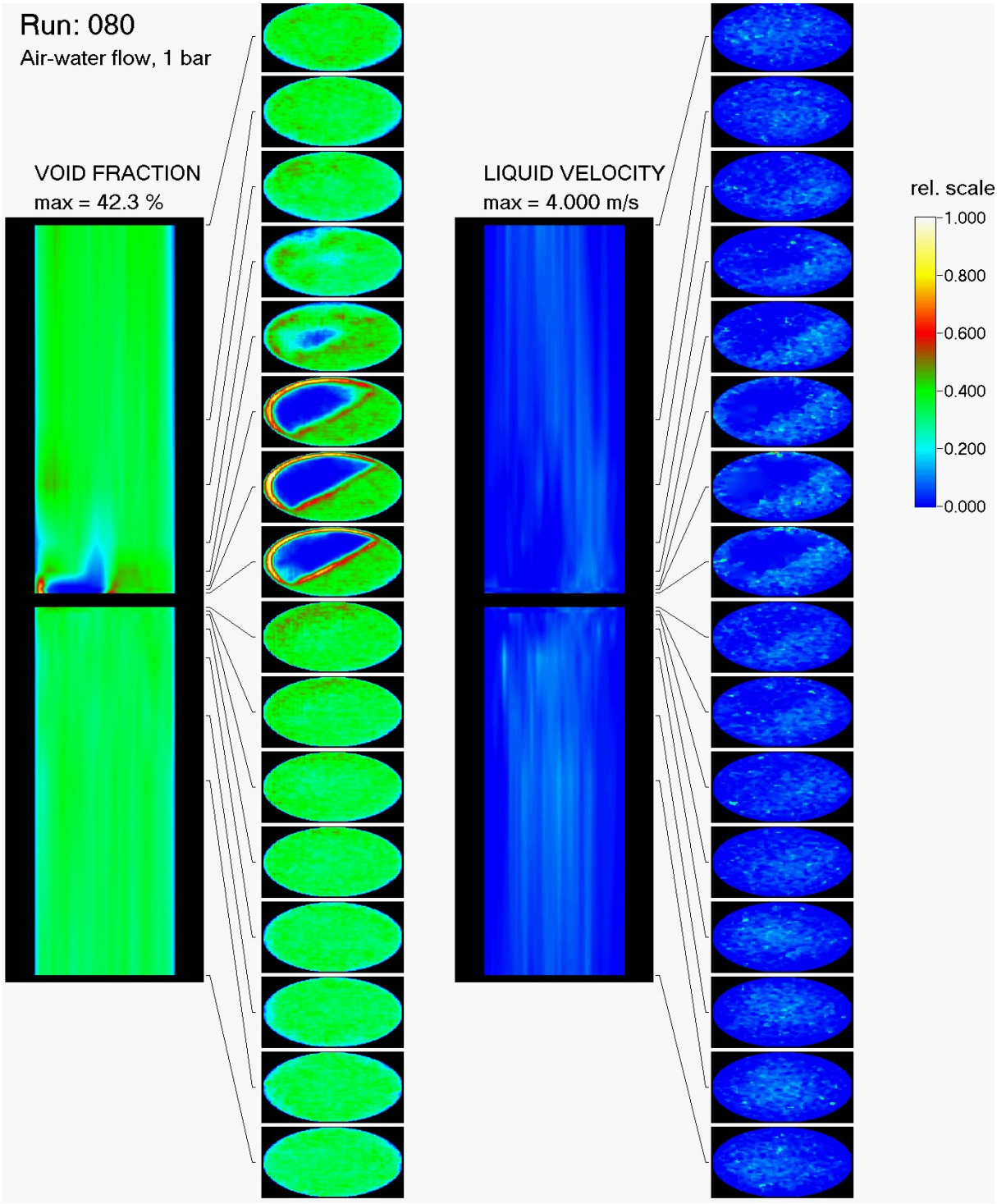

Fig. B.5 Test run 080, J_L = 0.102 m/s, J_G = 0.0574 m/s (at injection position)

Attachment B: Void fraction and liquid velocity distributions

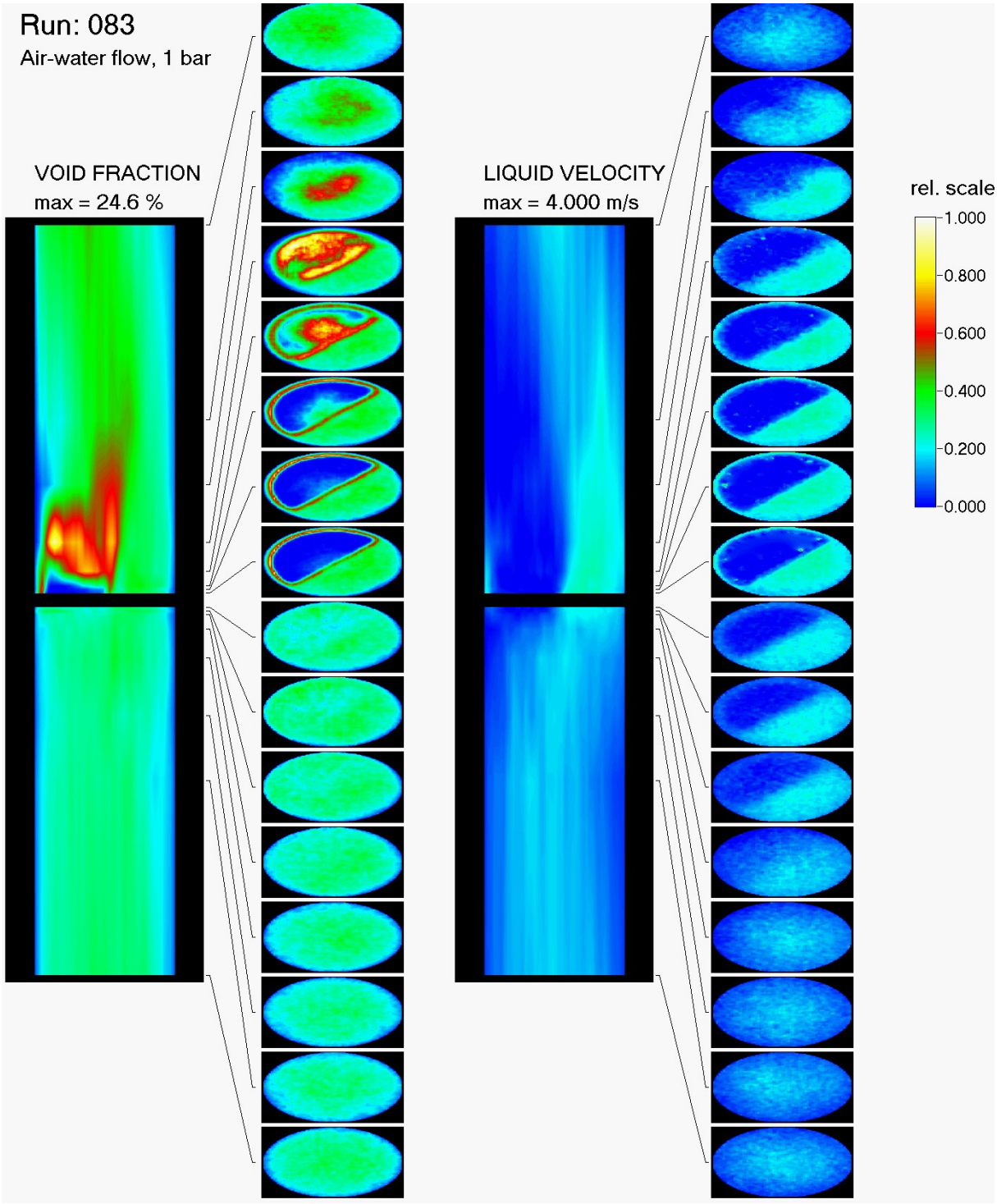

Fig. B.6 Test run 083, J_L = 0.405 m/s, J_G = 0.0574 m/s (at injection position)

Attachment B: Void fraction and liquid velocity distributions

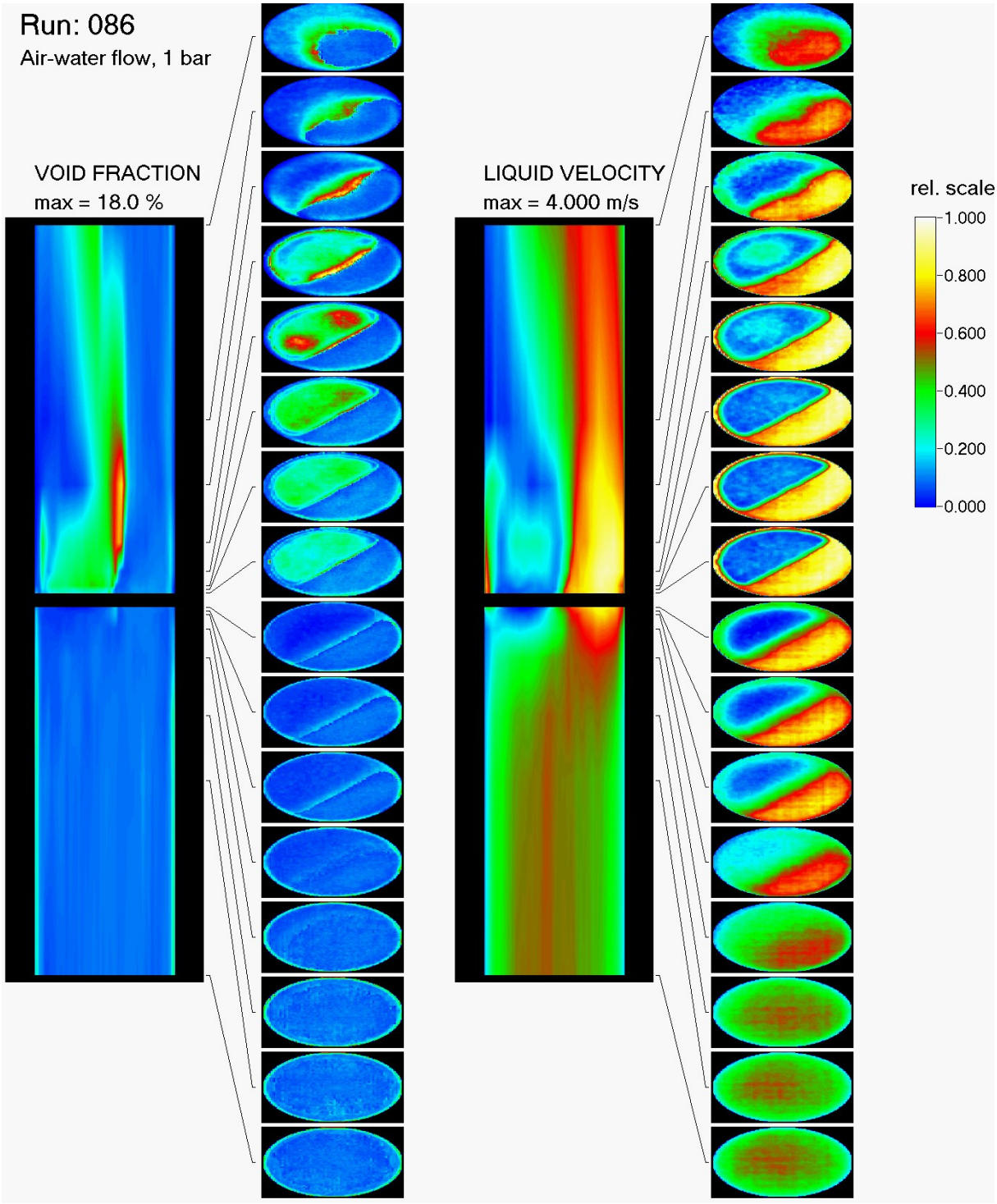

Fig. B.7 Test run 086, J_L = 1.611 m/s, J_G = 0.0574 m/s (at injection position)

Attachment B: Void fraction and liquid velocity distributions

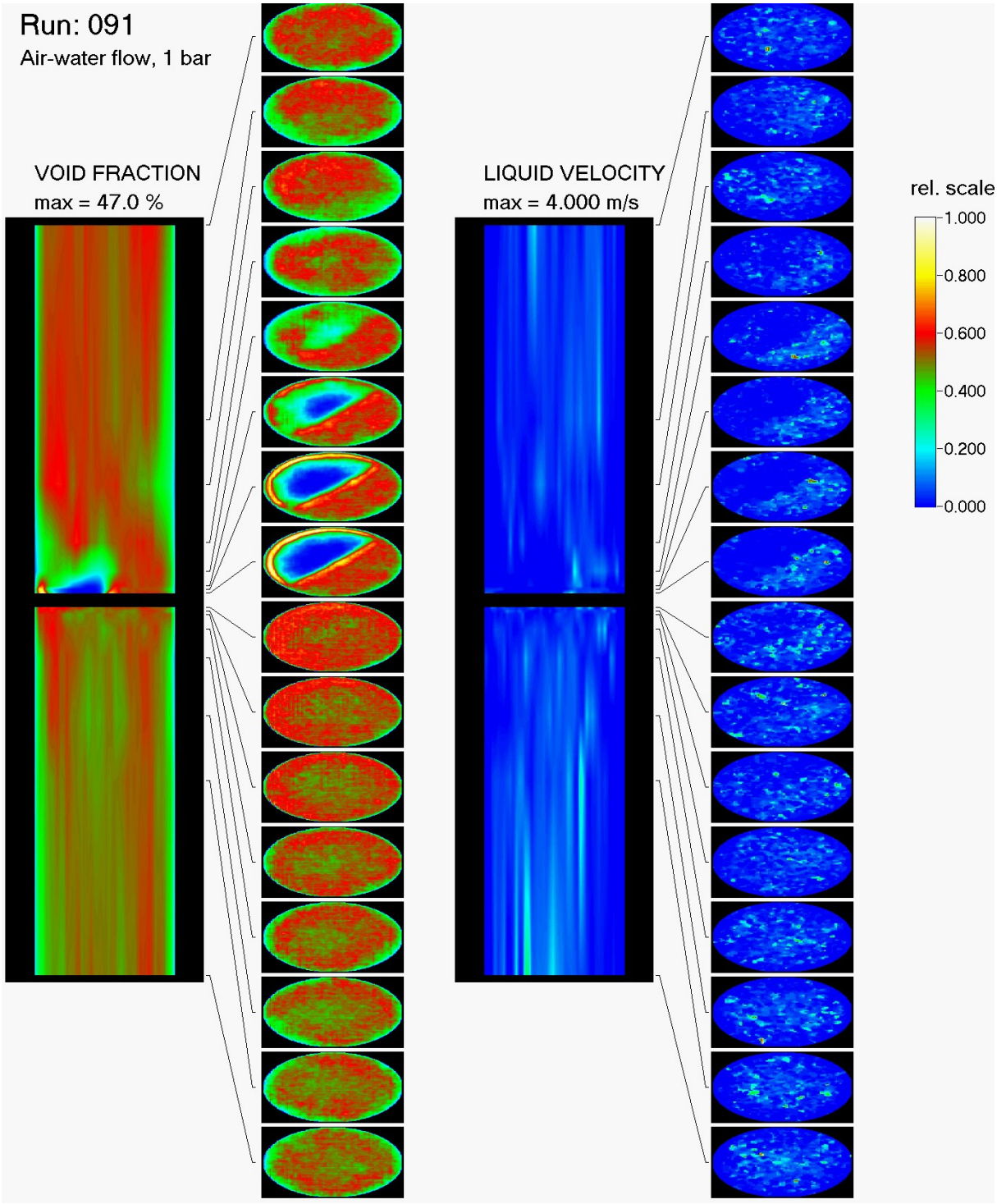

Fig. B.8 Test run 091, J_L = 0.102 m/s, J_G = 0.0898 m/s (at injection position)

Attachment B: Void fraction and liquid velocity distributions

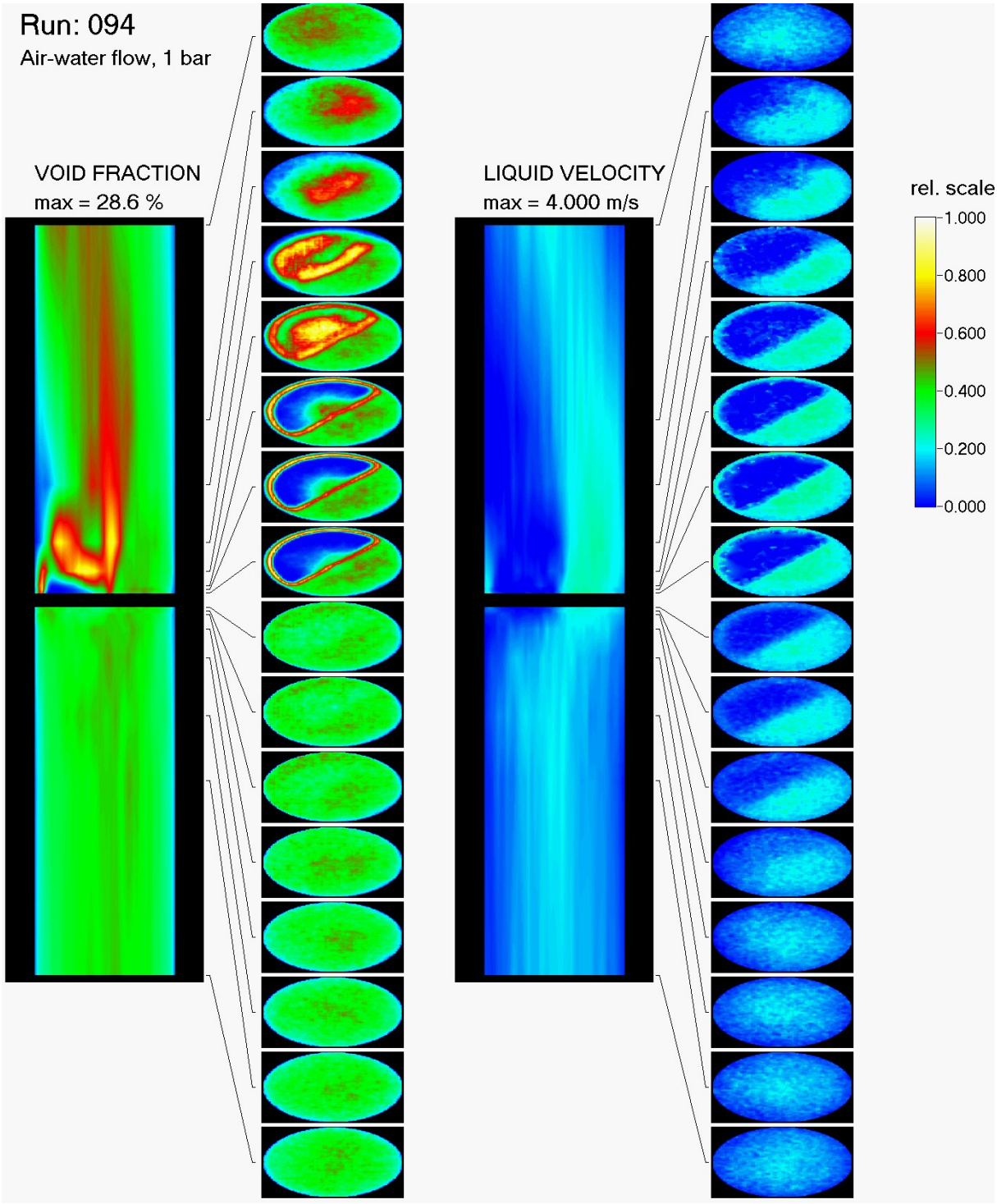

Fig. B.9 Test run 094, J_L = 0.405 m/s, J_G = 0.0898 m/s (at injection position)

Attachment B: Void fraction and liquid velocity distributions

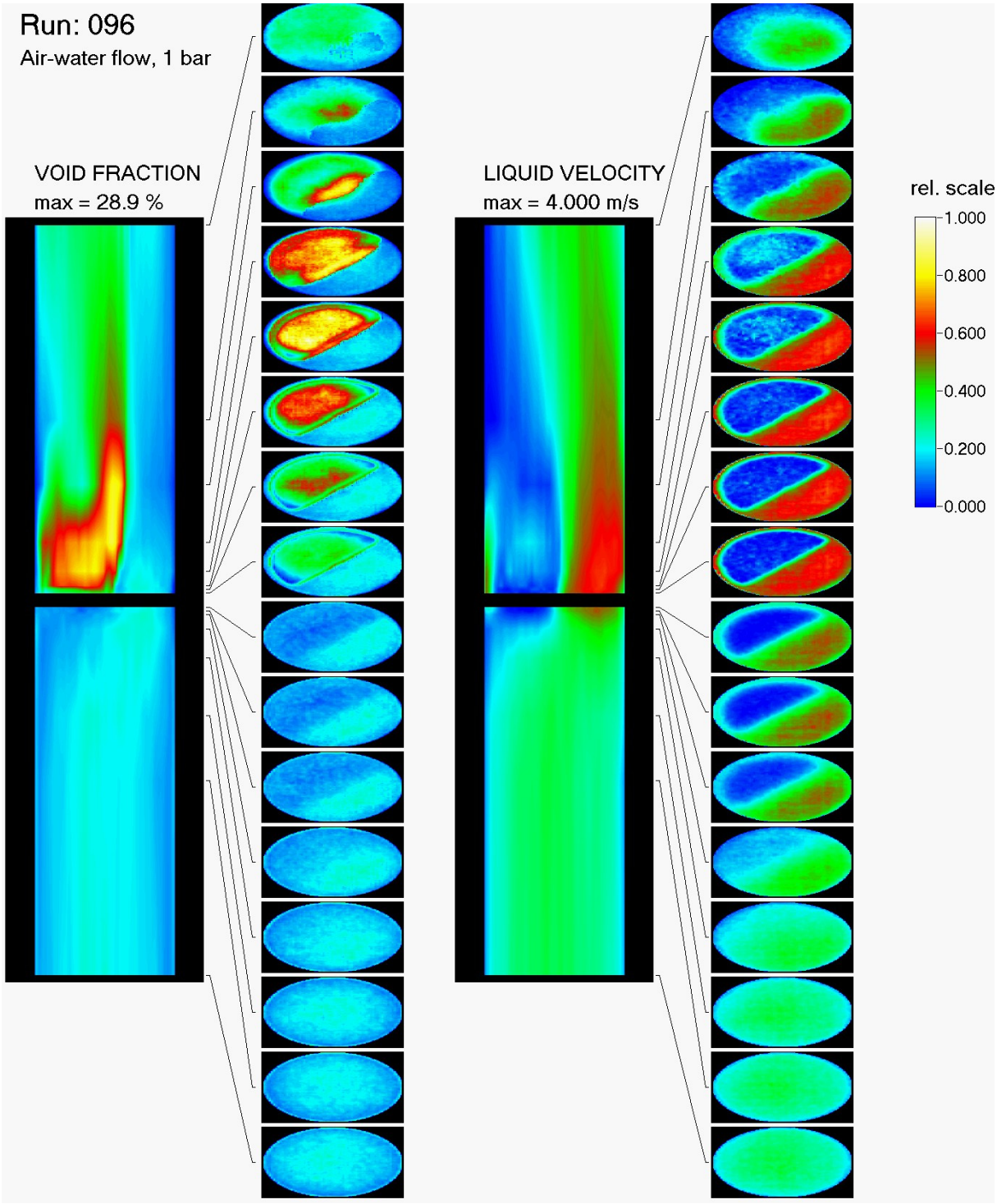

Fig. B.10 Test run 096, J_L = 1.017 m/s, J_G = 0.0898 m/s (at injection position)

Attachment B: Void fraction and liquid velocity distributions

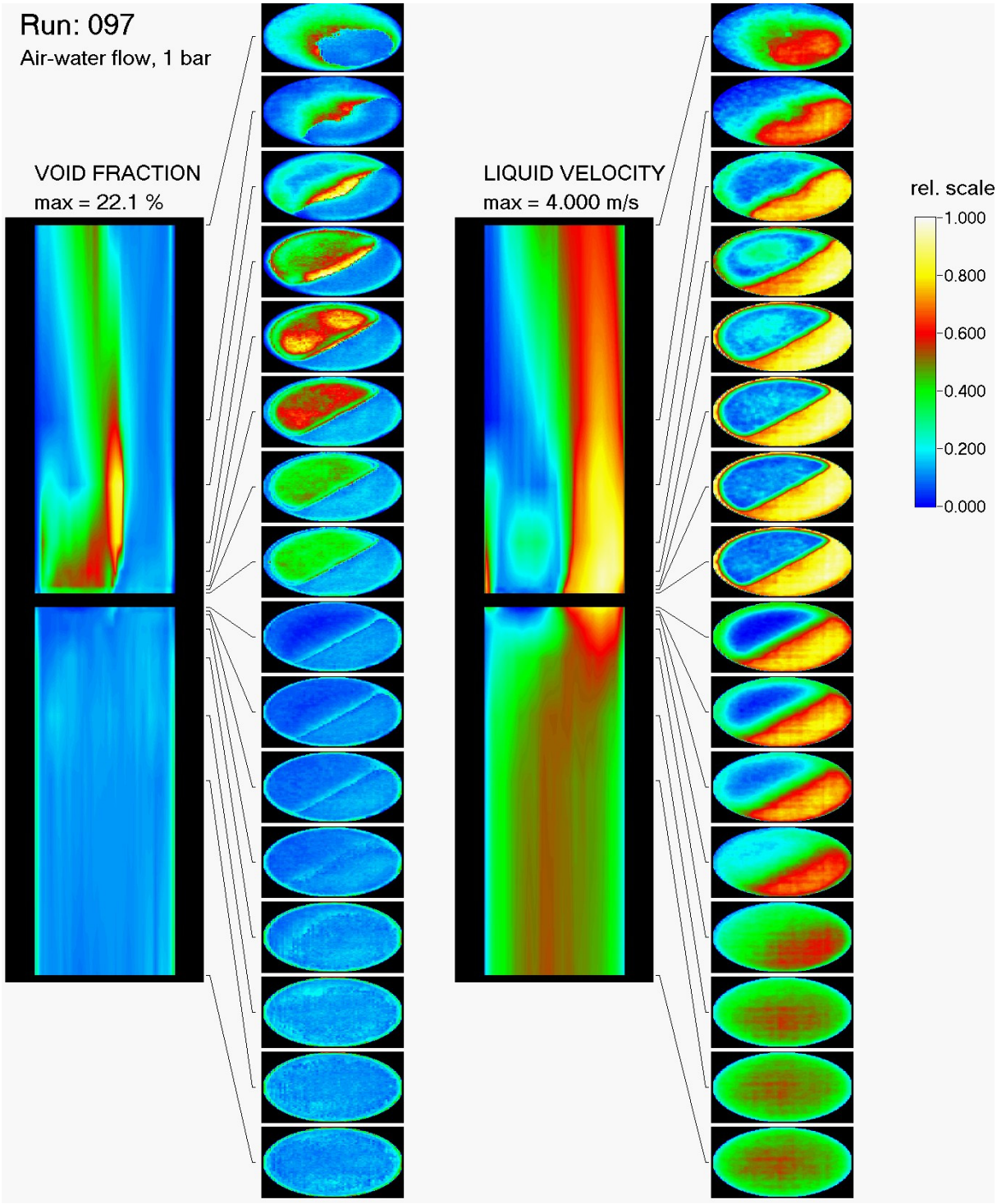

Fig. B.11 Test run 097, J_L = 1.611 m/s, J_G = 0.0898 m/s (at injection position)

Attachment B: Void fraction and liquid velocity distributions

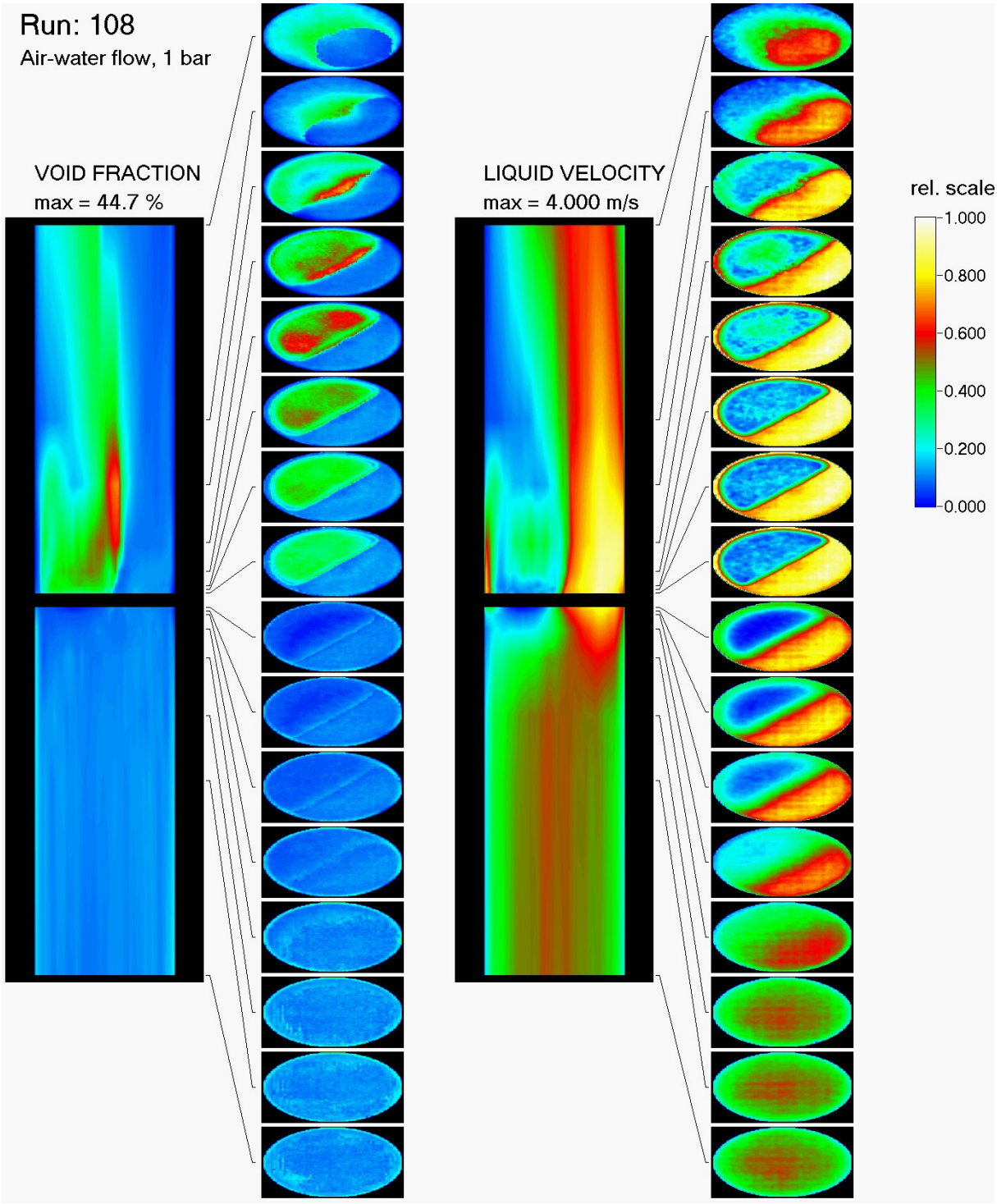

Fig. B.12 Test run 108, J_L = 1.611 m/s, J_G = 0.14 m/s (at injection position)

Attachment B: Void fraction and liquid velocity distributions

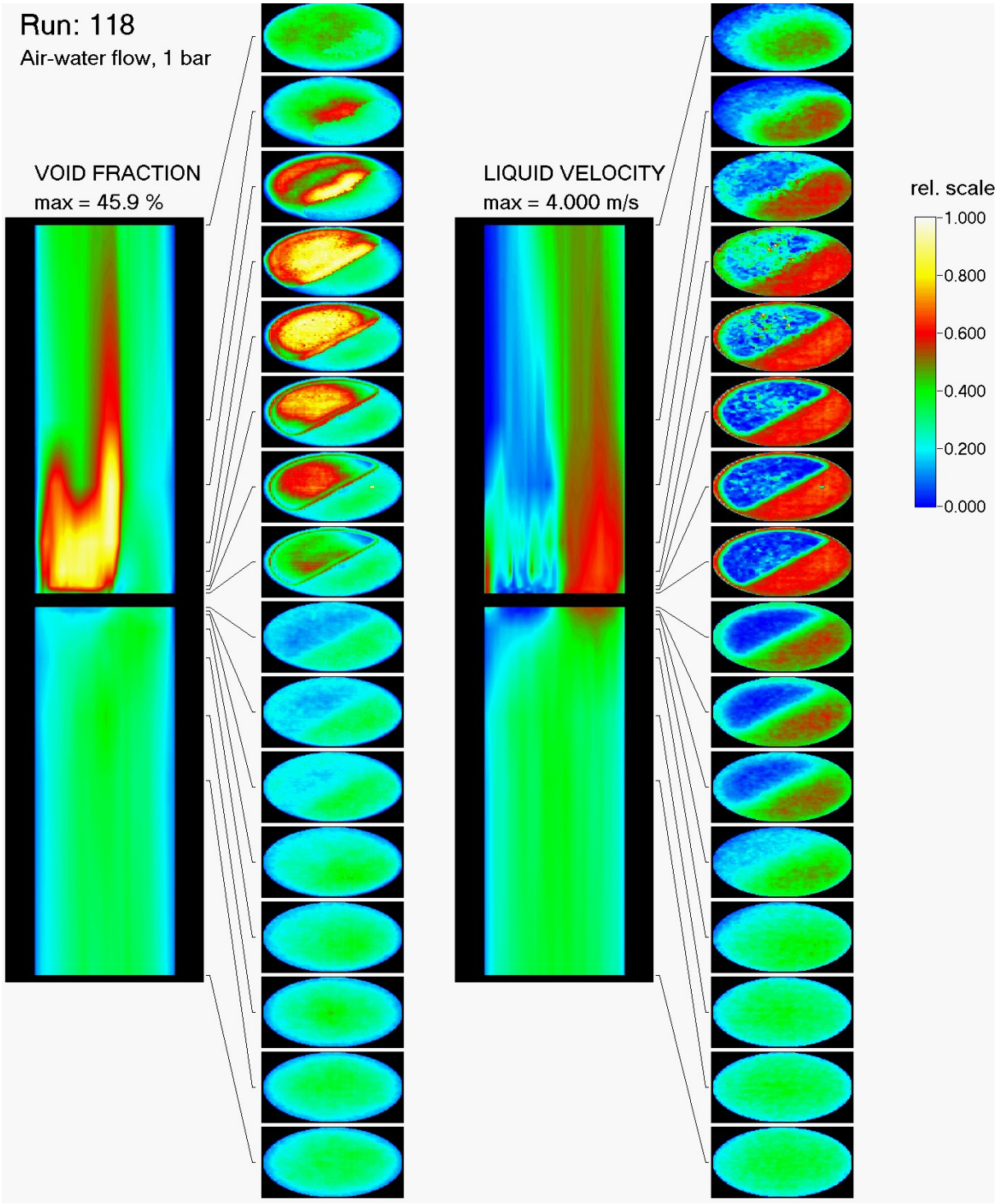

Fig. B.13 Test run 118, J_L = 1.017 m/s, J_G = 0.219 m/s (at injection position)

Attachment B: Void fraction and liquid velocity distributions

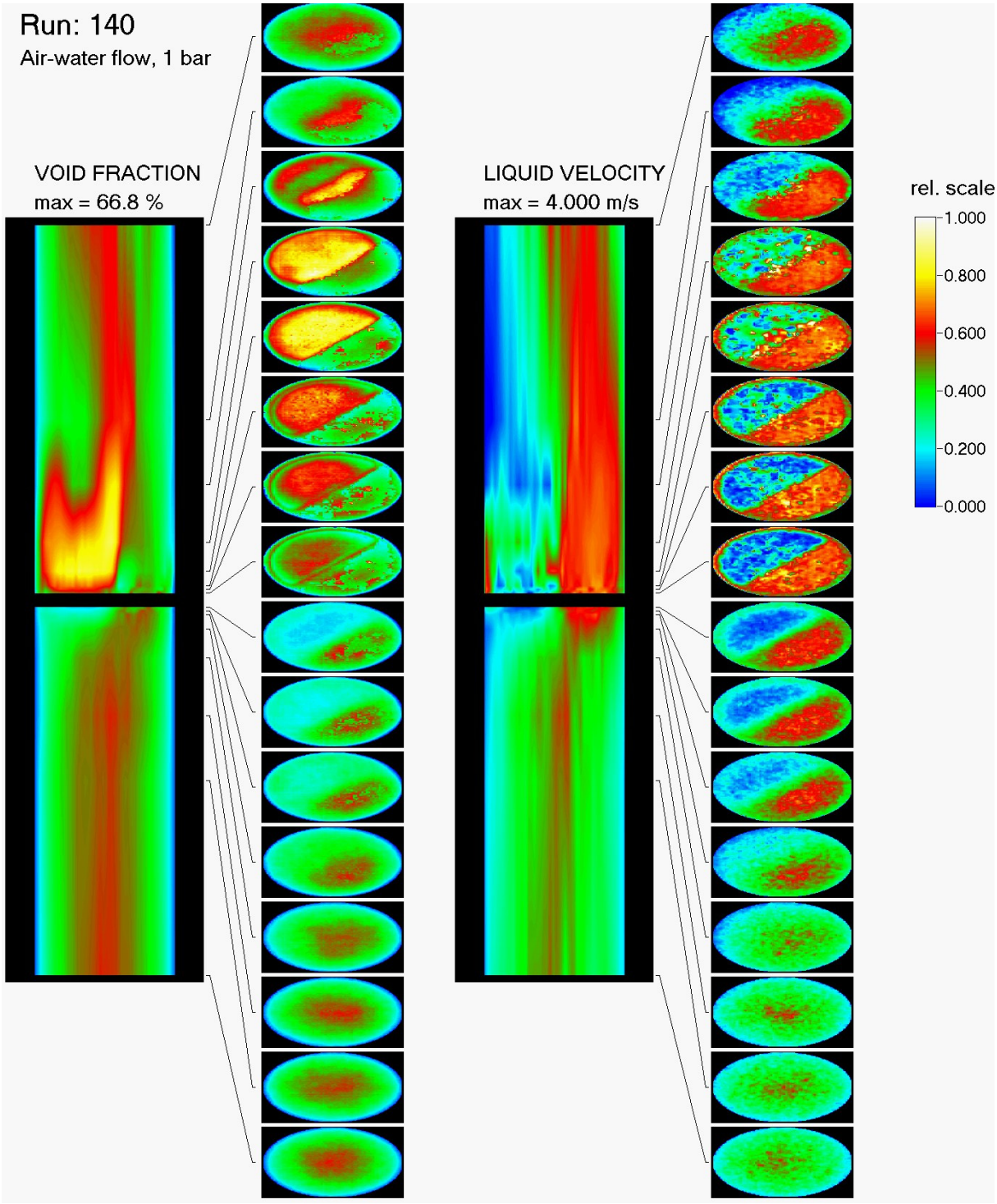

Fig. B.14 Test run 140, J_L = 1.017 m/s, J_G = 0.534 m/s (at injection position)

Attachment B: Void fraction and liquid velocity distributions

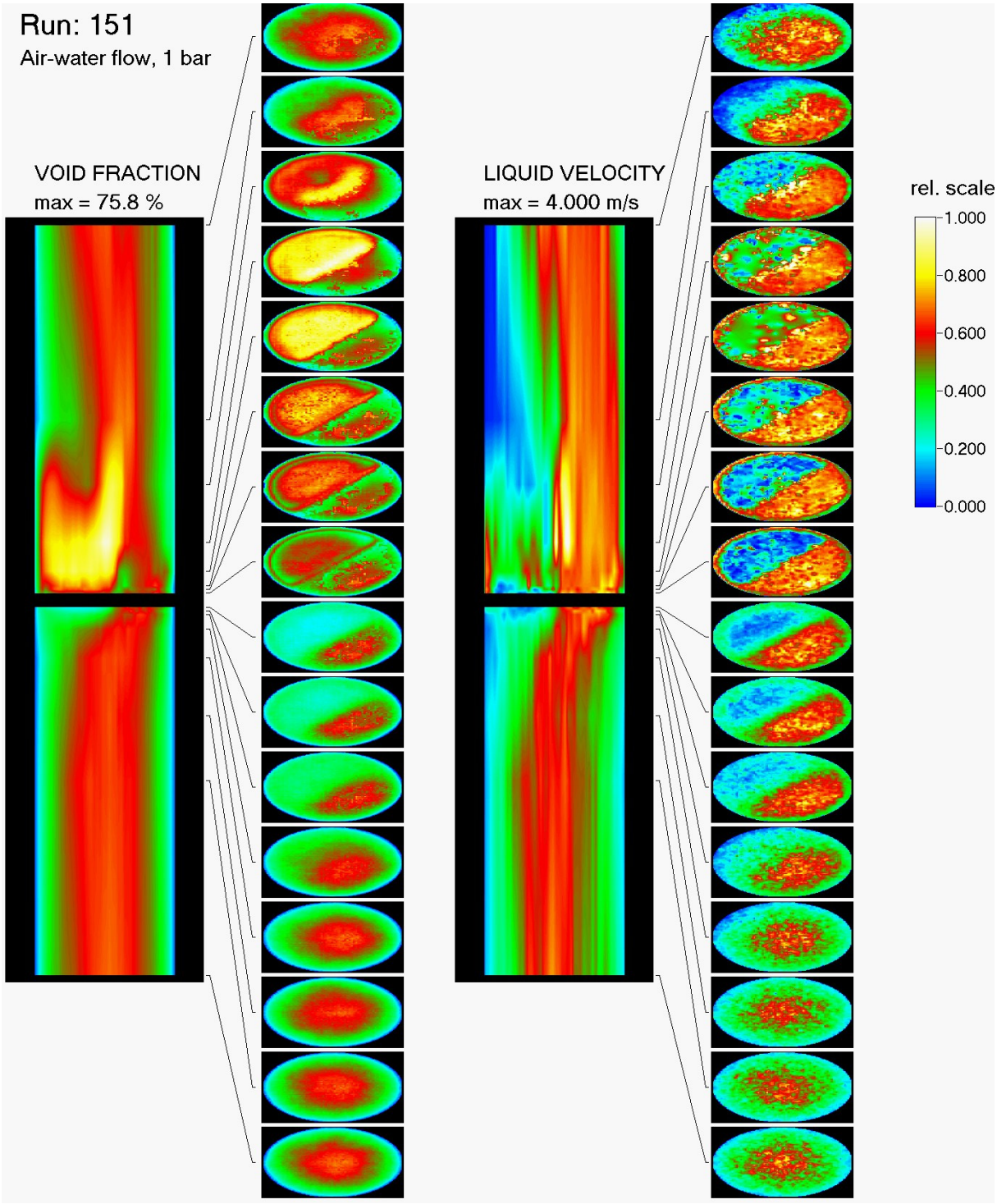

Fig. B.15 Test run 151, J_L = 1.017 m/s, J_G = 0.835 m/s (at injection position)

Attachment B: Void fraction and liquid velocity distributions

B.2 Time averaged void fraction and liquid velocity distributions up- and downstream of the obstacle for steam-water test runs at 6.5 MPa

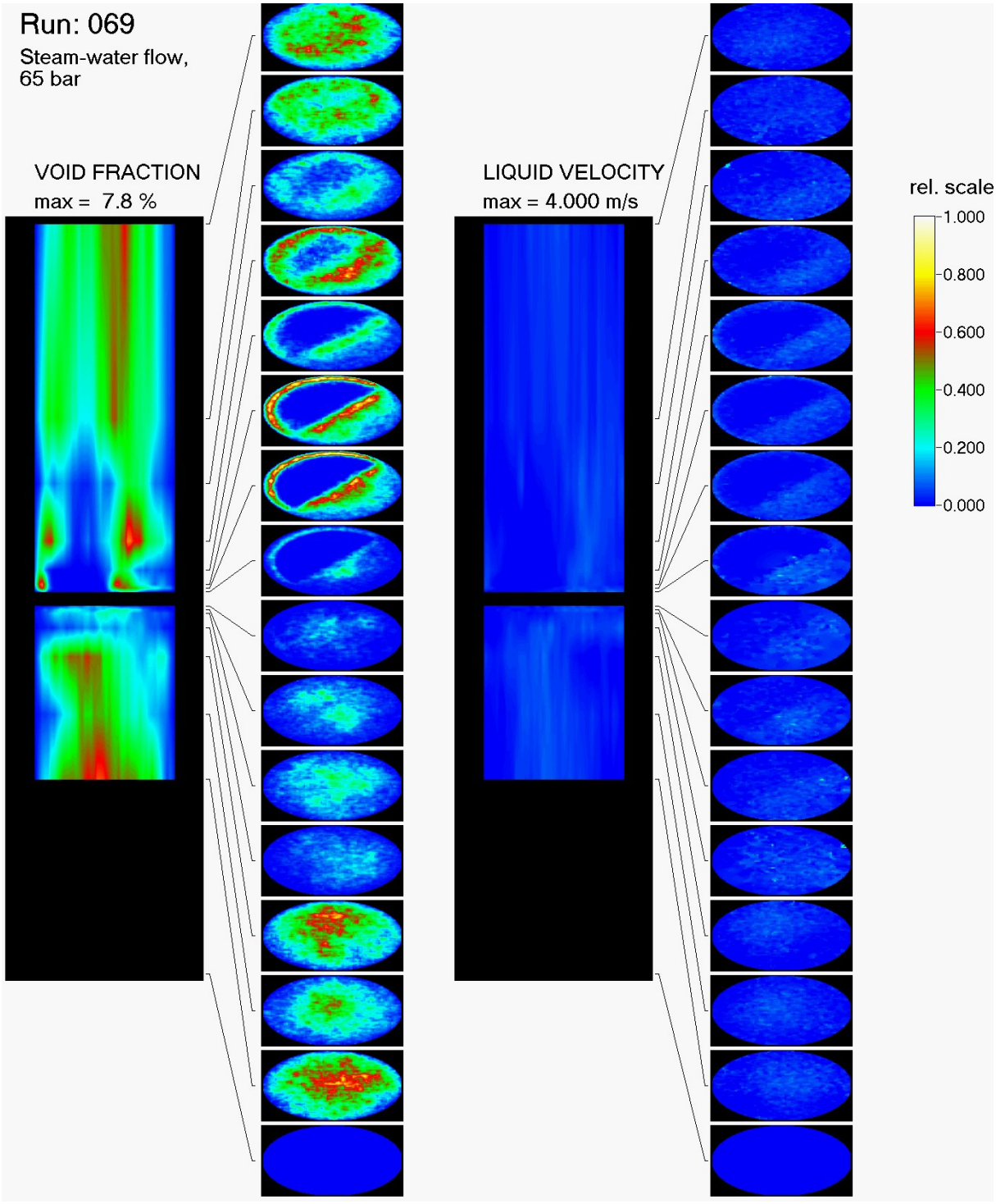

Fig. B.16 Test run 069, J_L = 0.102 m/s, J_G = 0.0368 m/s (at injection position)

Attachment B: Void fraction and liquid velocity distributions

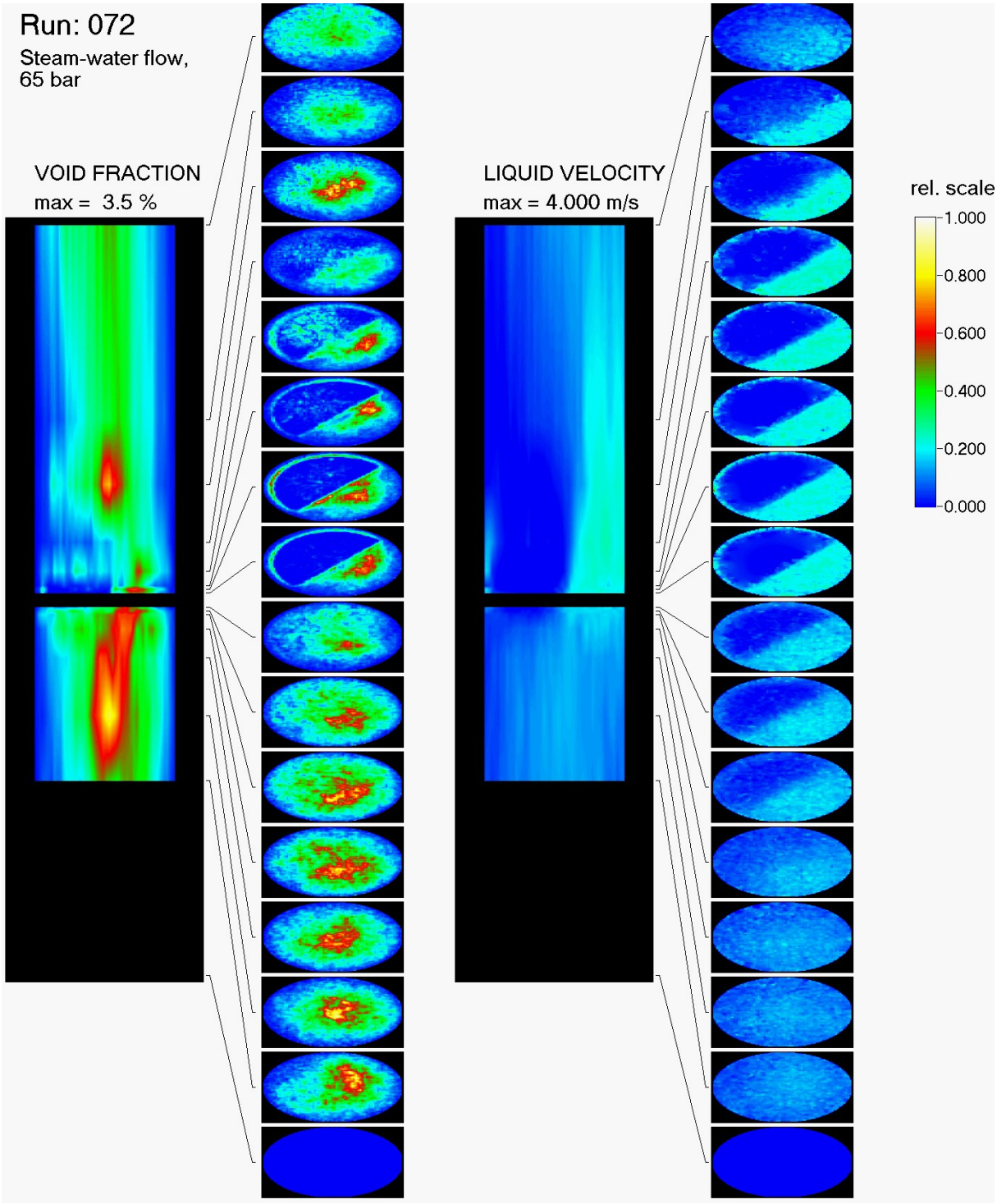

Fig. B.17 Test run 072, J_L = 0.405 m/s, J_G = 0.0368 m/s (at injection position)

Attachment B: Void fraction and liquid velocity distributions

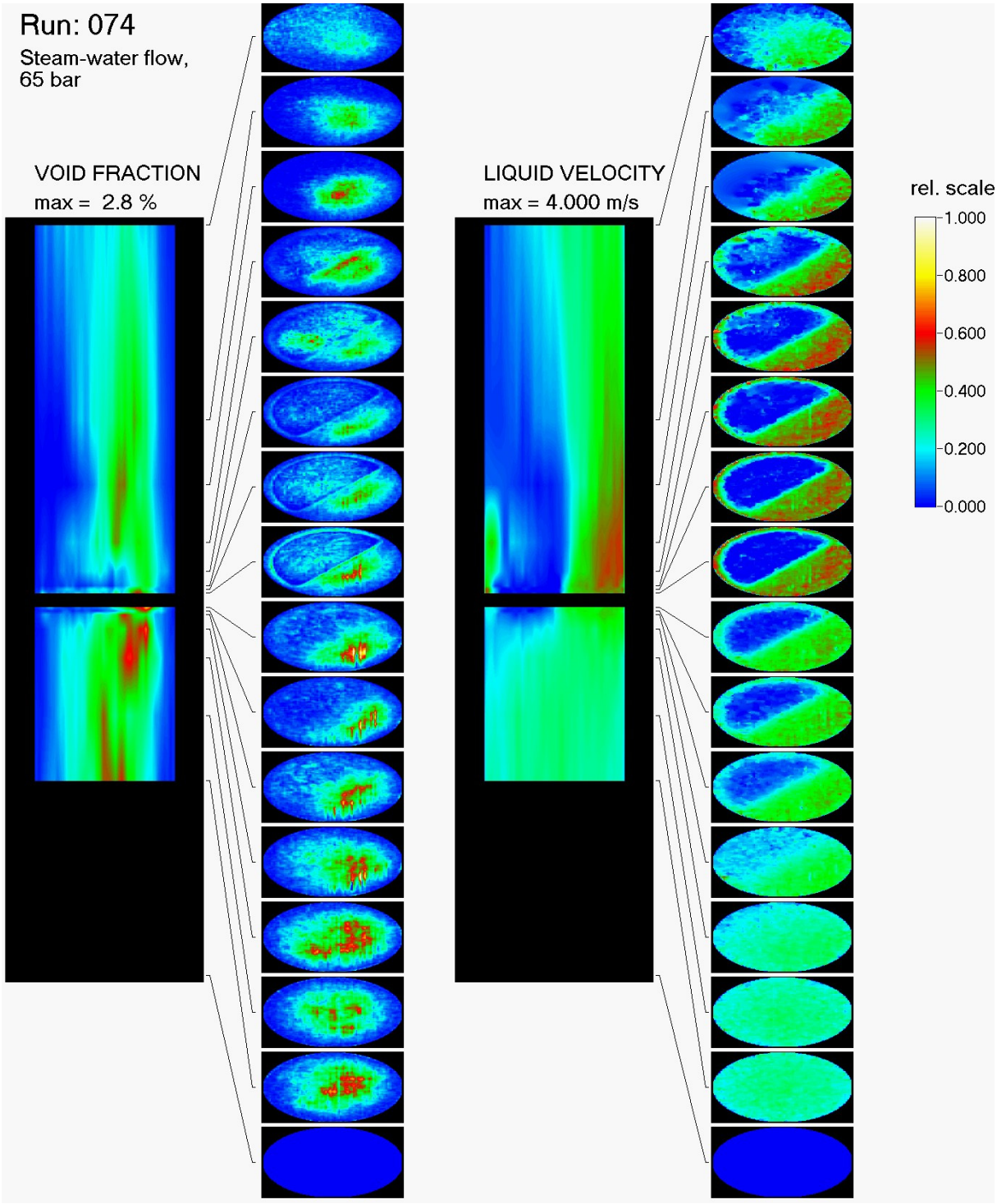

Fig. B.18 Test run 074, J_L = 1.017 m/s, J_G = 0.0368 m/s (at injection position)

Attachment B: Void fraction and liquid velocity distributions

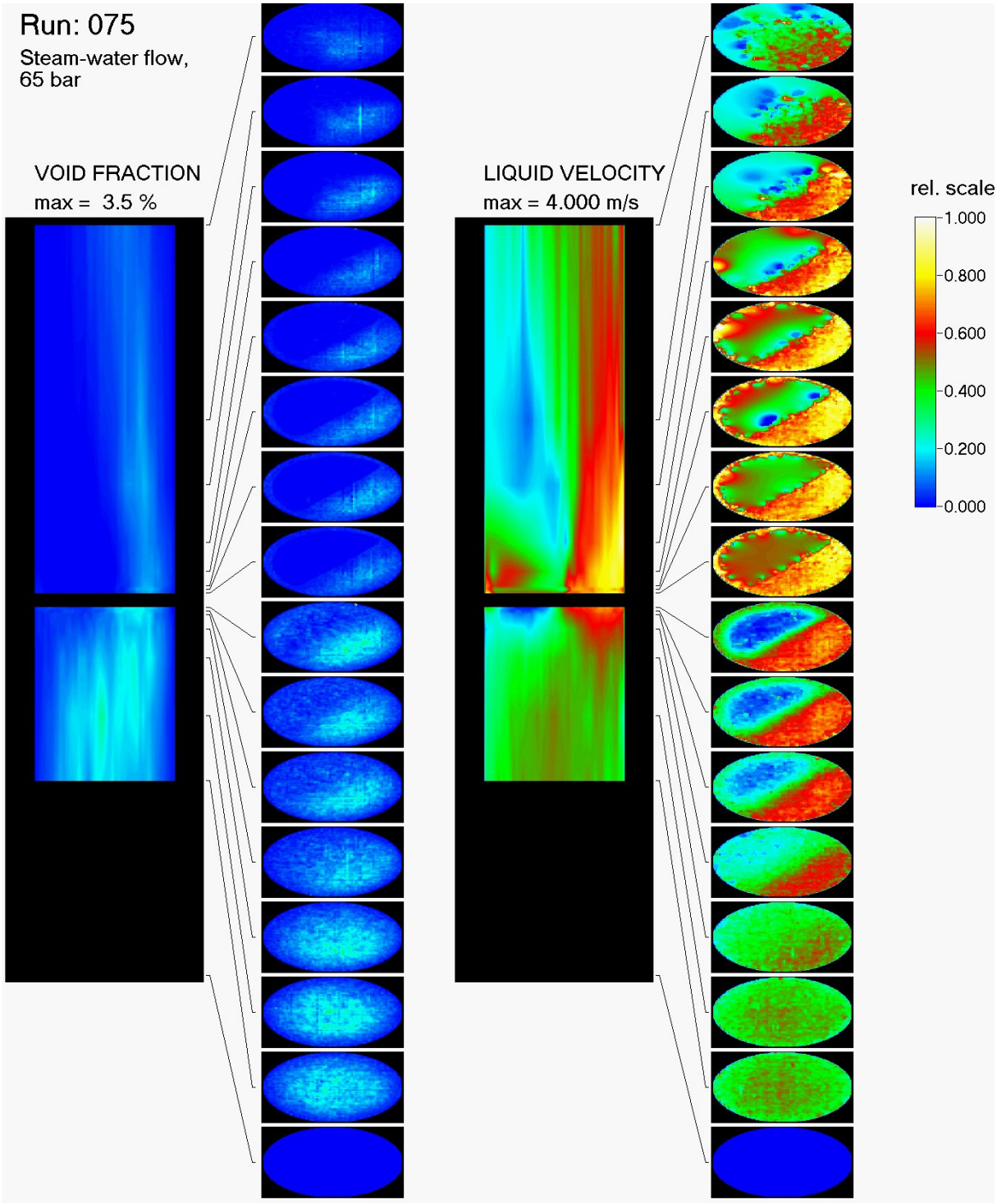

Fig. B.19 Test run 075, J_L = 1.611 m/s, J_G = 0.0368 m/s (at injection position)

Attachment B: Void fraction and liquid velocity distributions

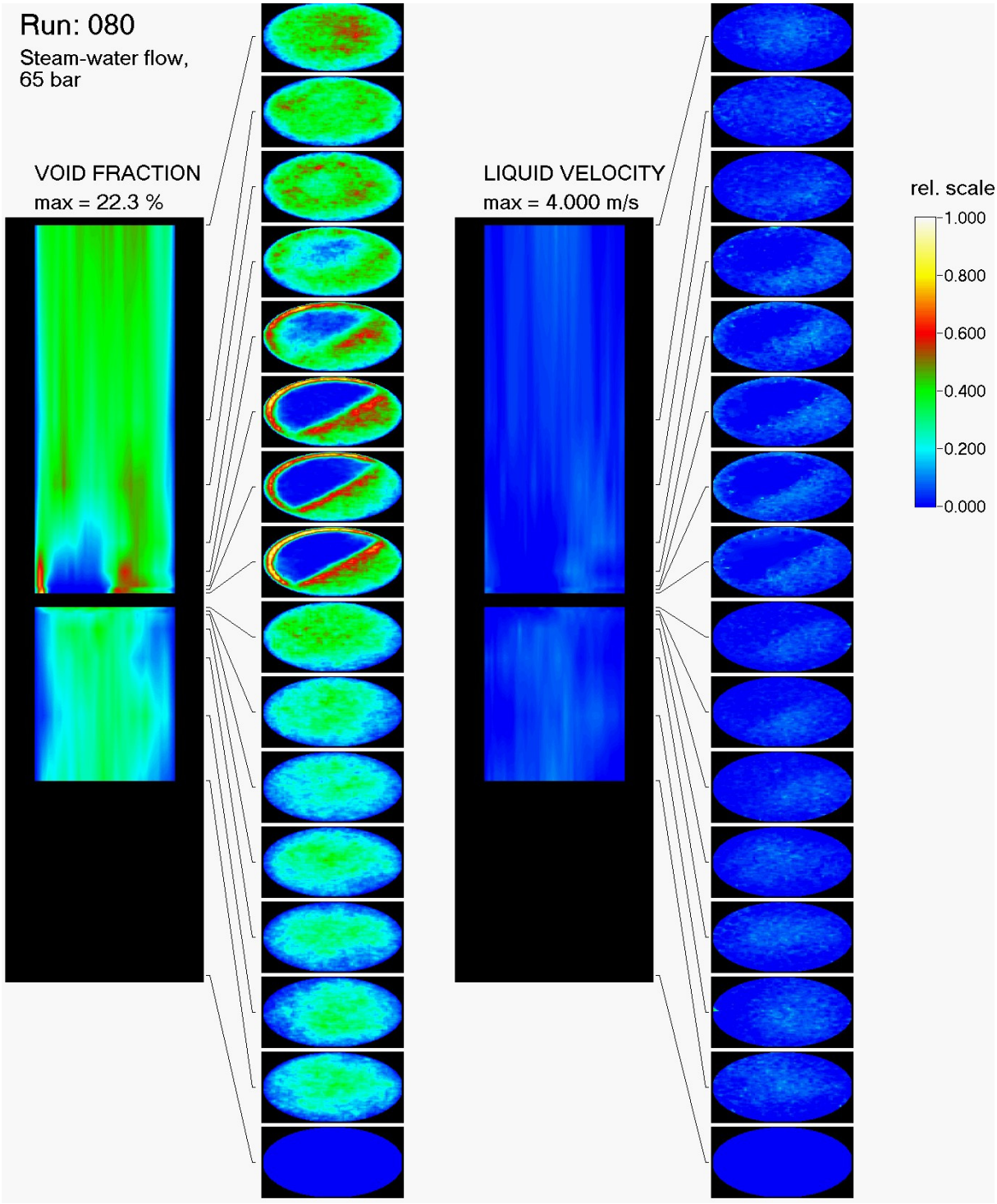

Fig. B.20 Test run 080, J_L = 0.102 m/s, J_G = 0.0574 m/s (at injection position)

Attachment B: Void fraction and liquid velocity distributions

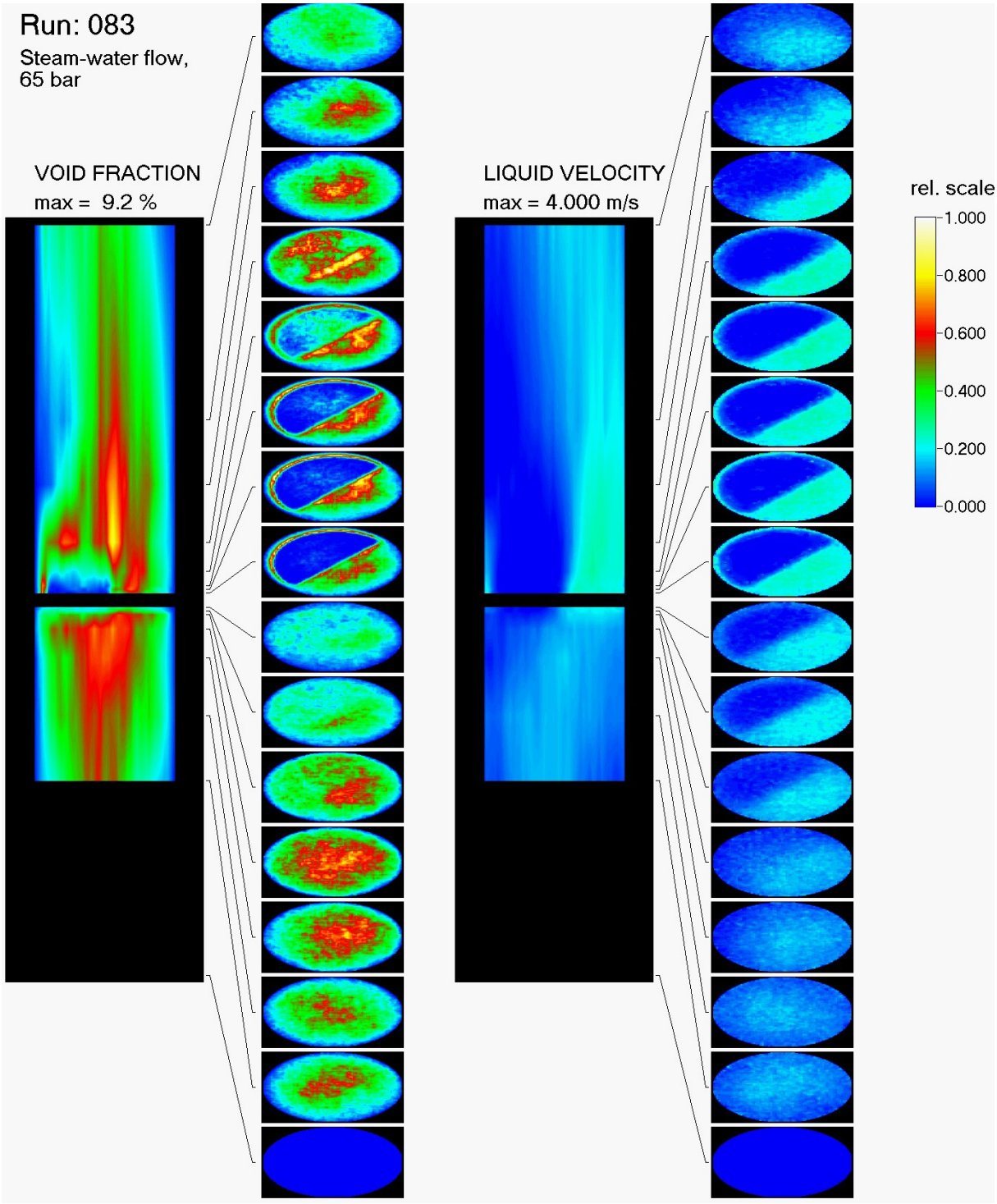

Fig. B.21 Test run 083, J_L = 0.405 m/s, J_G = 0.0574 m/s (at injection position)

Attachment B: Void fraction and liquid velocity distributions

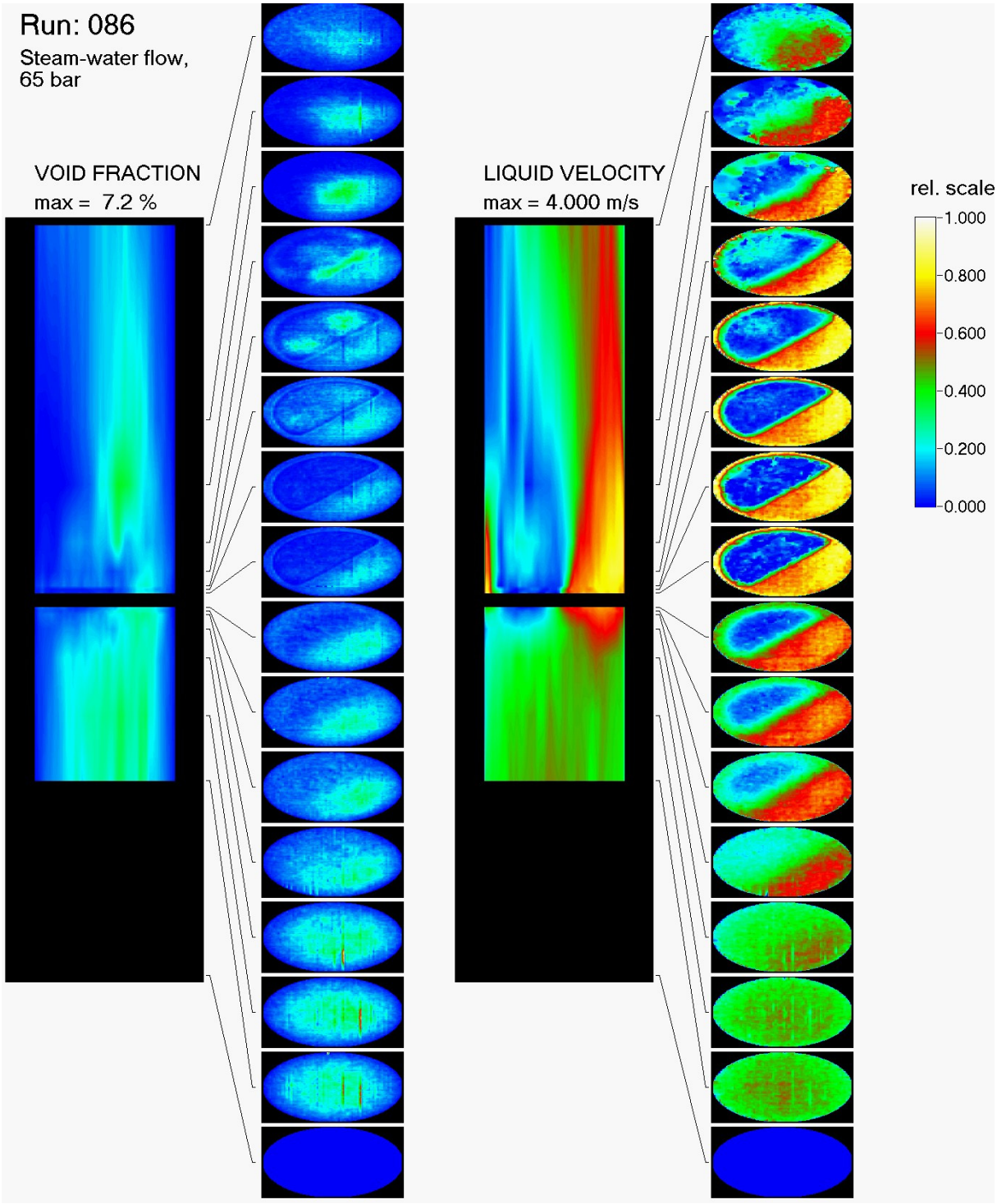

Fig. B.22 Test run 086, J_L = 1.611 m/s, J_G = 0.0574 m/s (at injection position)

Attachment B: Void fraction and liquid velocity distributions

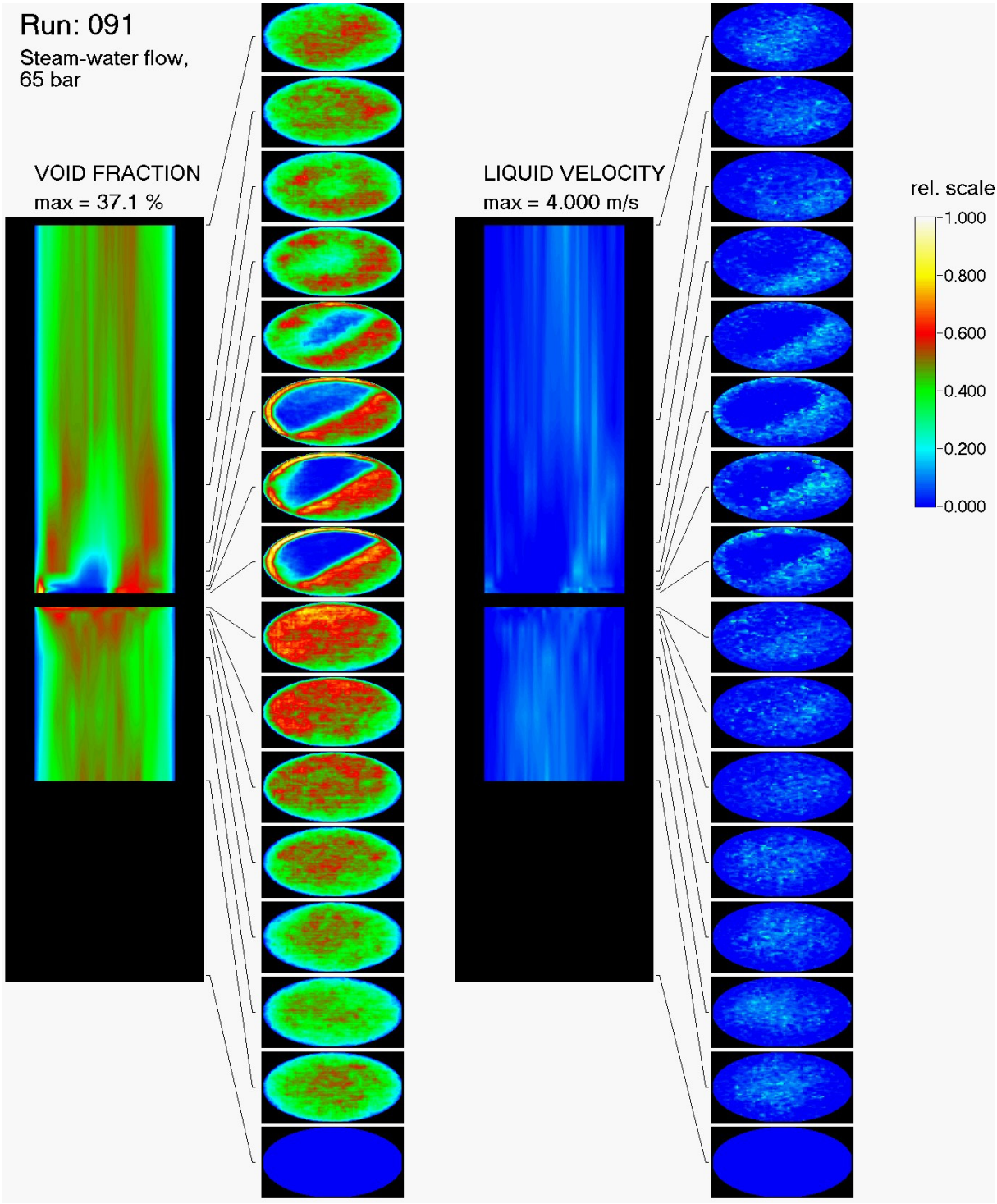

Fig. B.23 Test run 091, J_L = 0.102 m/s, J_G = 0.0898 m/s (at injection position)

Attachment B: Void fraction and liquid velocity distributions

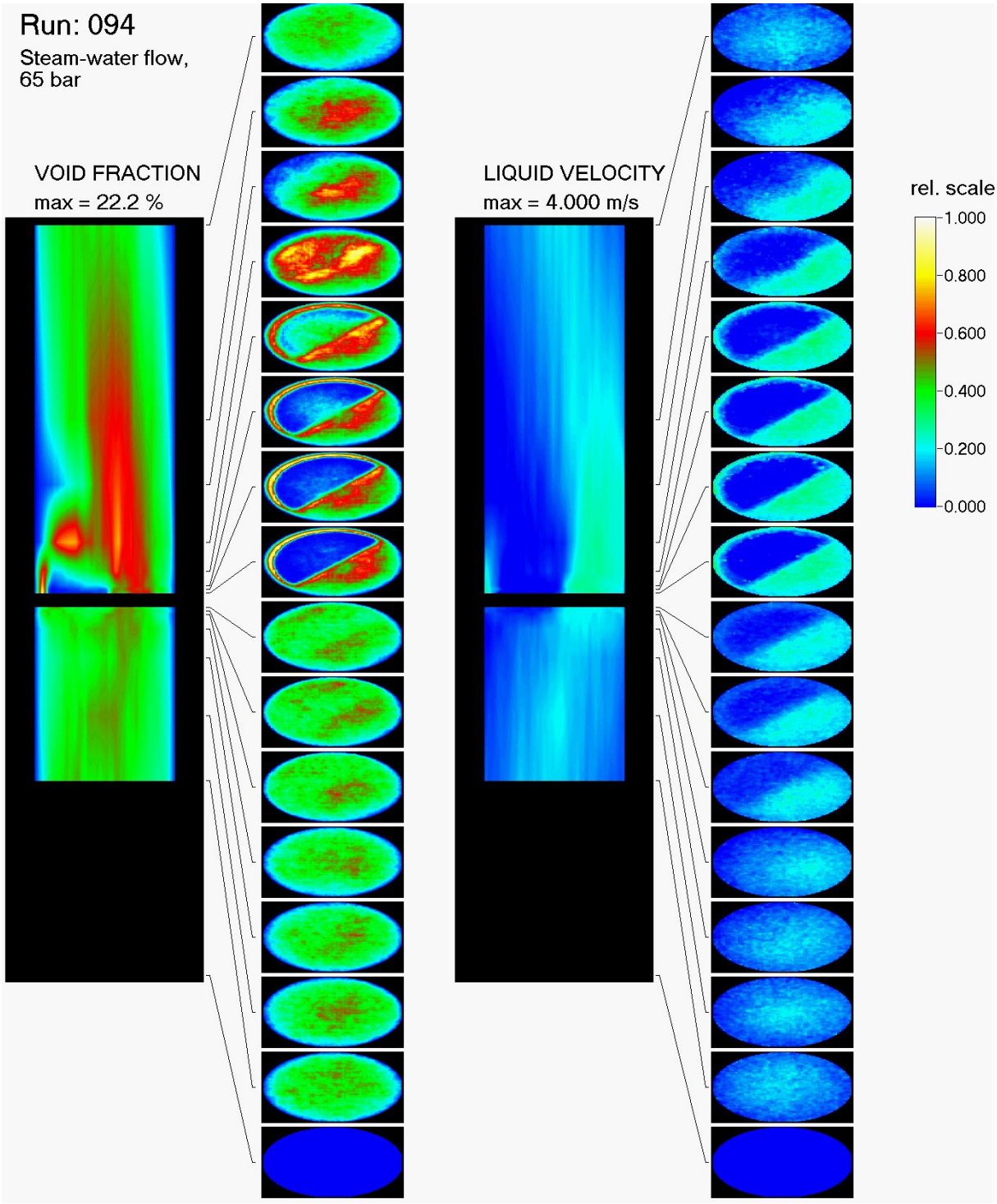

Fig. B.24 Test run 094, J_L = 0.405 m/s, J_G = 0.0898 m/s (at injection position)

Attachment B: Void fraction and liquid velocity distributions

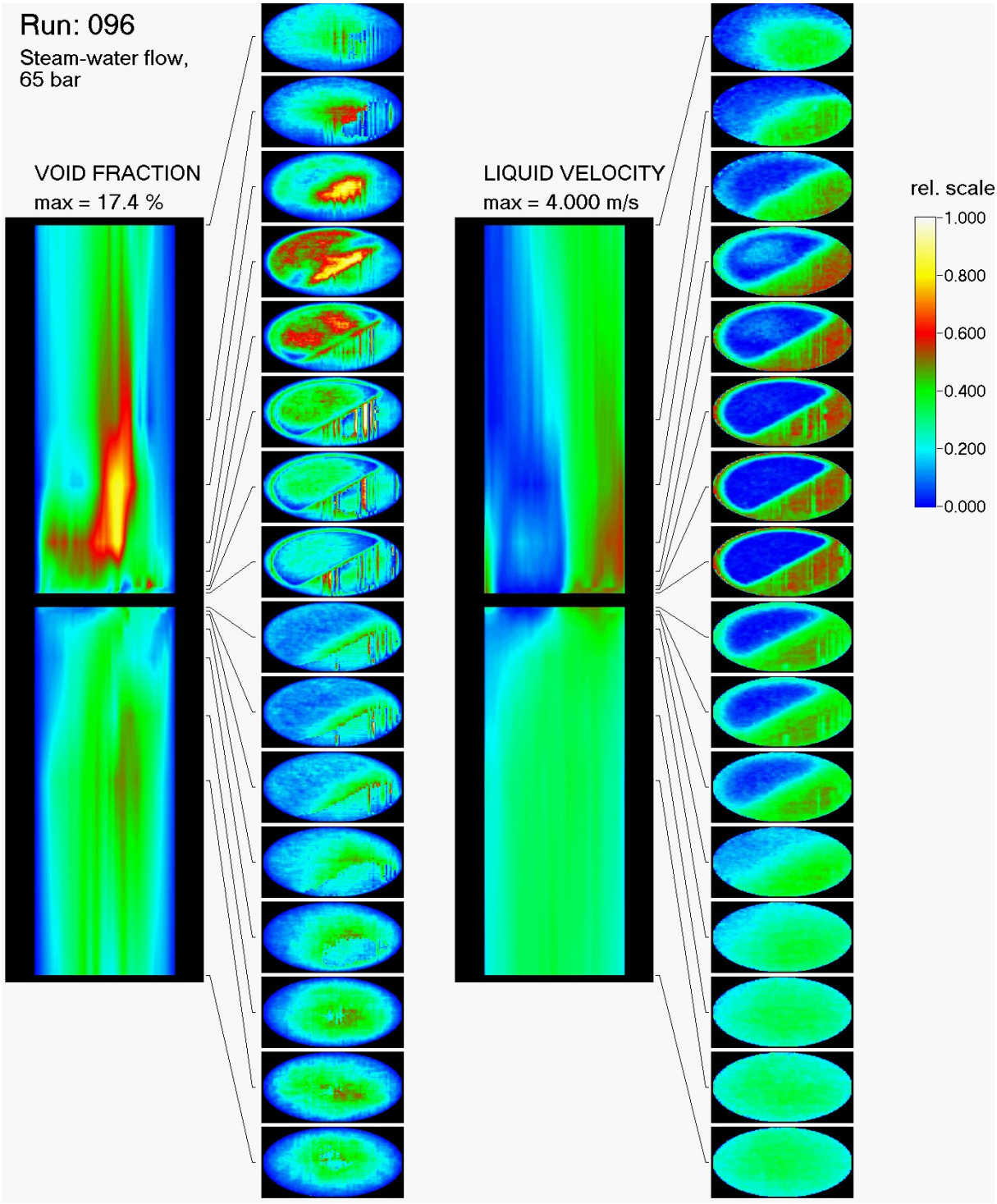

Fig. B.25 Test run 096, J_L = 1.017 m/s, J_G = 0.0898 m/s (at injection position)

Attachment B: Void fraction and liquid velocity distributions

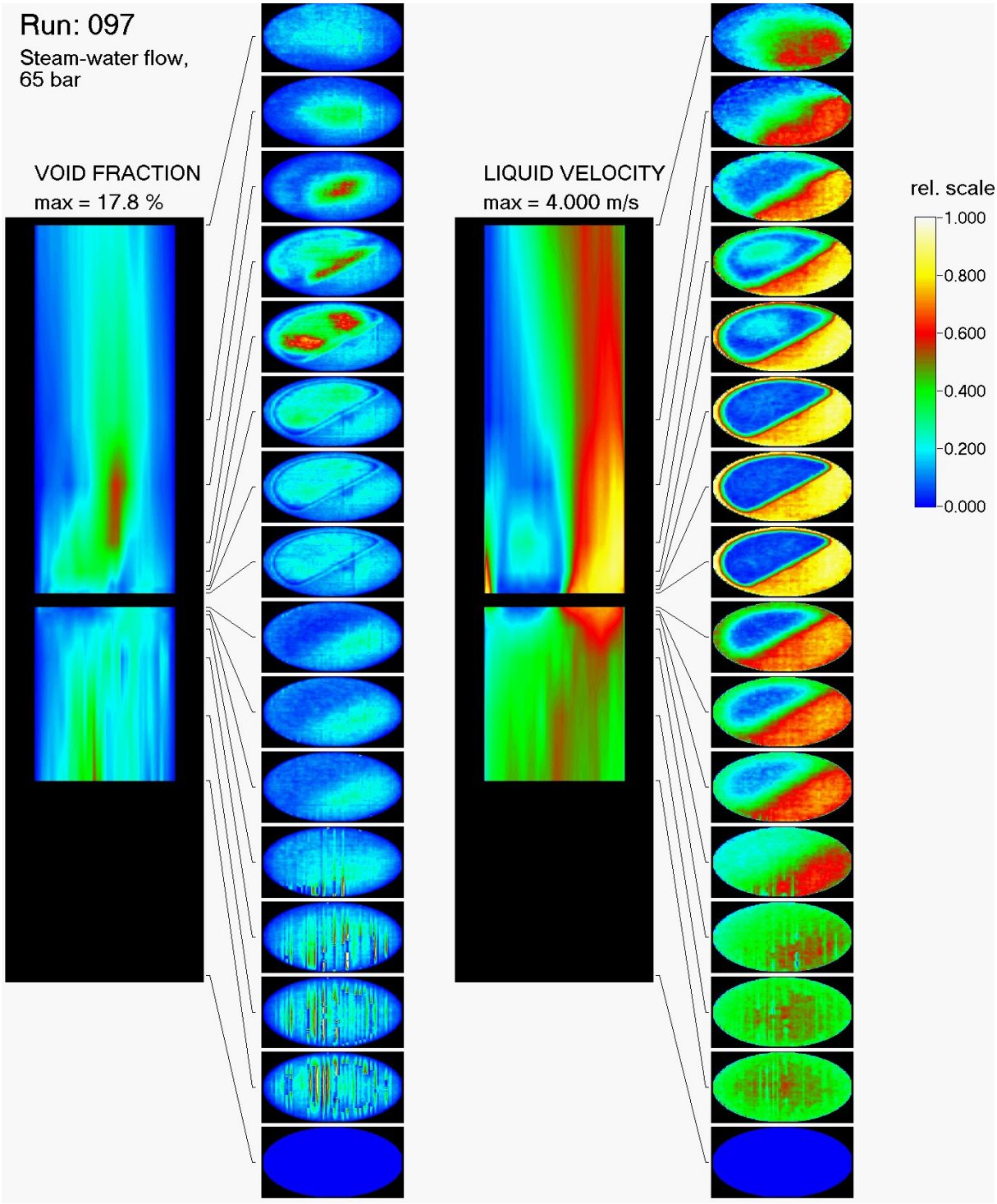

Fig. B.26 Test run 097, J_L = 1.611 m/s, J_G = 0.0898 m/s (at injection position)

Attachment B: Void fraction and liquid velocity distributions

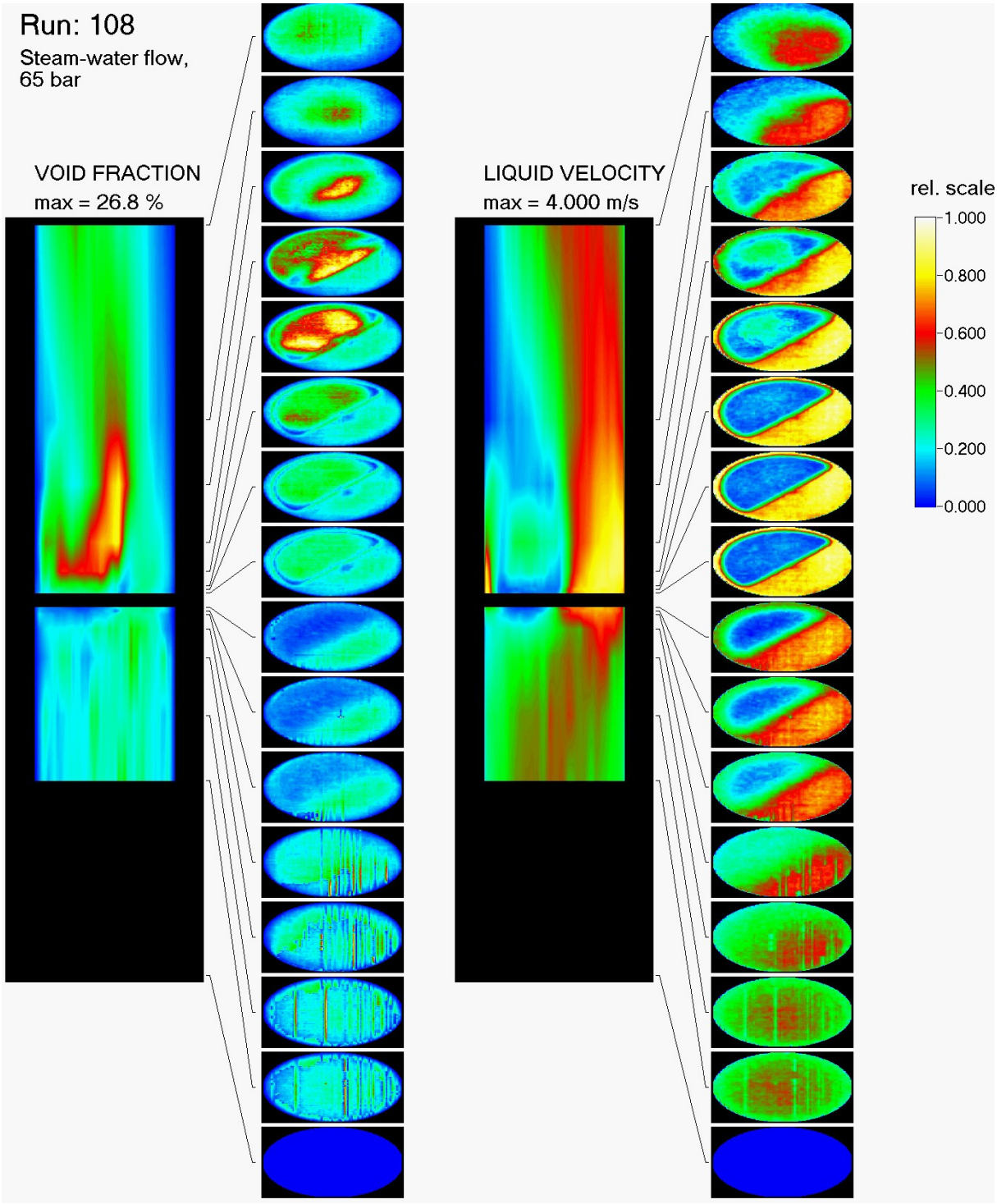

Fig. B.27 Test run 108, J_L = 1.611 m/s, J_G = 0.14 m/s (at injection position)

Attachment B: Void fraction and liquid velocity distributions

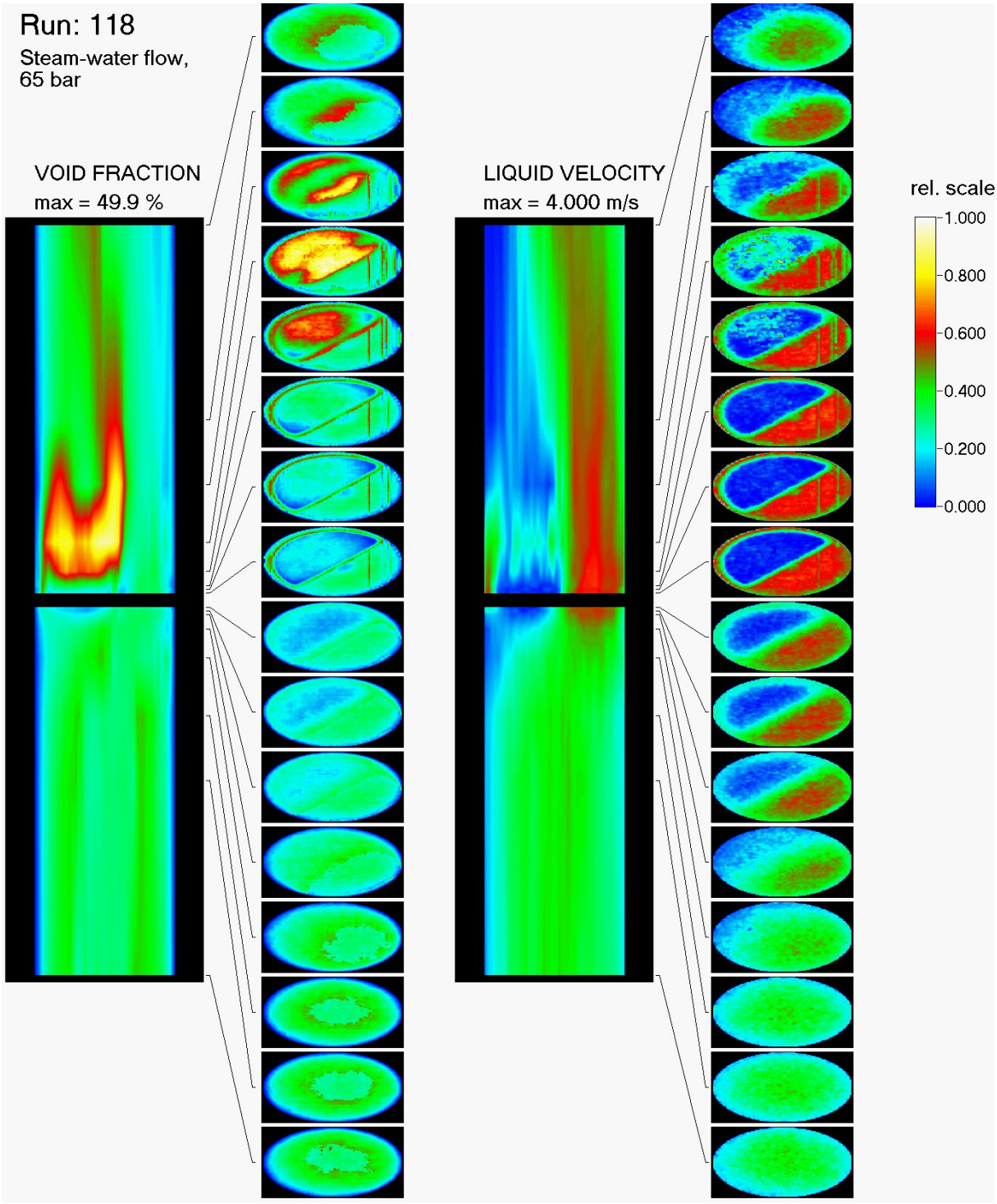

Fig. B.28 Test run 118, J_L = 1.017 m/s, J_G = 0.219 m/s (at injection position)

Attachment B: Void fraction and liquid velocity distributions

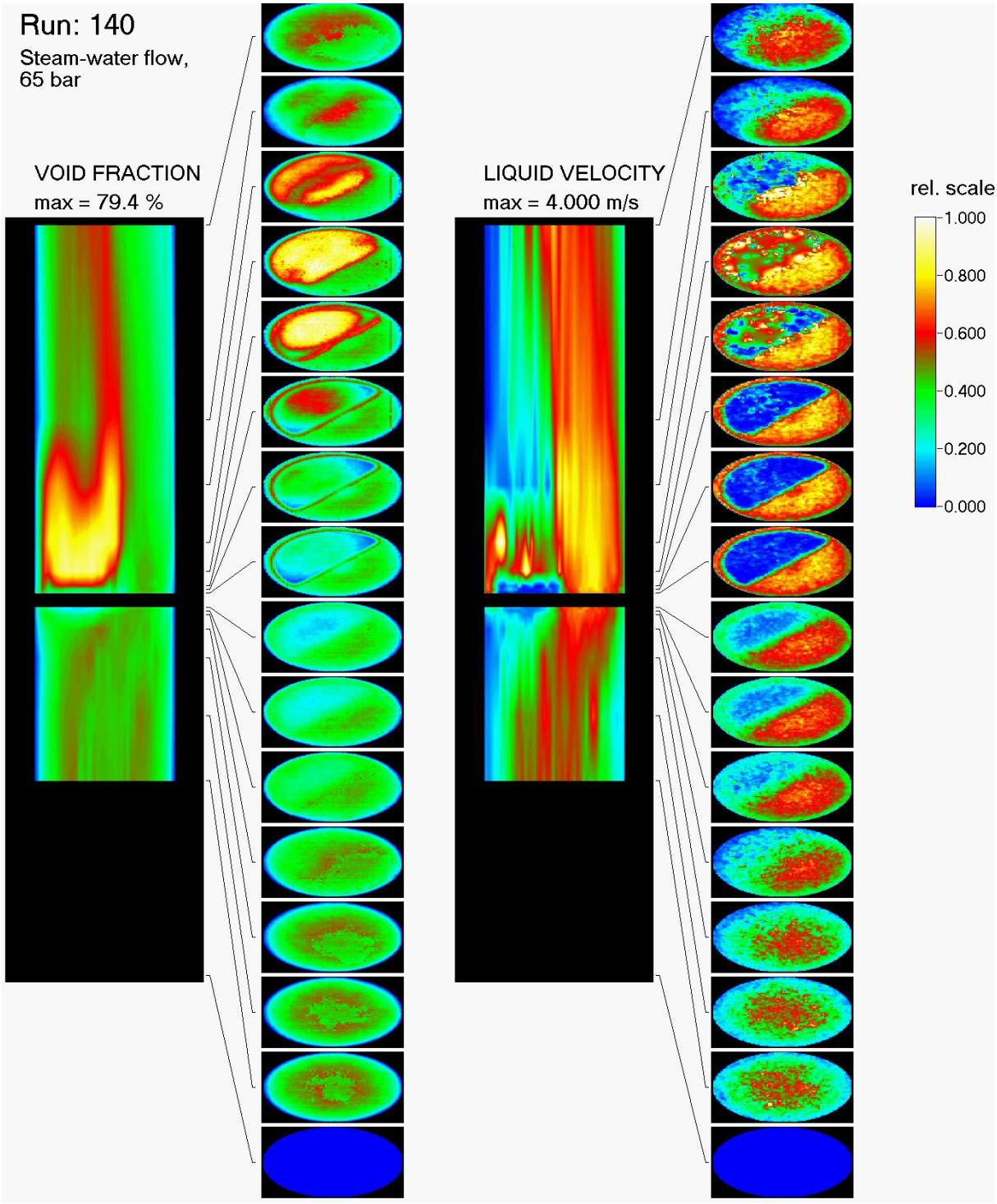

Fig. B.29 Test run 140, J_L = 1.017 m/s, J_G = 0.534 m/s (at injection position)

Attachment B: Void fraction and liquid velocity distributions

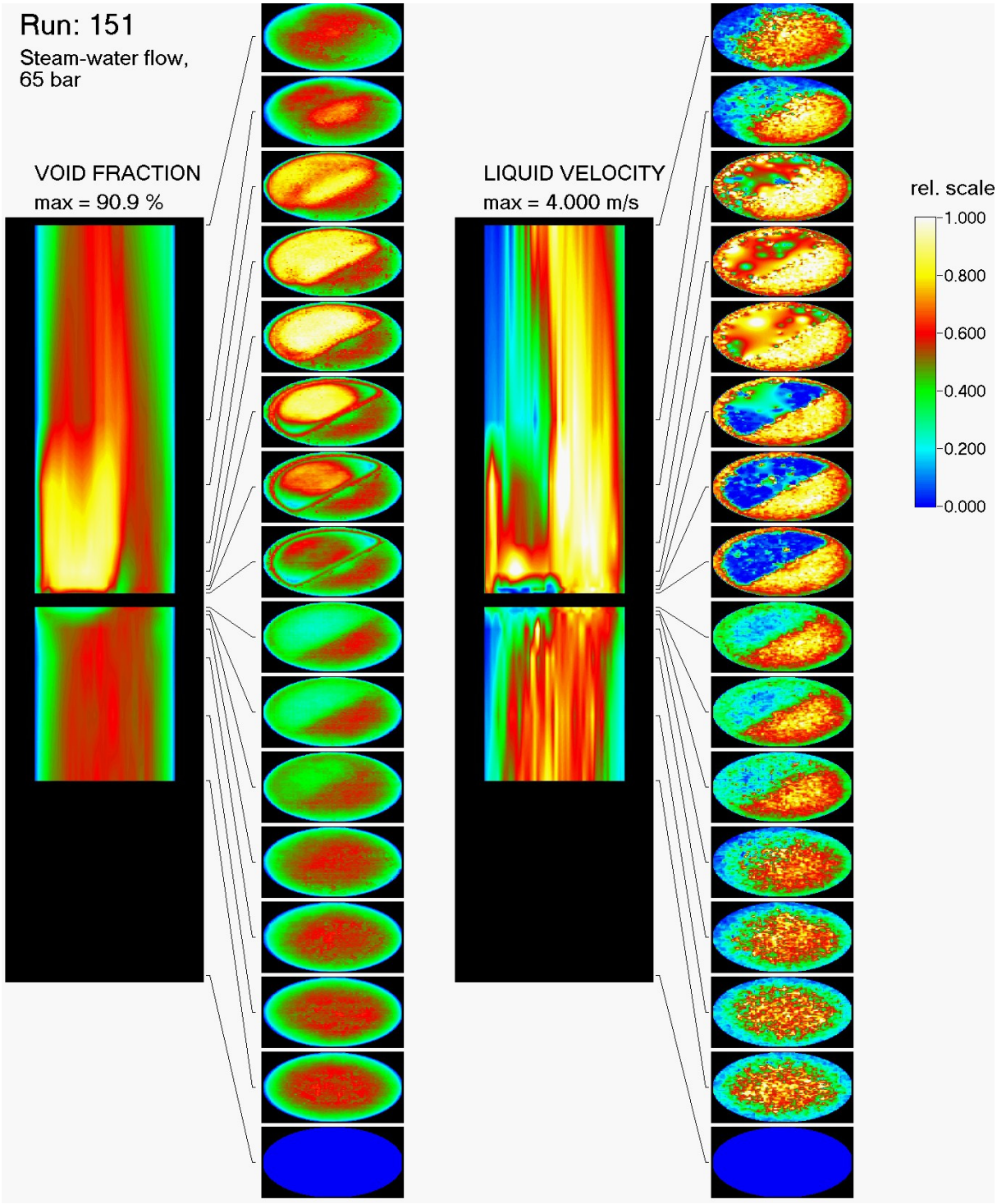

Fig. B.30 Test run 151, J_L = 1.017 m/s, J_G = 0.835 m/s (at injection position)

Attachment C: Void fraction distributions decomposed in bubble-size classes

C.1 Time averaged void fraction distributions decomposed in bubble-size classes up- and downstream of the obstacle for air-water and steam-water test runs

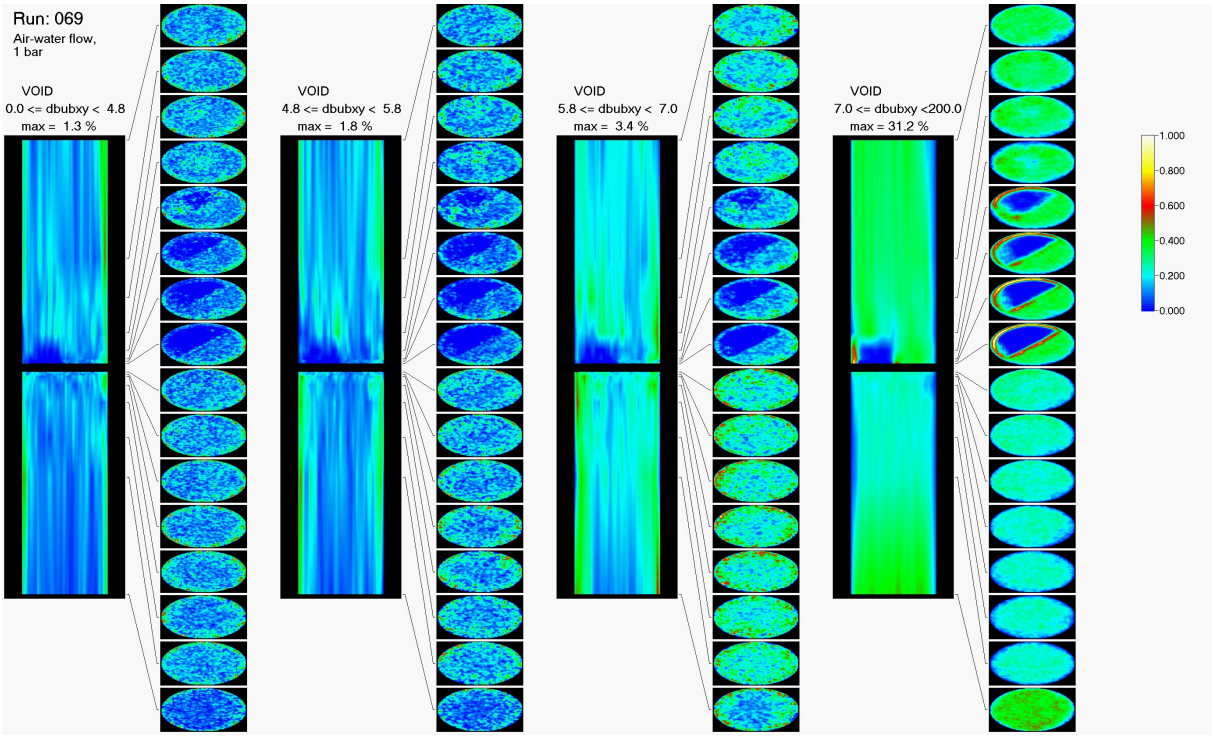

Fig. C.1 Air-water test run 069, J_L = 0.102 m/s, J_G = 0.0368 m/s (at injection position)

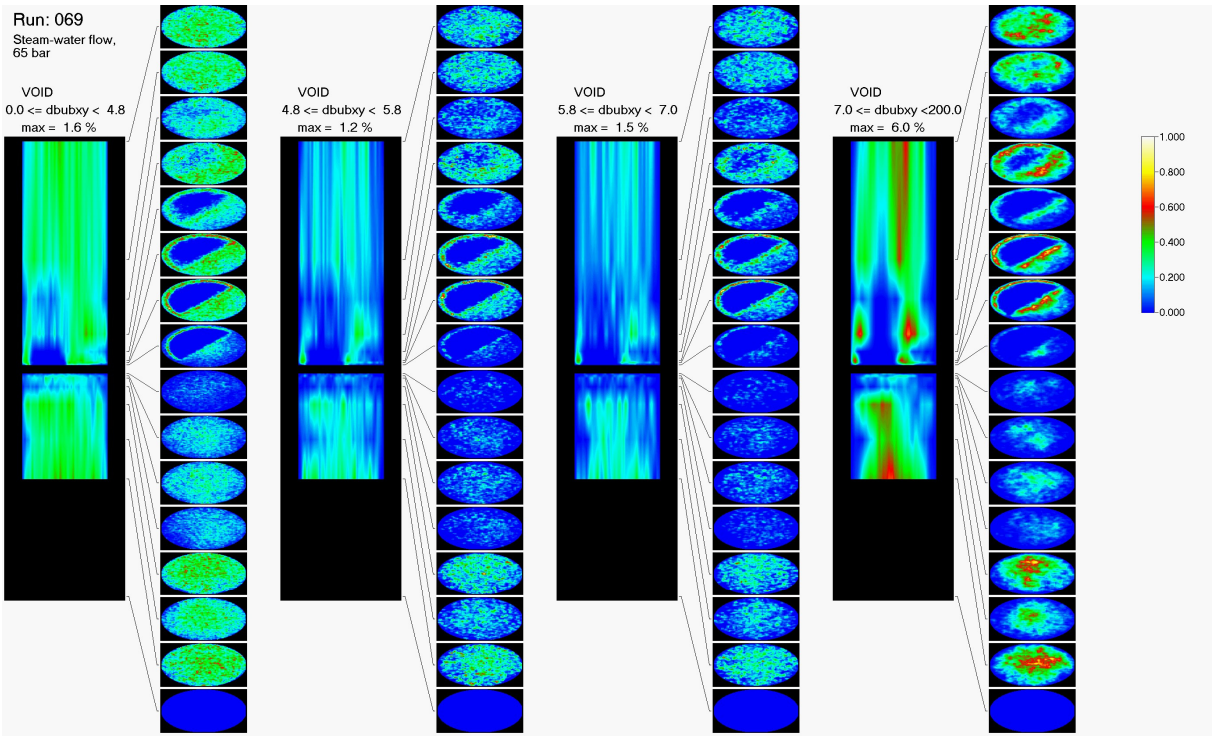

Fig. C.2 Steam-water test run 069, J_L = 0.102 m/s, J_G = 0.0368 m/s (at injection position)

Attachment C: Void fraction distributions decomposed in bubble-size classes

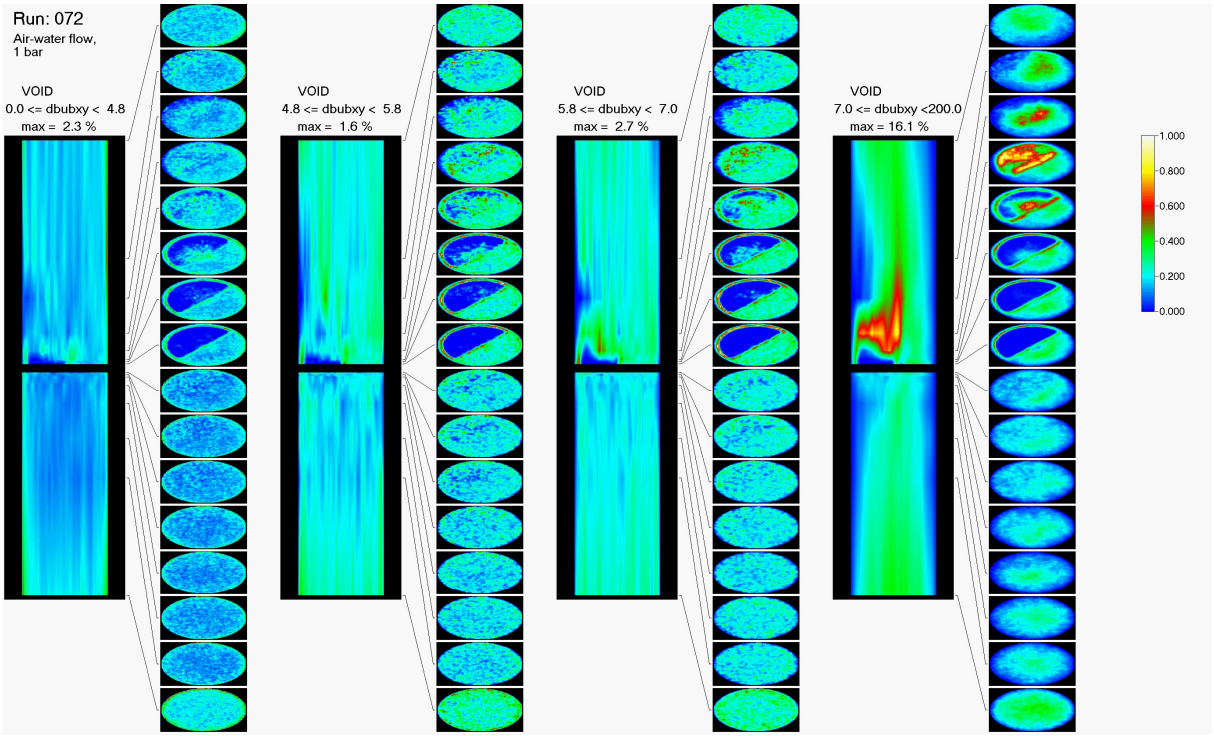

Fig. C.3 Air-water test run 072, J_L = 0.405 m/s, J_G = 0.0368 m/s (at injection position)

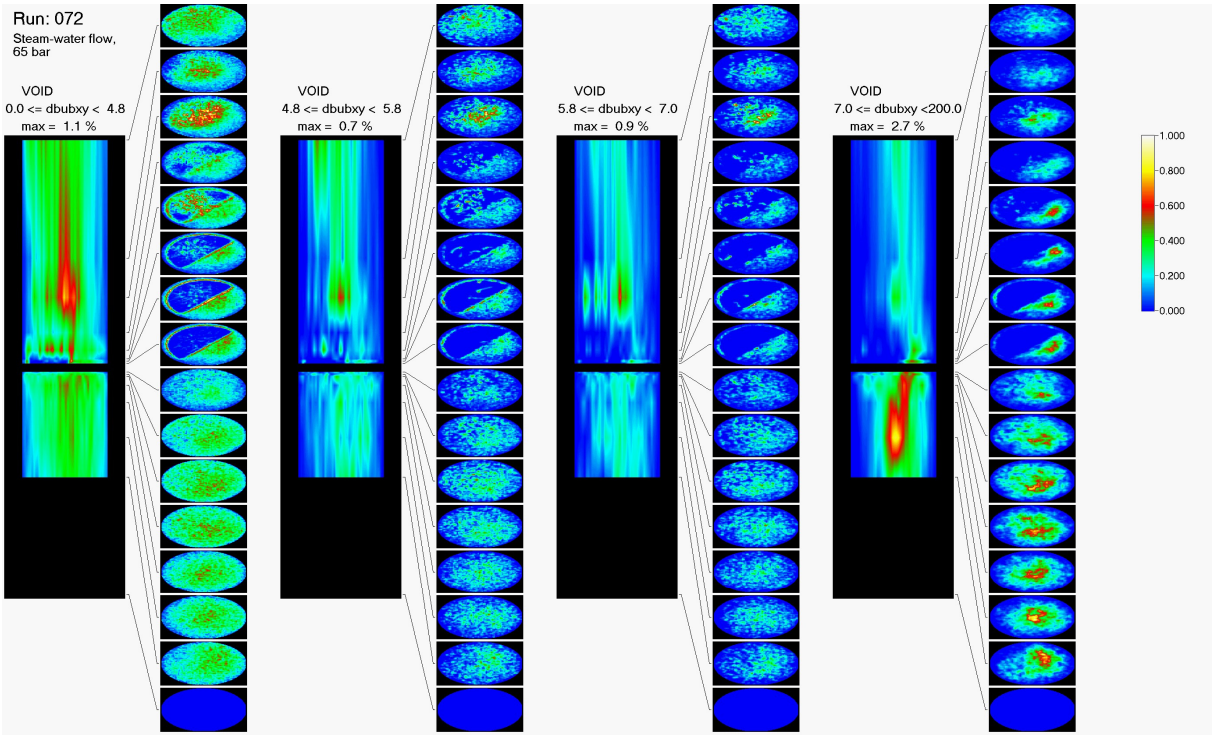

Fig. C.4 Steam-water test run 072, J_L = 0.405 m/s, J_G = 0.0368 m/s (at injection position)

Attachment C: Void fraction distributions decomposed in bubble-size classes

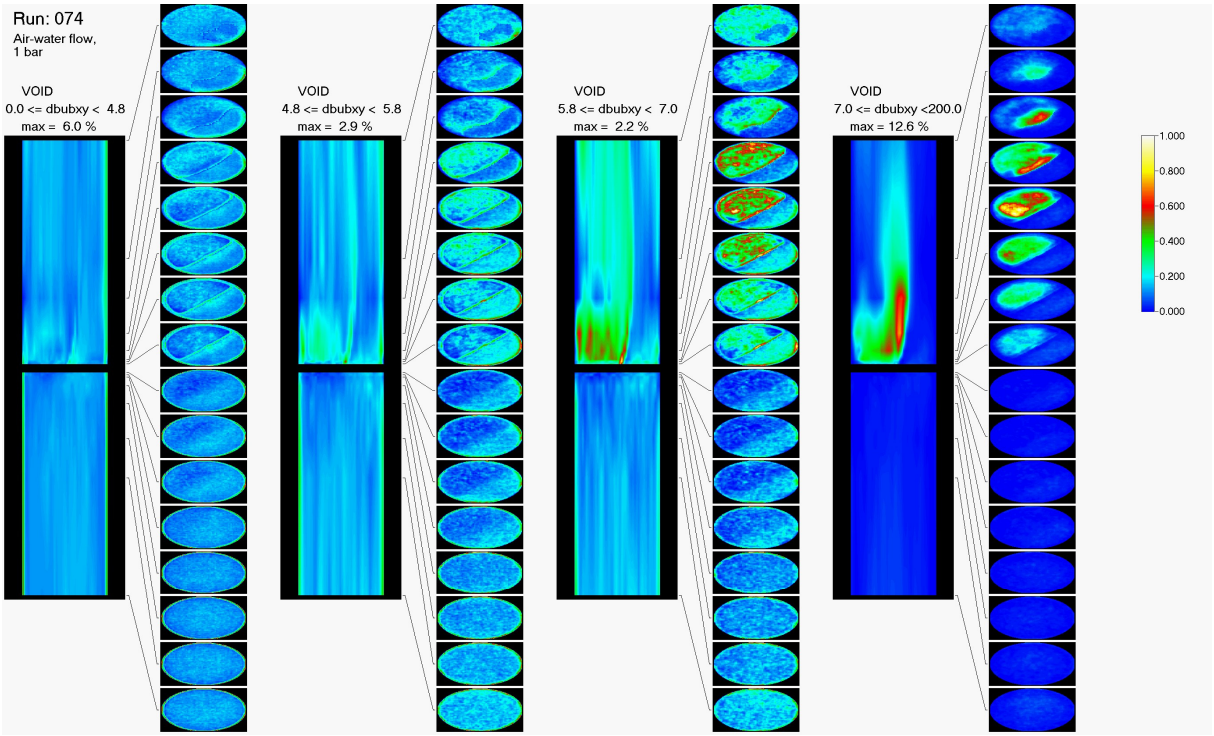

Fig. C.5 Air-water test run 074, J_L = 1.017 m/s, J_G = 0.0368 m/s (at injection position)

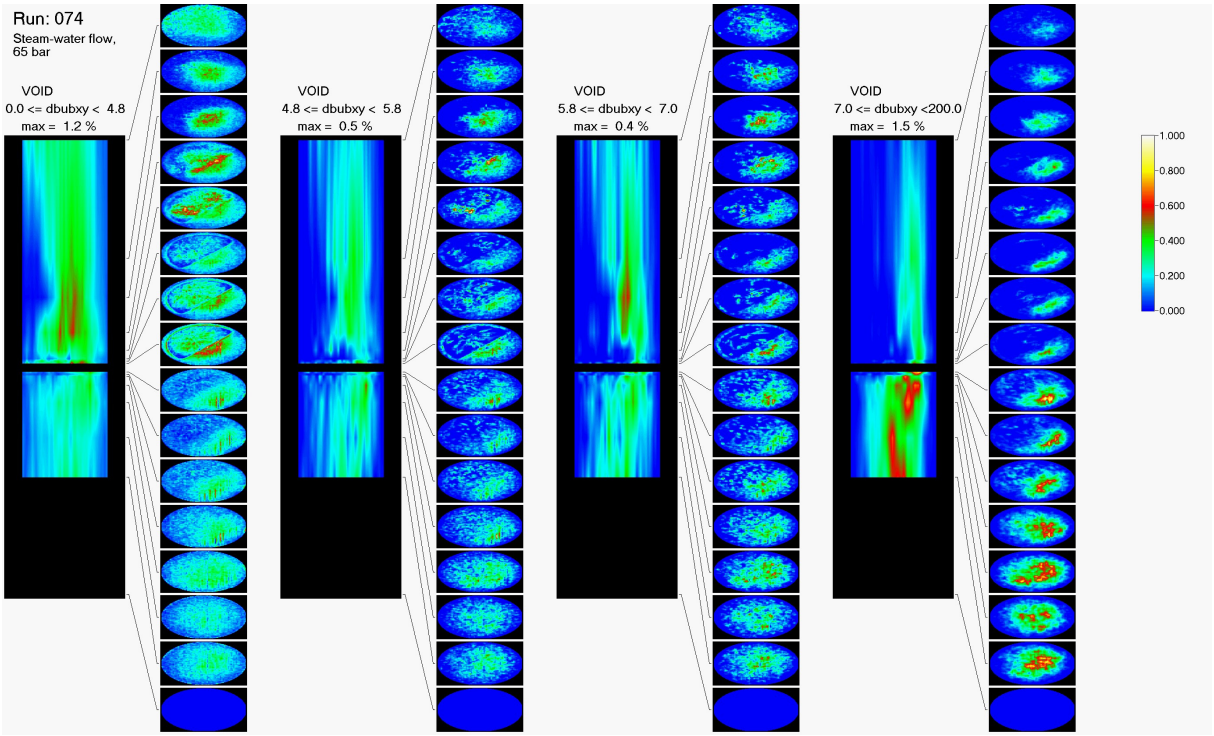

Fig. C.6 Steam-water test run 074, J_L = 1.017 m/s, J_G = 0.0368 m/s (at injection position)

Attachment C: Void fraction distributions decomposed in bubble-size classes

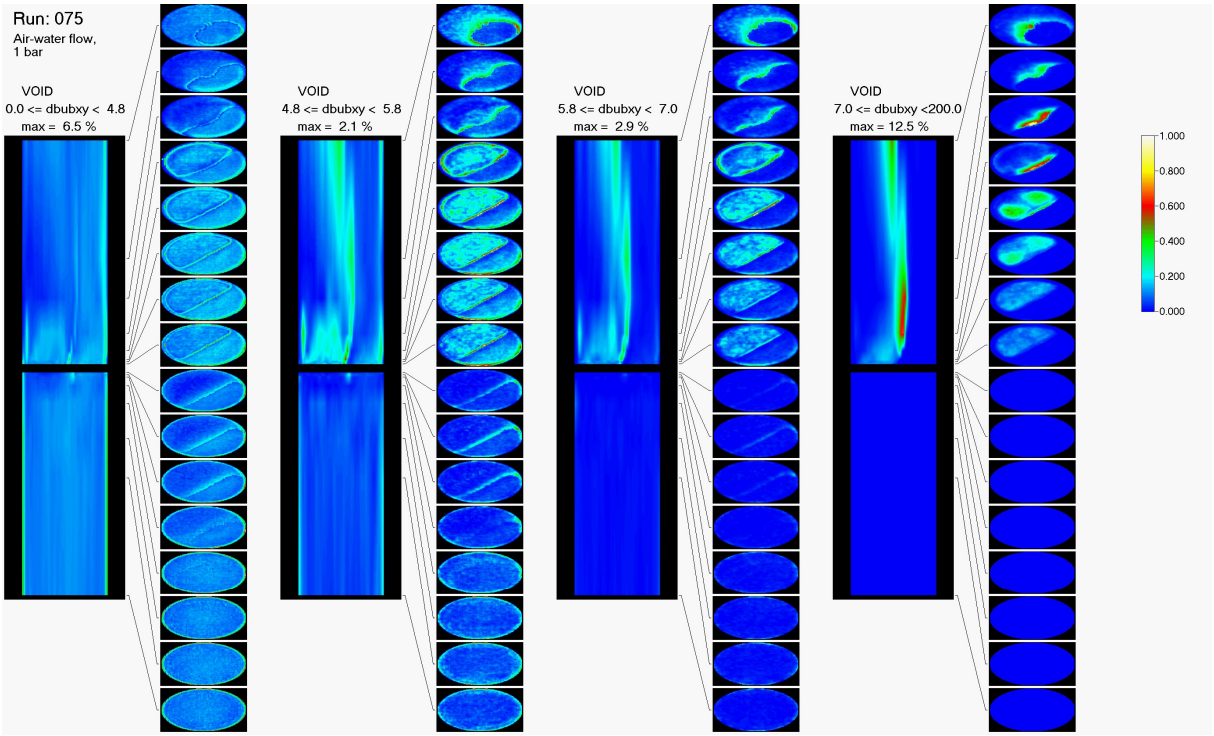

Fig. C.7 Air-water test run 075, J_L = 1.611 m/s, J_G = 0.0368 m/s (at injection position)

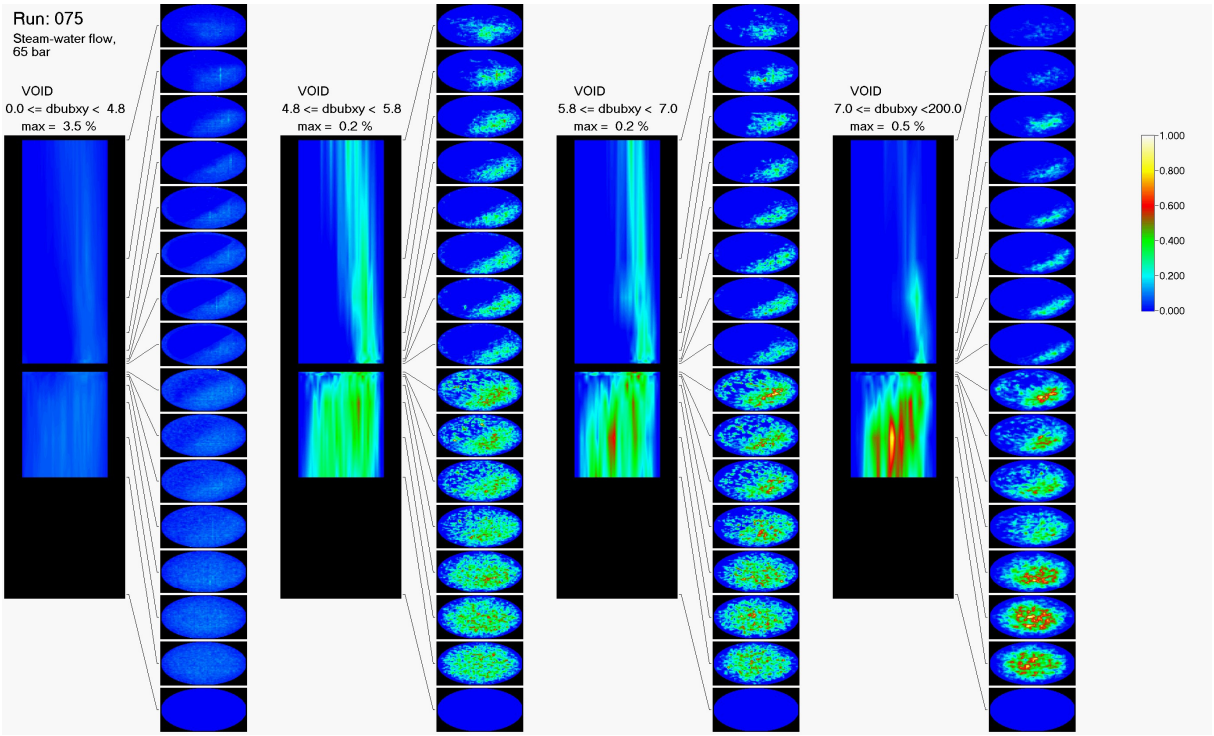

Fig. C.8 Steam-water test run 075, J_L = 1.611 m/s, J_G = 0.0368 m/s (at injection position)

Attachment C: Void fraction distributions decomposed in bubble-size classes

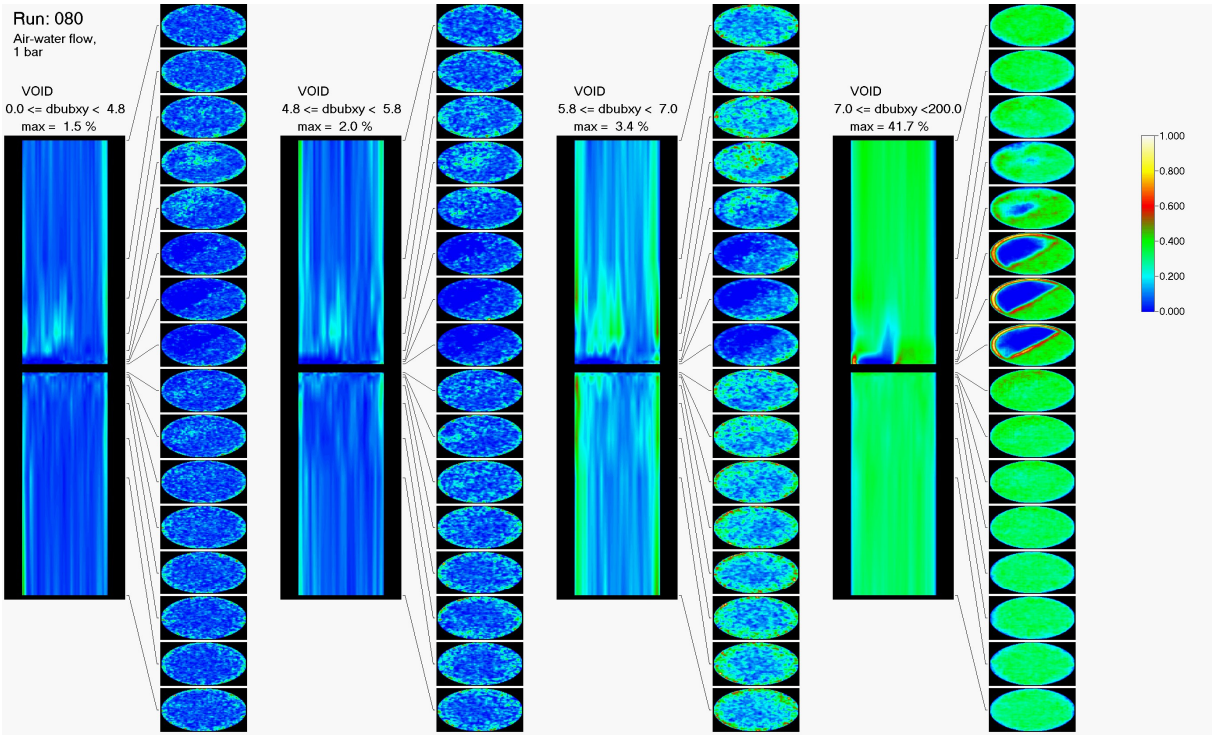

Fig. C.9 Air-water test run 080, J_L = 0.102 m/s, J_G = 0.0574 m/s (at injection position)

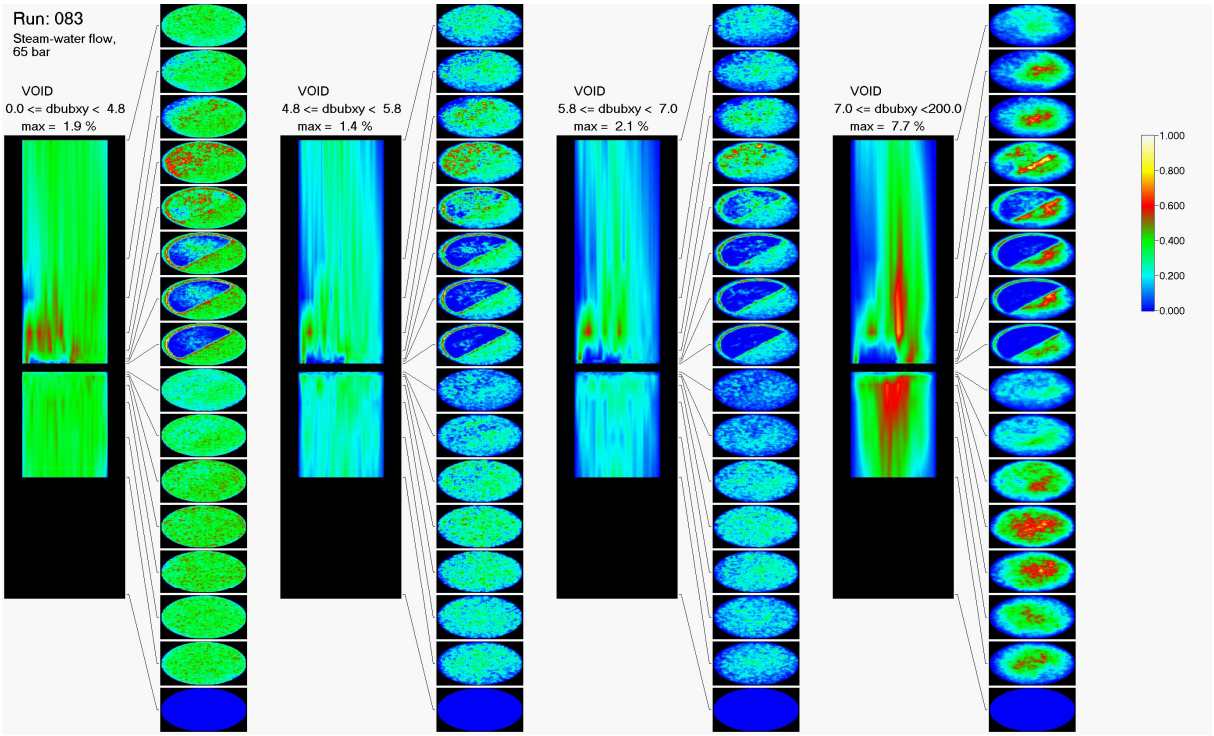

Fig. C.10 Steam-water test run 080, J_L = 0.102 m/s, J_G = 0.0574 m/s (at injection position)

Attachment C: Void fraction distributions decomposed in bubble-size classes

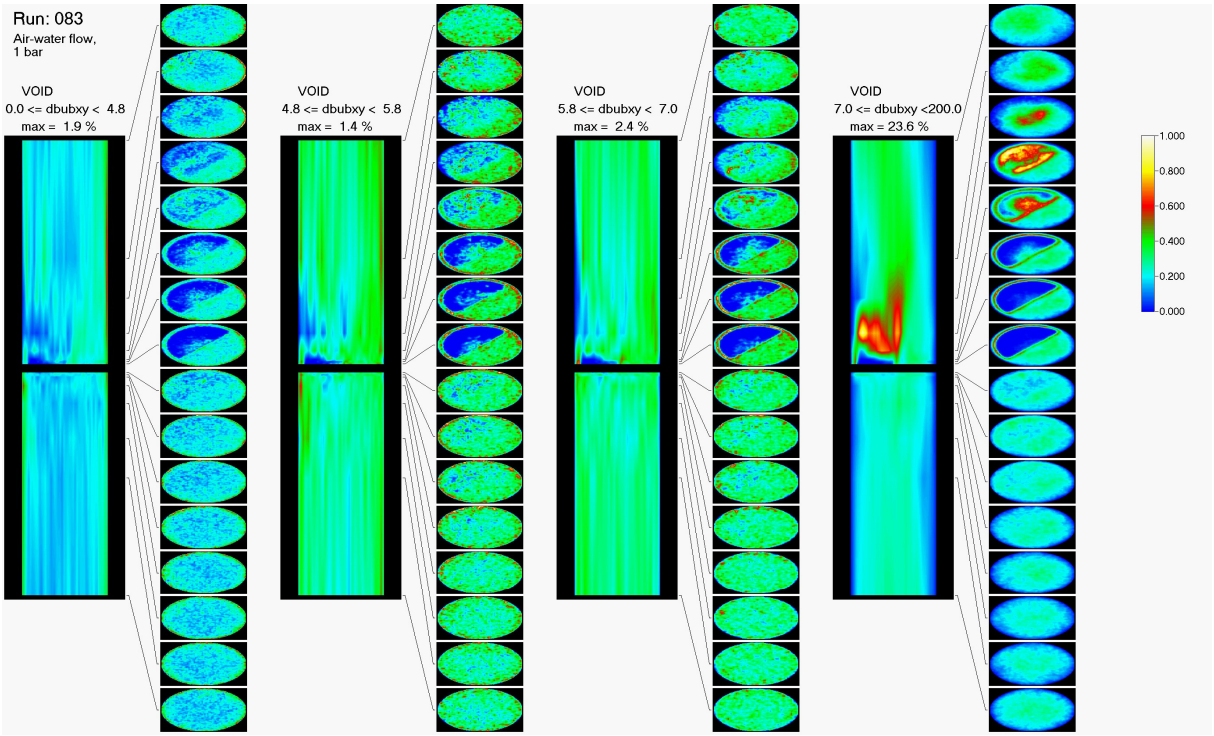

Fig. C.11 Air-water test run 083, J_L = 0.405 m/s, J_G = 0.0574 m/s (at injection position)

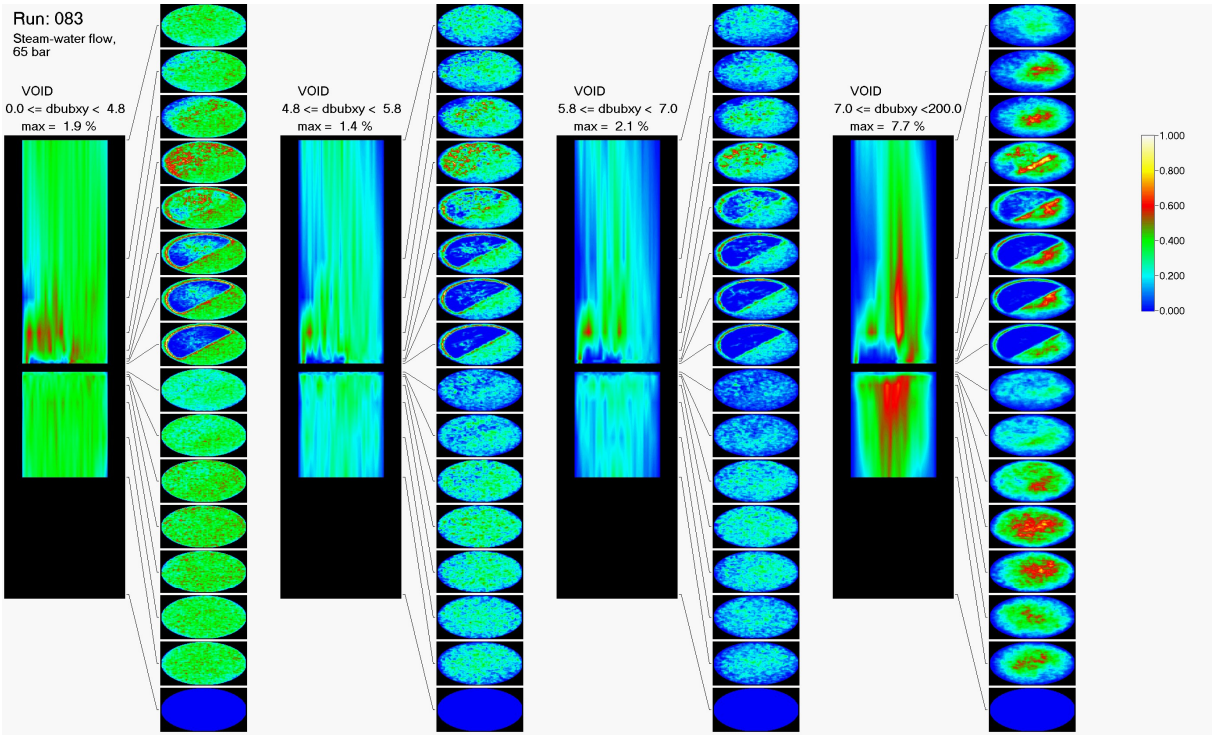

Fig. C.12 Steam-water test run 083, J_L = 0.405 m/s, J_G = 0.0574 m/s (at injection position)

Attachment C: Void fraction distributions decomposed in bubble-size classes

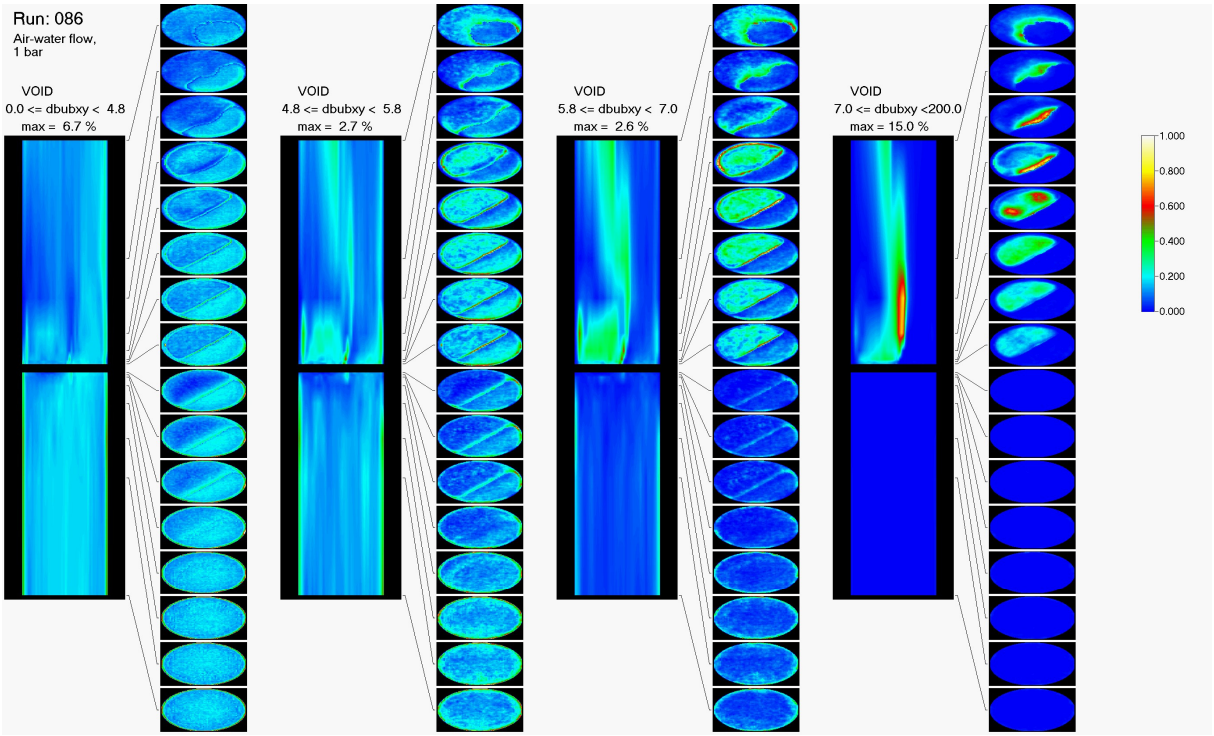

Fig. C.13 Air-water test run 086, J_L = 1.611 m/s, J_G = 0.0574 m/s (at injection position)

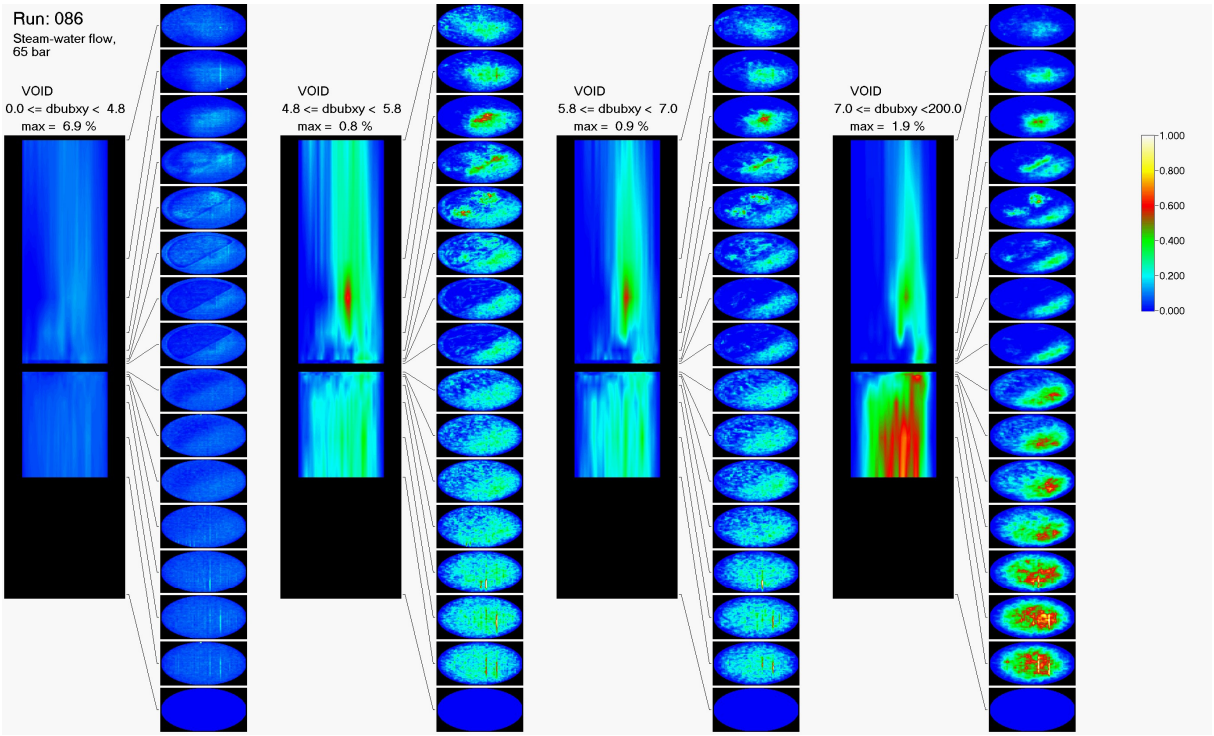

Fig. C.14 Steam-water test run 086, J_L = 1.611 m/s, J_G = 0.0574 m/s (at injection position)

Attachment C: Void fraction distributions decomposed in bubble-size classes

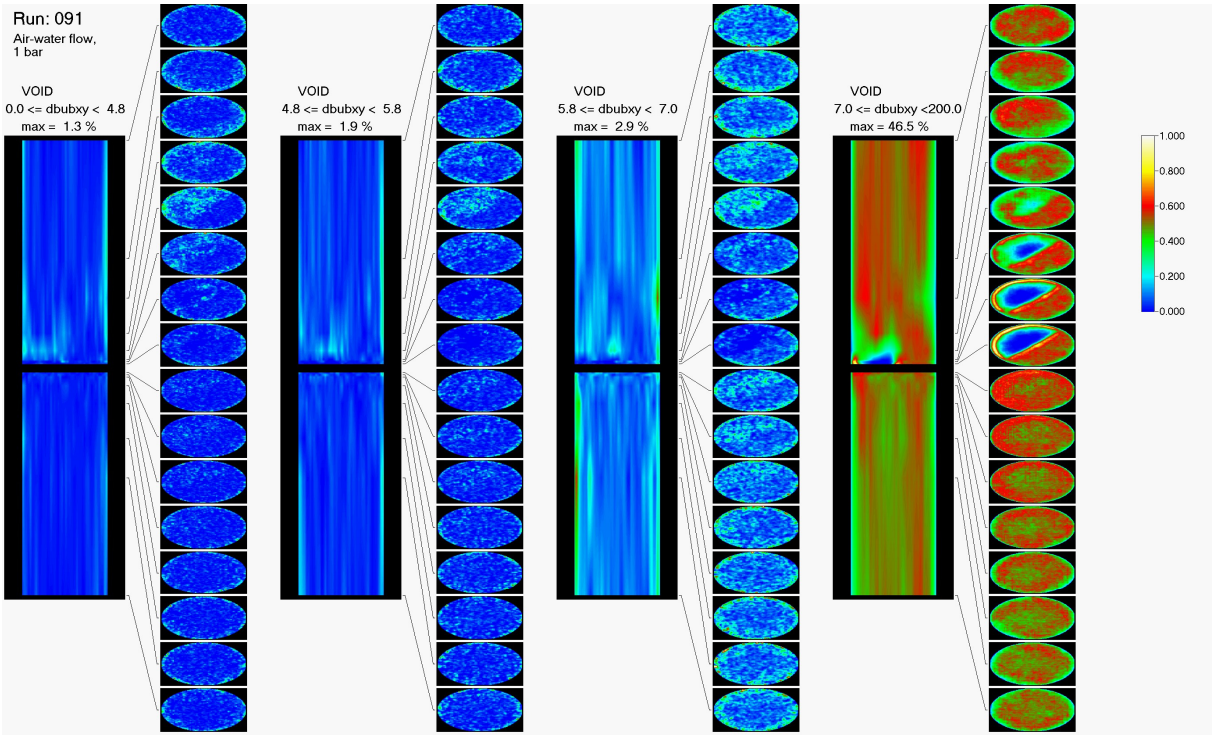

Fig. C.15 Air-water test run 091, J_L = 0.102 m/s, J_G = 0.0898 m/s (at injection position)

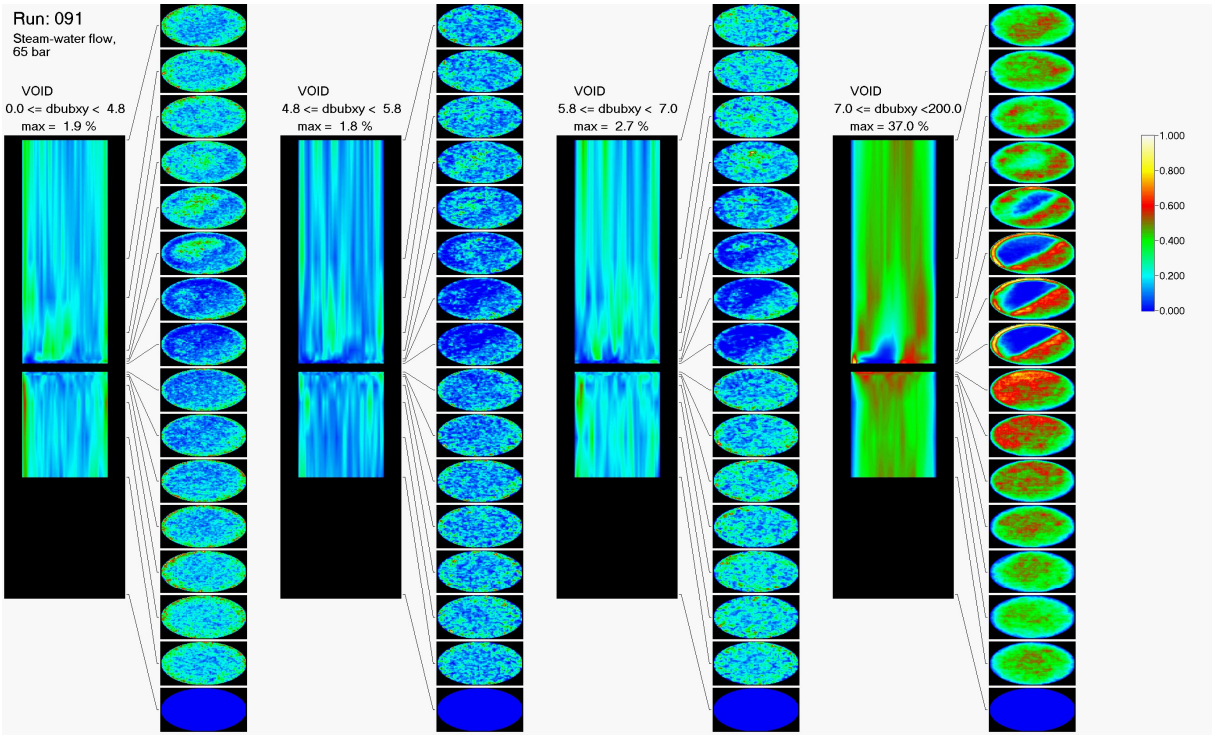

Fig. C.16 Steam-water test run 091, J_L = 0.102 m/s, J_G = 0.0898 m/s (at injection position)

Attachment C: Void fraction distributions decomposed in bubble-size classes

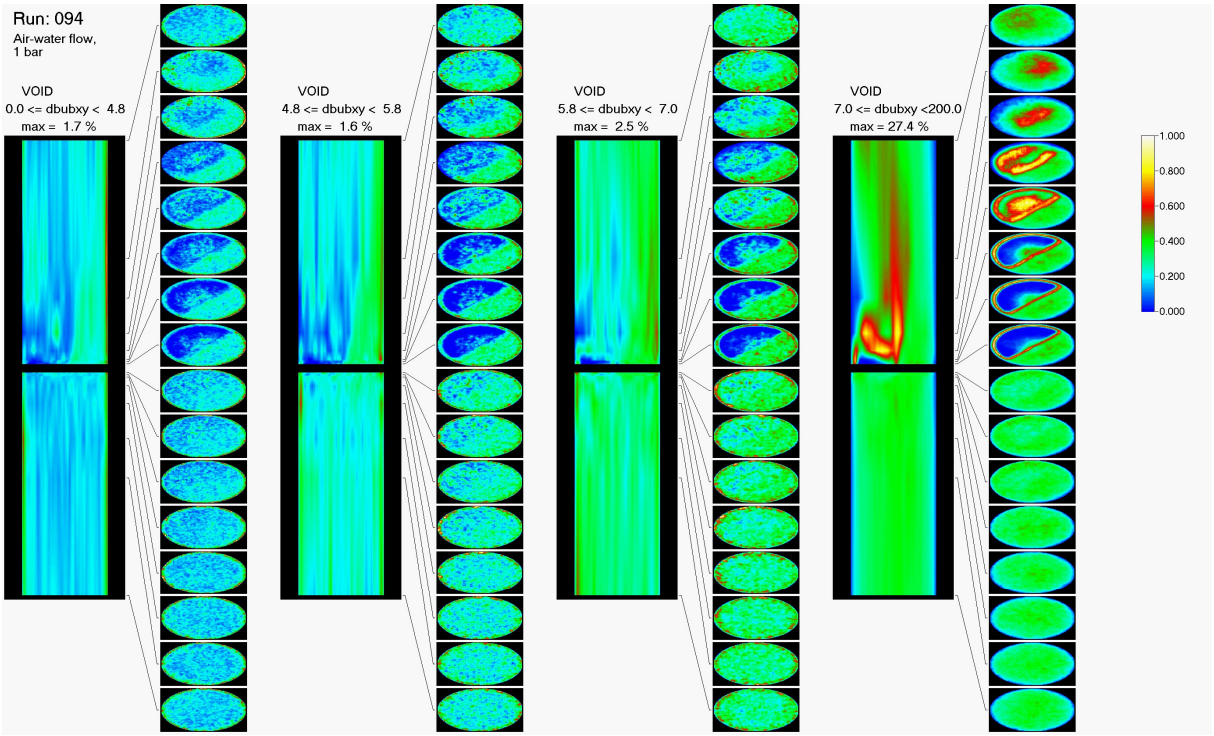

Fig. C.17 Air-water test run 094, J_L = 0.405 m/s, J_G = 0.0898 m/s (at injection position)

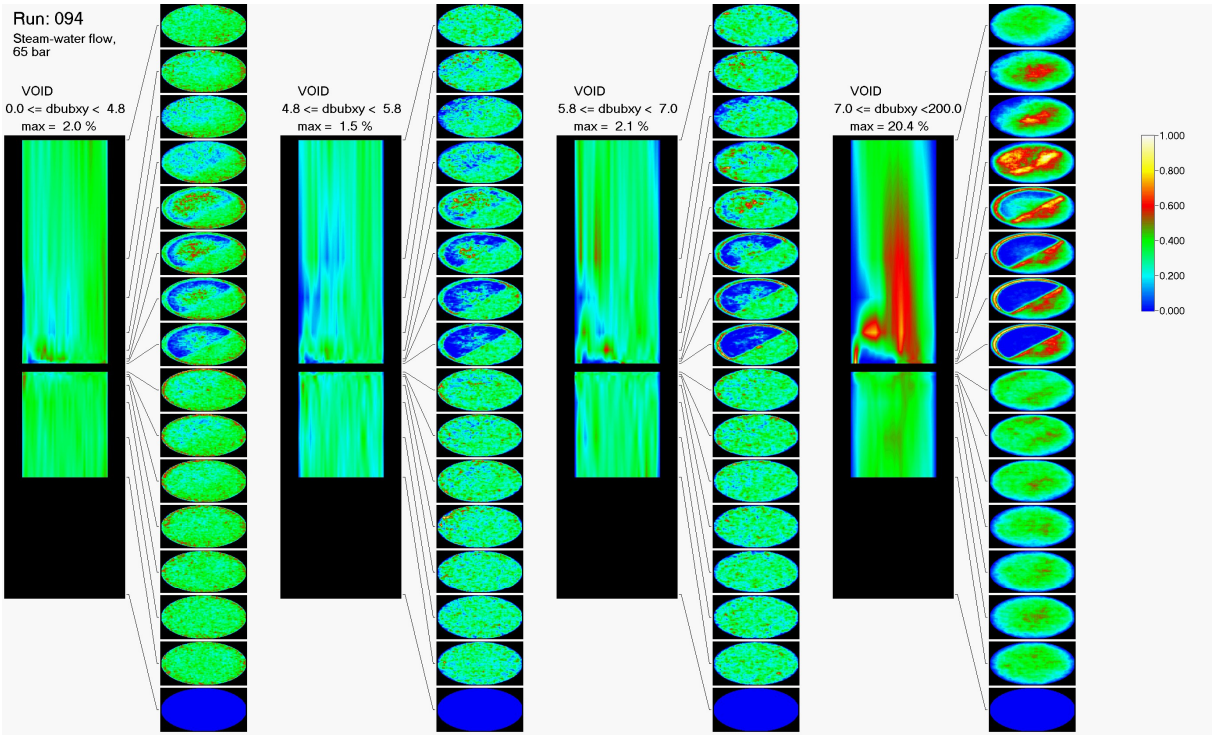

Fig. C.18 Steam-water test run 094, J_L = 0.405 m/s, J_G = 0.0898 m/s (at injection position)

Attachment C: Void fraction distributions decomposed in bubble-size classes

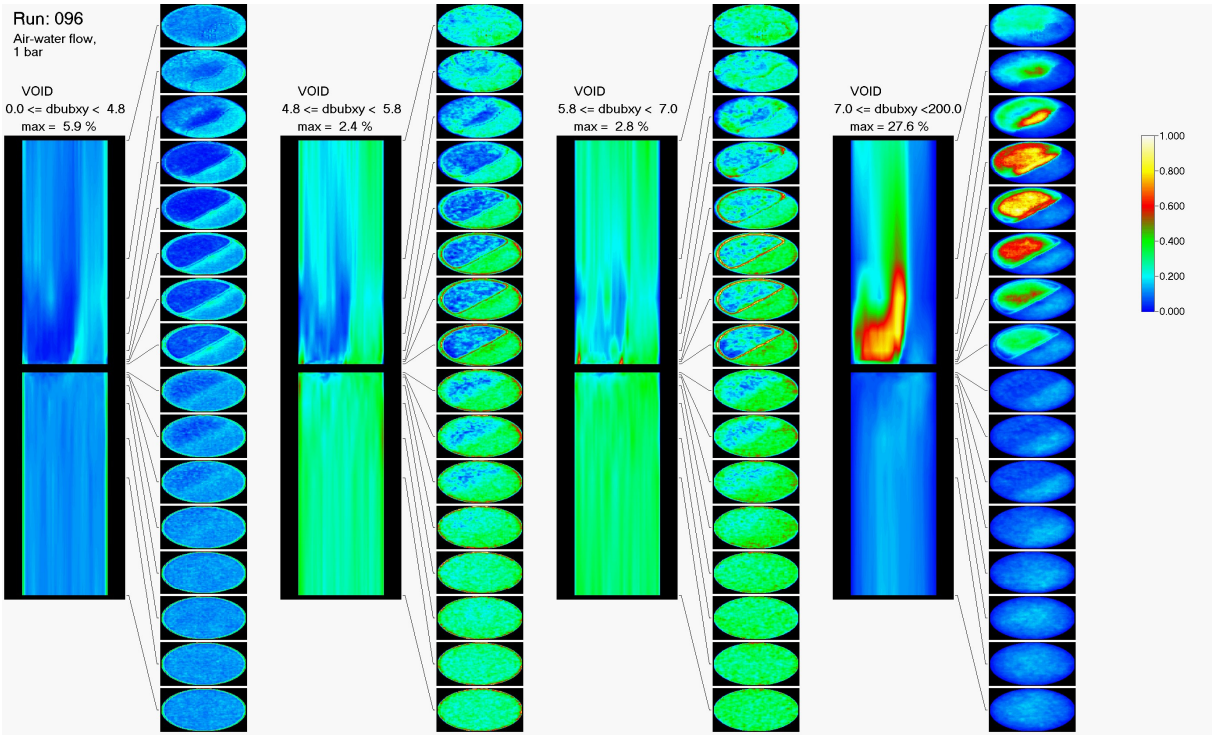

Fig. C.19 Air-water test run 096, J_L = 1.017 m/s, J_G = 0.0898 m/s (at injection position)

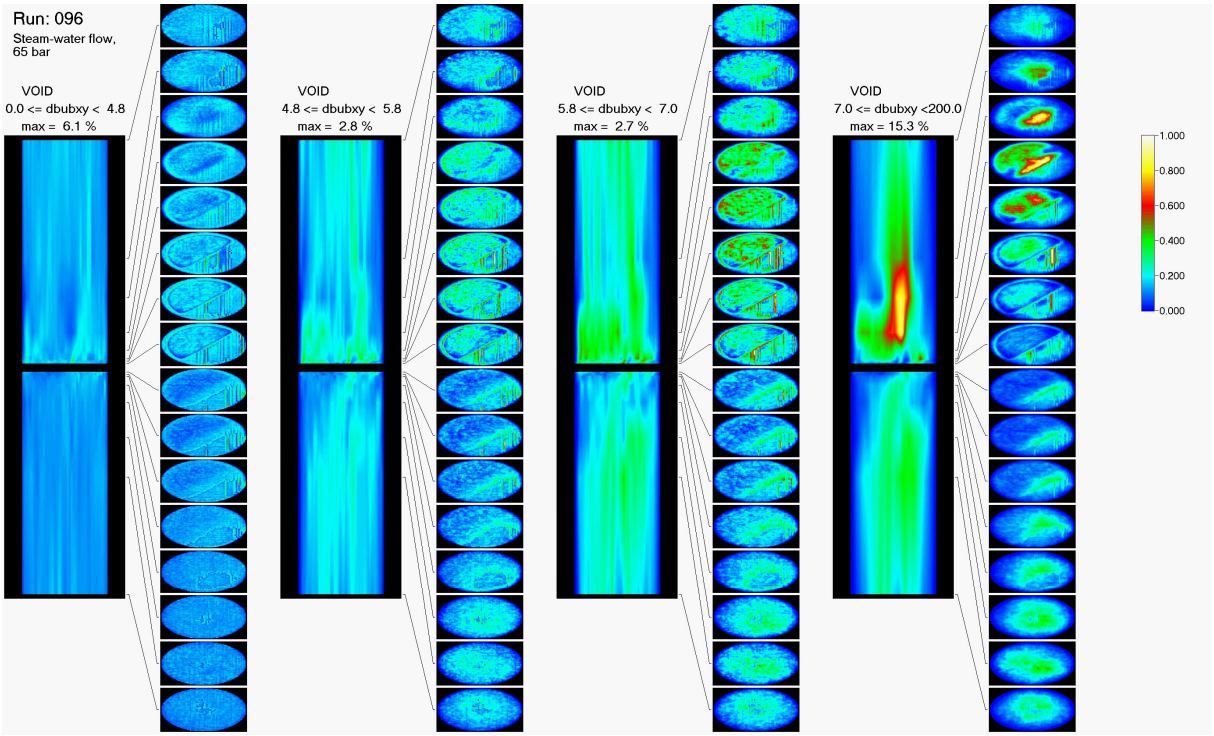

Fig. C.20 Steam-water test run 096, J_L = 1.017 m/s, J_G = 0.0898 m/s (at injection position)

Attachment C: Void fraction distributions decomposed in bubble-size classes

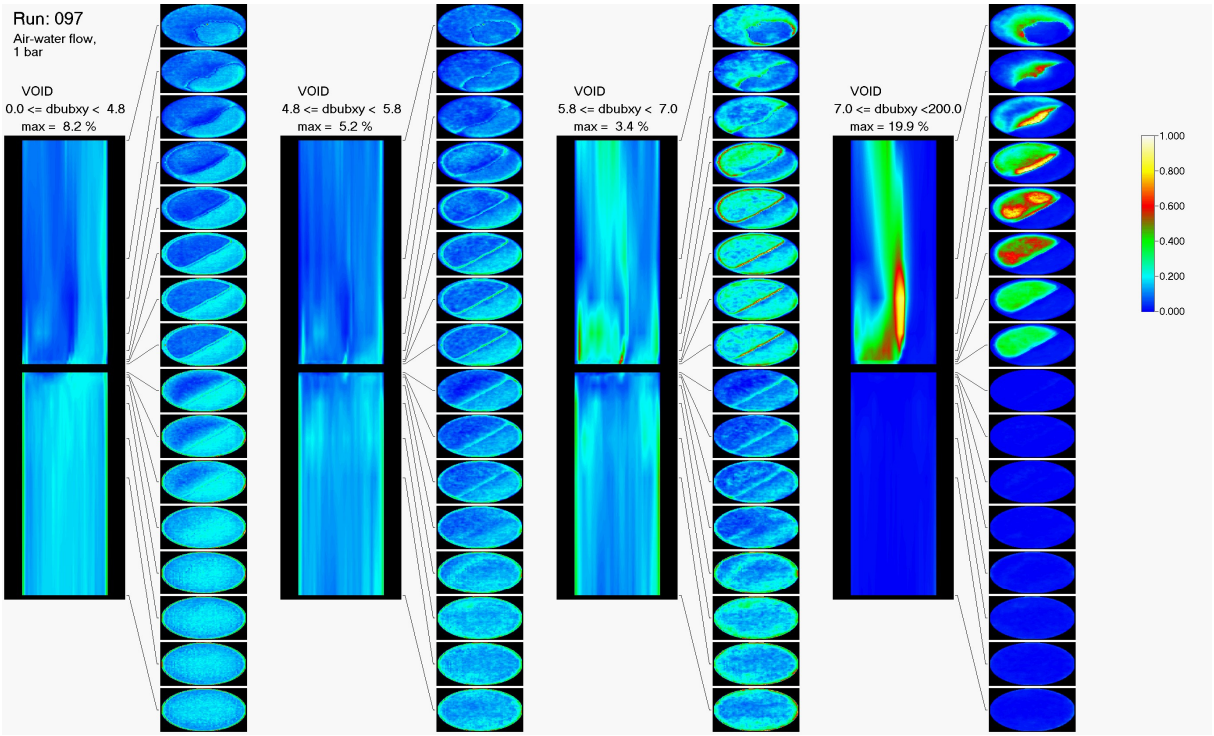

Fig. C.21 Air-water test run 097, J_L = 1.611 m/s, J_G = 0.0898 m/s (at injection position)

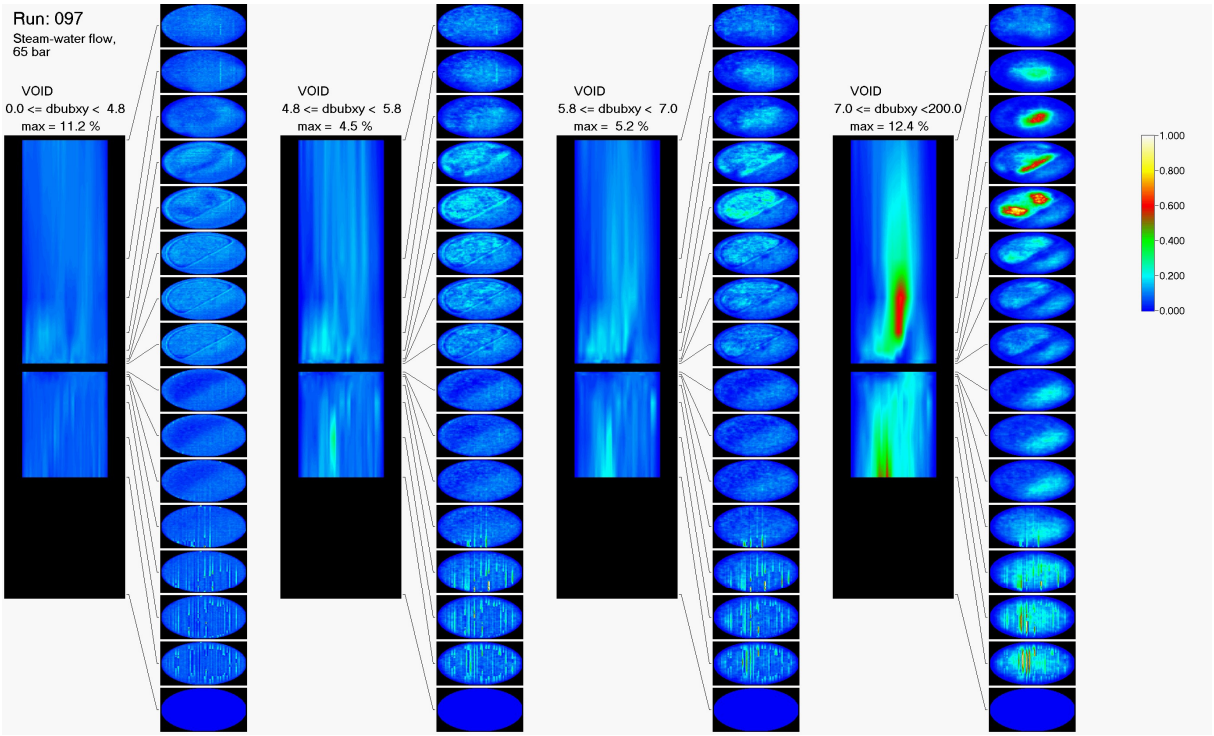

Fig. C.22 Steam-water test run 097, J_L = 1.611 m/s, J_G = 0.0898 m/s (at injection position)

Attachment C: Void fraction distributions decomposed in bubble-size classes

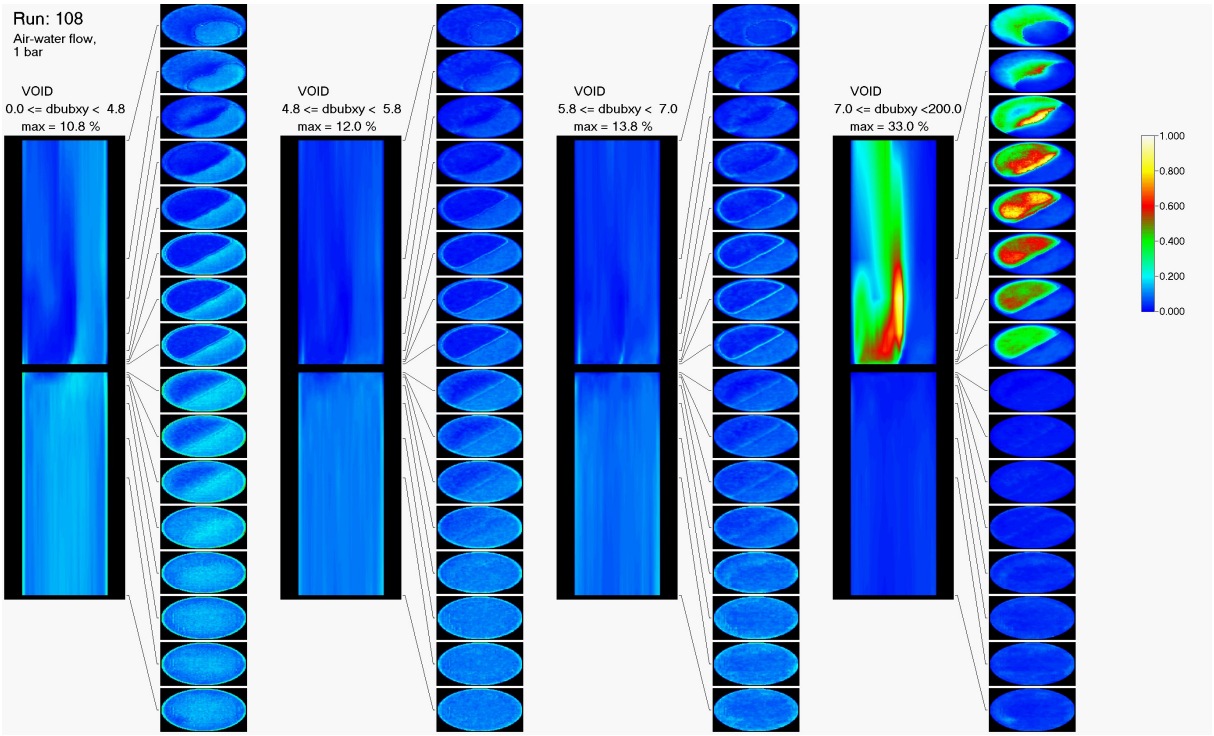

Fig. C.23 Air-water test run 108, J_L = 1.611 m/s, J_G = 0.14 m/s (at injection position)

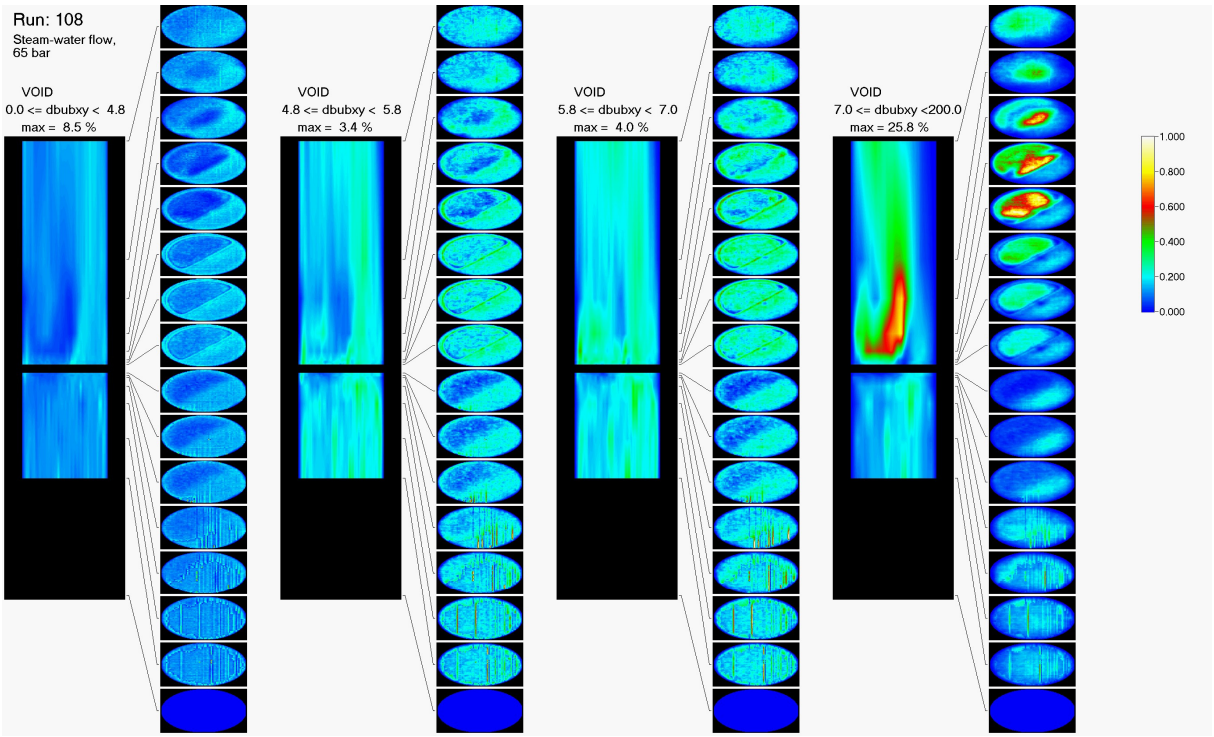

Fig. C.24 Steam-water test run 108, J_L = 1.611 m/s, J_G = 0.14 m/s (at injection position)

Attachment C: Void fraction distributions decomposed in bubble-size classes

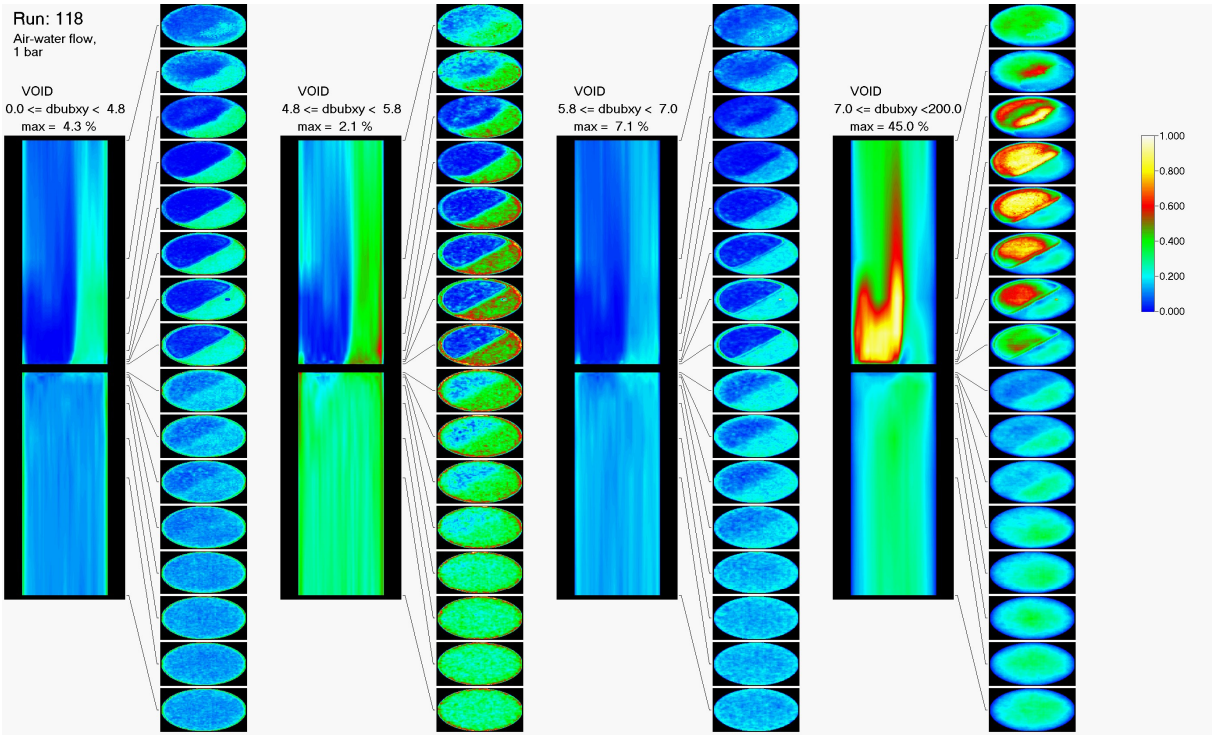

Fig. C.25 Air-water test run 118, J_L = 1.017 m/s, J_G = 0.219 m/s (at injection position)

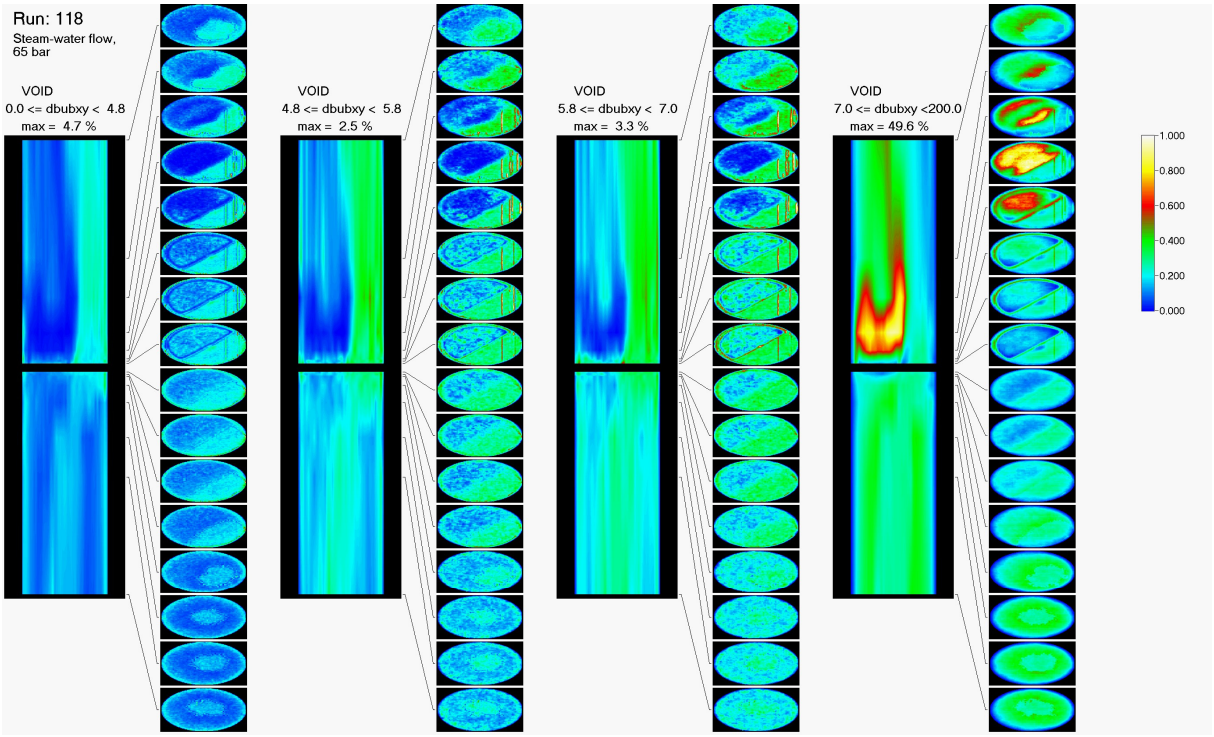

Fig. C.26 Steam-water test run 118, J_L = 1.017 m/s, J_G = 0.219 m/s (at injection position)

Attachment C: Void fraction distributions decomposed in bubble-size classes

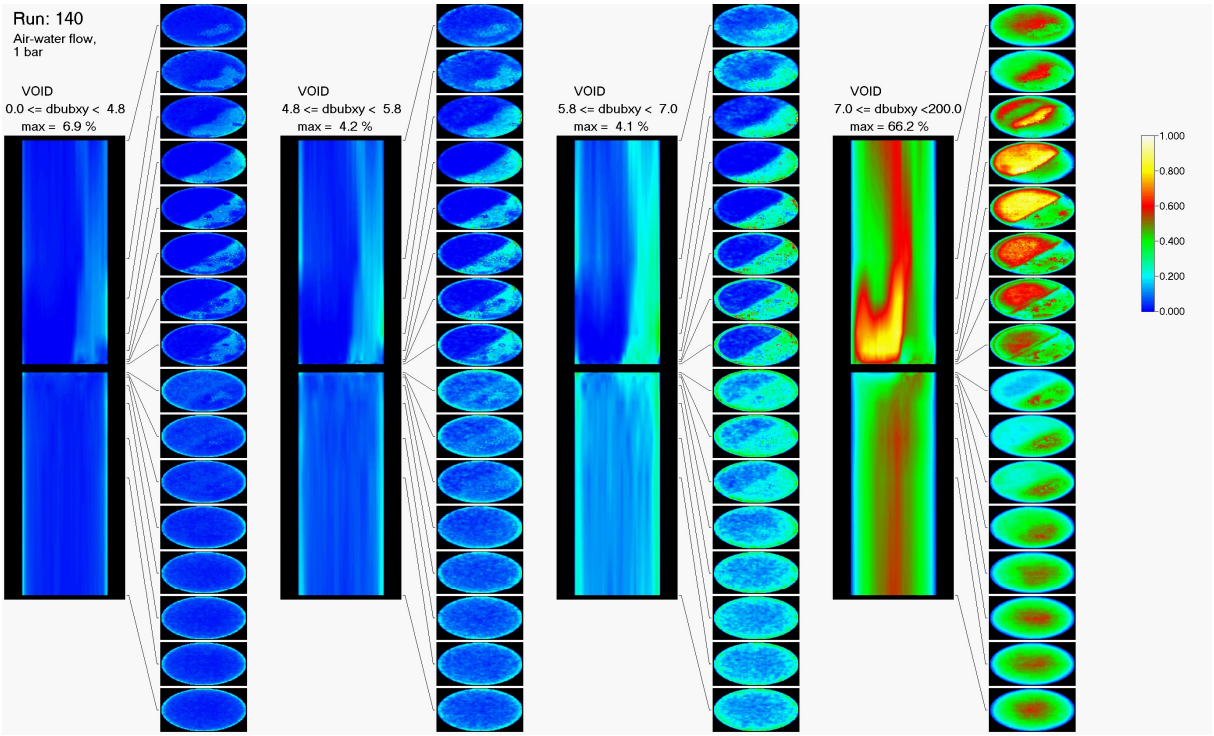

Fig. C.27 Air-water test run 140, J_L = 1.017 m/s, J_G = 0.534 m/s (at injection position)

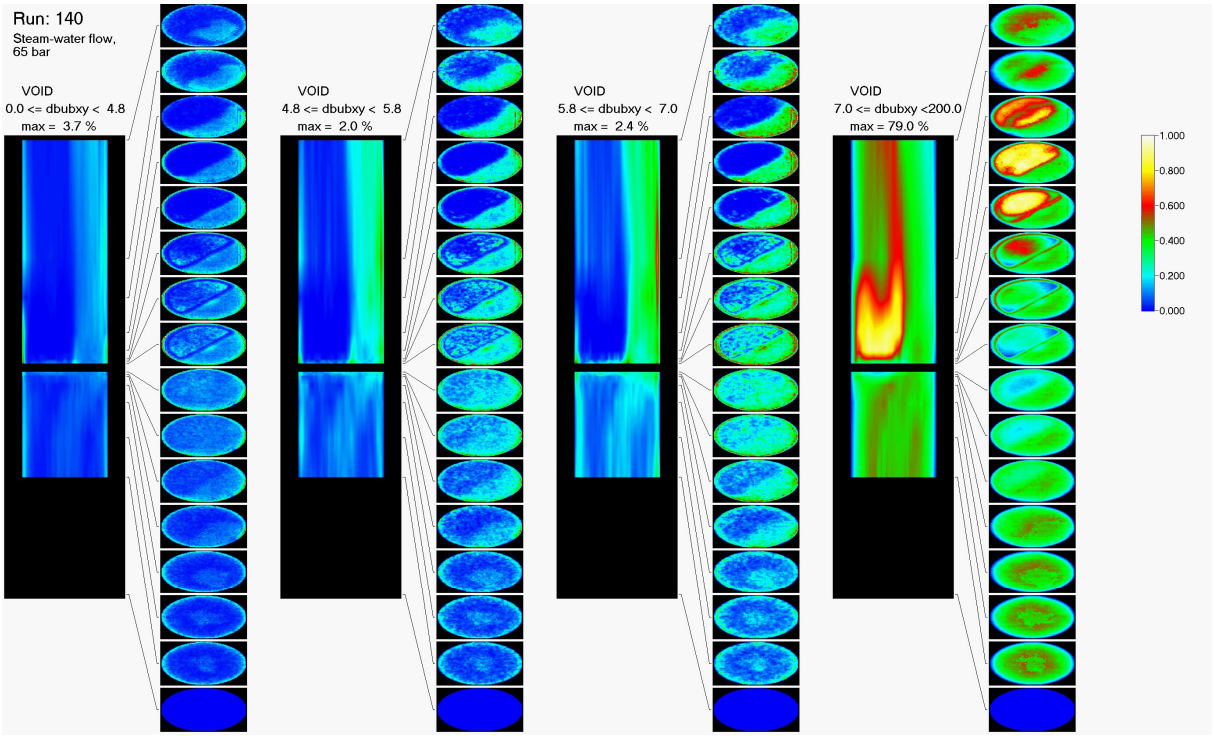

Fig. C.28 Steam-water test run 140, J_L = 1.017 m/s, J_G = 0.534 m/s (at injection position)

Attachment C: Void fraction distributions decomposed in bubble-size classes

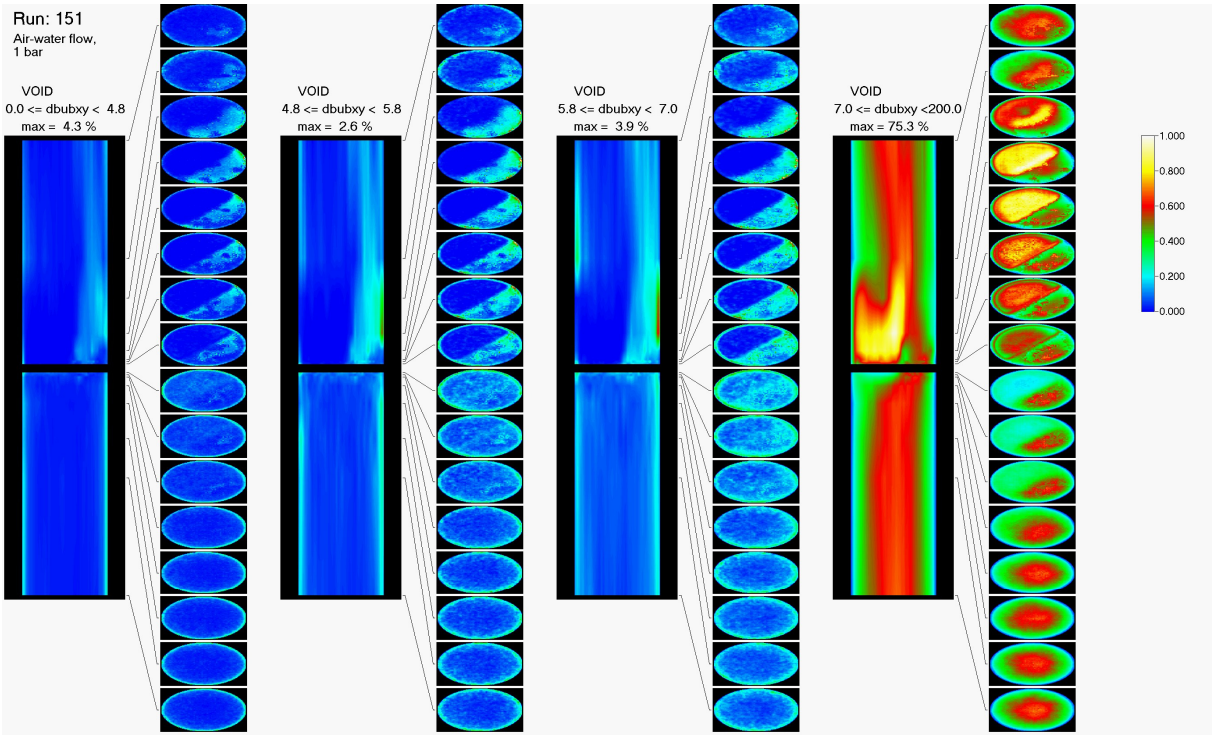

Fig. C.29 Air-water test run 151, J_L = 1.017 m/s, J_G = 0.835 m/s (at injection position)

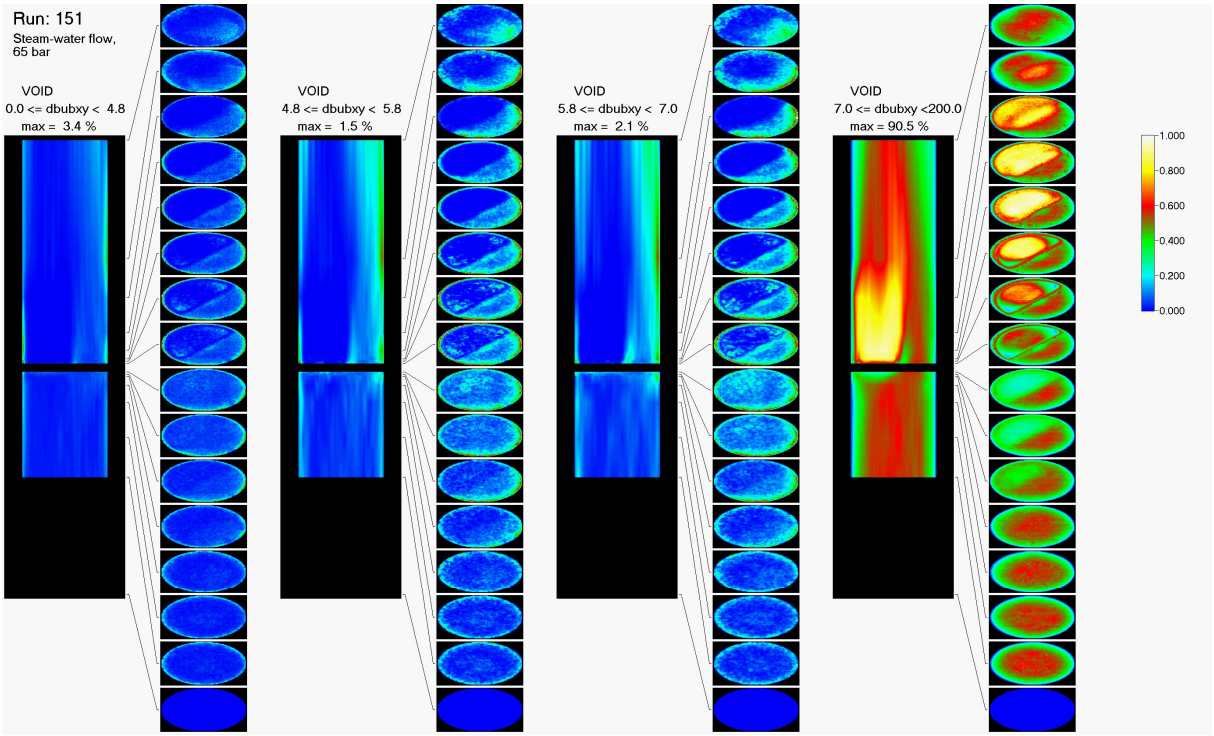

Fig. C.30 Steam-water test run 151, J_L = 1.017 m/s, J_G = 0.835 m/s (at injection position)